Doctoral Dissertation

Investigating the role of mechanochemistry and ionic microenvironment in hydrogel-induced myoblast differentiation and calcium-driven glioblastoma stemness

(ハイドロゲル誘導性筋芽細胞分化とカルシウム駆動性神経膠芽腫幹細胞性におけるメカノケミストリーとイオン性微小環境の役割に関する研究)

Yuheng Nie

Division of Soft Matter

Graduate School of Life Science

Hokkaido University

June 2025

Chapter 1

Cationic hydrogels promote malignant phenotypes *via* Calcium-NFAT-c-Myc driven glioblastoma reprogramming

Table of Contents

1. Abstract

Glioblastoma has a poor prognosis and a markedly low five-year survival rate. Glioma stem cells (GSCs) are regarded as a critical factor in recurrence, but the molecular mechanisms of GSCs generation in tumor microenvironment remain unclear. It has been reported that glioblastoma tissue is rich in positive charges due to the influence of the extracellular matrix and hypoxia. In this study, we developed adjustable, fully synthetic hydrogels to elucidate the effect of different charges on stemness induction. By varying the concentration of polymer-associated ionizable monomers, we synthesized hydrogels with surface charges ranging from negative to positive, and found that cationic hydrogels induced stem cell characteristics to the greatest extent. RNA sequencing revealed that cationic hydrogels enhance the expression of genes related to epithelial-to-mesenchymal transition, improve cell tolerance to temozolomide, and increase the expression of calcium channel proteins. Mechanistically, chromatin immunoprecipitation assays demonstrated that the cationic hydrogel activates the calcium ion-NFAT pathway, allowing NFATc1 and NFATc2 to translocate into the nucleus and act as transcription factors, thereby inducing c-Myc expression to promote glioblastoma stemness. The knockdown of NFATc1 and c-Myc significantly reduced cationic hydrogel-induced stemness, indicating that NFAT and c-Myc are crucial for this process. Spatial transcriptome analysis demonstrated that *c-Myc* is expressed surrounding palisading necrosis areas in addition to perivascular regions in human glioblastoma tissues. These results suggest that positively charged tumor microenvironment promote malignant phenotypes through calcium-NFAT-c-Myc-driven glioma reprogramming, providing a new strategy for glioma treatment.

Abbreviations

ABC: ATP-binding cassette

ALDH: aldehyde dehydrogenase

APTMA: (3-acrylamidopropyl) trimethyl-ammonium Chloride

APS: Ammonium persulfate

BBB: blood-brain barrier

CSCs: cancer stem cells

ChIP: chromatin immunoprecipitation

DMA: N,N-dimethylacrylamide

DMEM: Dulbecco's Modified Eagle Medium

EMT: epithelial-mesenchymal transition

ECM: extracellular matrix

ECs: endothelial cells

EFs: Electric fields

GBM: glioblastoma multiforme

GSEA: Gene Set Enrichment Analysis

GSCs: glioblastoma stem cells

ITGAV: integrin αv

ITGA6: integrin α6

MET: microelectrode technique

MDR: multidrug resistance protein

NaAMPS: 2-Acrylamido-2-methylpropanesulfonic acid

NFAT: nuclear factor of activated T cells

PS: polystyrene

qRT-PCR: Quantitative real-time polymerase chain reaction

RGD: Arginine-Glycine-Aspartic acid

siRNA: small interfering RNA

TMZ: temozolomide

TRP: Transient Receptor Potential

TME: tumor microenvironment

TEMED: Tetramethylethylenediamine

VEGFR: vascular endothelial growth factor receptor

2. Introduction

Glioblastoma multiforme (GBM), classified as a grade IV astrocytoma, is the most common, aggressive and lethal primary brain tumour in adults. Its incidence is increasing annually, ranging from 0.59 to 5 cases per 100,000 population; survival after disease onset is estimated to be 12 to 18 months, with 5% of diagnosed patients surviving more than 5 years[1,2]. The standard treatment for glioblastoma includes surgical resection, chemotherapy and radiotherapy[3]. However, despite the development of innovative diagnostic strategies and novel therapeutic approaches, the majority of patients eventually experience tumor recurrence and the poor prognosis of cancer has not been significantly improved. The search for better therapeutic strategies to combat this dreaded disease is a continuous endeavour.

Several studies have suggested that glioblastoma stem cells (GSCs), a rare cell population in tumor tissue, are involved in tumorigenesis and recurrence[4,5]. These cells have been reported to have robust self-renewal capacity, long-term survival, invasive phenotype, neurosphere forming capacity, and pluripotency[6]. In addition, GSCs have been shown to be more resistant to chemotherapy and radiotherapy, which explain the recurrence of tumours in many patients[5,6]. Therefore, targeting GSCs offers a the GSCs coexist with cellular and stromal components in specific niche microenvironments, which ultimately determine their fate. The perivascular niche plays a critical role in maintaining the GSC phenotype and GSCs self-renewal by interacting with endothelial cells (ECs) and activating Notch signalling pathways[7,8]. In addition, the hypoxic microenvironment activates hypoxia-inducible factor 2α (HIF-2α), thereby enhancing the self-renewal capacity of GSCs[9]. Several studies have reported a complex association between the perivascular and hypoxic microenvironments. Hypoxia affects angiogenesis and enhances the activity of vascular endothelial growth factor (VEGF)[8,10], which is particularly important for maintaining tumour growth. Furthermore, GSCs are also present at the invasive front of GBM tumours and influence tumor cell infiltration into normal brain tissue[11]. Therefore, to develop novel therapeutic approaches targeting GSCs, it is crucial to understand the characteristics and behaviours of GSCs in diverse microenvironment *in vivo*, however; currently there is no reliable *in vitro* culture system to mimic the behaviours of GSCs in *in vivo* brain. The conventional two-dimensional (2D) cultures performed in tissue culture polystyrene (PS) dish frequently lack the ability to assess the influence of biophysical factors present in the tumor

microenvironment, such as composition and stiffness, on the maintenance of GSCs. In order to gain a detailed understanding of the properties of GSCs in brain tissue, it is necessary to develop a culture system that can stably generate GSCs by providing a highly reproducible and tunable tissue microenvironment. These models facilitate the identification of factors that play pivotal roles in therapy resistance and recurrence, ultimately leading to the development of novel therapeutic options.

Biomedical hydrogels are hydrophilic polymer-based biomaterials that are revolutionizing the development of medical materials[12]. These distinctive materials are especially effective at interfaces with complex cellular systems[13], providing novel *in vitro* and *in vivo* avenues to regulate cell fate and influence cell function. The development of advanced hydrogels that mimic the properties of biological tissues has the potential to revolutionize biomedical engineering applications[14], especially in emerging fields such as stem cell therapy[15] and cancer research[16]. At present, biological or synthetic hydrogels have become standard products designed to actively regulate various aspects of stem cell signalling pathways, thereby enhancing morphogenesis, proliferation and differentiation[17,18]. A significant number of these systems employ bio- or biomimetic patterns within the hydrogel backbone to modify responses based on established interactions between cells and native extracellular matrix (ECM) molecules. These interactions are frequently combined with mechanical and biophysical properties similar to stem cell niches, promote differentiation pathways such as myogenesis, chondrogenesis, and neurogenesis[19,20]. We have recently reported that fully synthesised double-network (DN) hydrogels can be employed to rapidly reprogram differentiated cancer cells into cancer stem cells (CSCs), thereby identifying biomarkers for cancer-targeted therapy[21].

One of the factors that defines cell-matrix interactions is the transmission of mechanical signals, such as stress, elasticity, and shear forces, from the matrix to the cell, designated as mechanotransduction. Furthermore, cellular responses to changes in morphology, proliferation, and differentiation are crucial aspects of these interactions[22]. Mounting evidence indicates that matrix elasticity plays a regulatory role in the proliferation and differentiation of endothelial stem cells and certain types of tissue stem cells. Adult neural stem cells cultured on relatively rigid synthetic substrate differentiate predominantly into glial cells, whereas neurons are the predominant cell type observed on softer substrates resembling brain tissue[23]. Similarly, in the field of oncology, it has

been demonstrated that stiffer matrices markedly enhance the stemness of liver cancer stem cells compared to softer matrices, significantly enhancing the malignant potential at the hepatocellular carcinoma cells and tissue levels[24,25].

On the other hand, cancer cell proliferation disrupts the local ionic environment, membrane potential, and transepithelial potential, leading to small electrical alterations in the tumor microenvironment. Electric fields (EFs) have been demonstrated to profoundly affect several important phenotypes of cancer cells, including migration[26] (galvanotaxis), proliferation[27], and differentiation[28]. However, despite this growing evidence, the precise role of Efs as a regulator of cancer progression and metastasis, and the underlying mechanisms by which EF exerts its effects remain poorly understood. In this study, we employed a distinctive synthetic hydrogel system to examine the effect of electric charge on the stemness, drug resistance, and migration ability of glioblastoma cells, by modifying the charge ratio of the basal surface through varying the monomer ratio as an external artificial electric field. Our findings demonstrate that the cationic charged hydrogels induce intracellular calcium influx and activate the NFAT transcriptional factor to induce oncogene c-Myc, leading to the upregulation of the stemness, drug resistance, and migration of glioblastoma cells.

3. Experimental section

3.1 Hydrogel preparation

The charged hydrogels were prepared *via* one-step radical polymerization in glass model. The two glass surfaces were separated by silicon spacers of defined thickness (typically 1–3 mm). The hydrogels with controlled surfaces charge were synthesized by the previously-developed technique. These hydrogels were dialyzed in deionized water for at least two weeks prior the cell seeding. The anionic monomer 2-acrylamido-2-methylpropanesulfonic acid sodium salt (NaAMPS, 49.7wt% aqueous solution) was provided by Toagosei Co., Ltd., (Japan) and used as received. All of the materials, including (3-acrylamidopropyl) trimethyl-ammonium Chloride (APTMA), N,N-Dimethylacrylamide (DMA), crosslinker N,N′-methylenebis(acrylamide) (MBAA), Tetramethylethylenediamine (TEMED) obtained from Wako Pure Chemical Industries, Ltd., Japan and used as received. All other reagents and solvents were purchased from Sigma-Aldrich.

3.2 Determination of ζ potential

Dulbecco's Modified Eagle Medium (DMEM, Wako) was selected as the reference solution. The carbon electrode was placed in the DMEM as a reference electrode. A glass microelectrode was inserted into the hydrogel at a constant speed of 8 μm/sec, controlled by a micromanipulator (DMA-1511, Narishige). The output signal is recorded in real time using an oscilloscope (Iwatsu, DS-4264) and the potential signal is recorded at a rate of 100 samples per second. All measurements were taken at 25°C.

3.3 Cell lines and cell culture

The human GBM cell lines U138 (ATCC#HTB-16) was purchased from American Type Culture Collection. U373 and KMG4 cell lines were kindly provided by Dr. Kazuo Tabuchi (Saga University, Saga, Japan). All cell lines were cultured in DMEM) supplemented with 10% FBS. All cells were maintained in a humidified cell incubator with 5% CO_2 at 37°C.

3.4 Antibodies

Antibodies against the following proteins were used for western blotting: Nanog (1:2000, Cell Signaling Technology; 4903), Sox2 (1:1000, Cell Signaling Technology; 14962), Oct4 (1:1000, Cell Signaling Technology; 2890), CD133 (1:1000, Cell Signaling Technology; 64326), N-Cadherin (1:1000, Cell Signaling Technology; 13116), E-Cadherin (1:1000, Cell Signaling Technology; 3195), Histone3 (1:1000, Cell Signaling Technology; 4620), Vimentin (1:1000, Cell Signaling Technology; 5741), c-Myc (1:1000, Cell Signaling Technology; 5605), NFATc2 (1:1000, Cell Signaling Technology; 5861), NFATc1 (1:1000, Cell Signaling Technology; 8032) and β-actin (1:5000, Sigma; A5316). The following antibodies were used for chromatin immunoprecipitation (ChIP): NFATc1 (1:100, BioLegend; 649601) and normal rabbit IgG (Cell Signaling Technology; 2729). The following antibodies were used for immunohistochemistry (IHC): c-Myc (1:200, Abcam; ab32072).

3.5 Western blotting

The western blotting procedure was carried out as per the manufacturer's protocol. Initially, total protein from cultured cells were extracted using cold RIPA buffer with protease inhibitors on ice. The supernatants were collected, and the total protein concentrations were measured using a Bradford protein concentration assay kit (Bio-rad). Subsequently, an equal amount of total protein was separated by 10% SDS-PAGE and transferred onto Polyvinylidene Fluoride (PVDF) membranes (Cat#88518; Thermo Fisher Scientific). The membranes were then blocked at room temperature with 5% skim milk or 2% BSA for 1 hour and incubated with specific primary antibodies, Subsequently, the membranes were incubated with HRP-conjugated secondary antibodies, Goat Anti-Mouse IgG (H + L)-HRP (Cat#7076), and Goat Anti-Rabbit (H + L)-HRP (Cat#7074, all from Cell Signaling Technology) at room temperature for 2 hours, and the bands were visualized using Western Blotting Detection Reagents (Amersham; Cat#RPN2106). GAPDH was used as an internal control, and the images were captured with a Amersham Imager 600 System (Amersham, Cat#66930529).

3.6 Quantitative real time PCR (qRT-PCR) and ChIP-qPCR

Total RNA was isolated from KMG4, U373 and U138 Glioblastoma using a RNeasy Mini Kit (Qiagen, Valencia, CA) according to the manufacturer’s protocols and reverse transcribed into cDNA using the SuperScript® VILO™ cDNA Synthesis Kit (Invitrogen, Carlsbad, CA). Relative expression levels of mRNA

were normalized to glyceraldehyde-3-phosphate dehydrogenase (GAPDH). ChIP analysis was performed dusing a SimpleChIP® Plus Enzymatic Chromatin IP Kit(Cell Signaling Technolog; 9005) , qRT-PCR samples were prepared with the same amount of cDNA, Power SYBR green PCR master mix, and the following primers:

GAPDH	forward: 5′-AGCCAC ATCGCTCAGACAC-3′	reverse: 5′-GCCCAATACGACCAAATCC-3′
SOX2	orward: 5′-GCTACAGCATGATGCAGGACCA-3′	reverse: 5′-TCTGCGAGCTGGTCATGGAGTT-3′
Nanog	forward: 5′-CTCCAACATCCTGAACCTCAGC-3′	reverse: 5′-CGTCACACCATTGCTATTCTTCG-3′
Oct4	forward: 5′-CCTGAAGCAGAAGAGGATCACC-3′	reverse: 5′-AAAGCGGCAGATGGTCGTTTGG-3′
CD44	forward: 5′-CCAGAAGGAACAGTGGTTTGGC-3′	reverse: 5′-ACTGTCCTCTGGGCTTGGTGTT-3′
ALDH1A1	forward: 5′-CGGGAAAAGCAATCTGAAGAGGG-3′	reverse: 5′-GATGCGGCTATACAACACTGGC-3′
CD133	forward: 5′-CACTACCAAGGACAAGGCGTTC-3′	reverse: 5′-CAACGCCTCTTTGGTCTCCTTG-3′
ABCG2	forward: 5′-GTTCTCAGCAGCTCTTCGGCTT-3′	reverse: 5′-TCCTCCAGACACACCACGGATA-3′
ABCB5	forward: 5′-TTTGCCTATGCGGCAGGGTTTC-3′	reverse: 5′-CAAAACGAGCGTTTCTCCGATGG-3′
TRPC1	forward: 5′-CCAAACTGCTGGTGGCAATGCT-3′	reverse: 5′-GGAATGATGTTGAAAGGTGGAGG-3′
TRPC2	forward: 5′-TTCCATTGGCAAGATGATTGAAGAC-3′	reverse: 5′-CTGCAAACTCGGGCACCAGAAA-3′
TRPC3	forward: 5′-TTGGCTACTGGATCGCACCTTG-3′	reverse: 5′-GAGGCATTGAACACAAGCAGACC-3′
TRPC6	forward: 5′-GCAGACAATGGCGGTCAAGTTC-3′	reverse: 5′-AATGGTGAAGGAGGCTGCGTGT-3′
TRPV1	forward: 5′-GTGGACAGCTACAGTGAGATGC-3′	reverse: 5′-GGAAGCCACATACTCCTTGAGG-3′
TRPV3	forward: 5′-ATCCTACTGCGGAGTGGCAACT-3′	reverse: 5′-CGCTTCTCCTTGATCTCACGAC-3′
TRPM4	forward: 5′-TGTATCTGCTCTCGGACAAGGC-3′	reverse: 5′-GCTGAGGAAACTGCATTGGAACC-3′
TRPM5	forward: 5′-GCGTACTCAAGGACTTCCTGCA-3′	reverse: 5′-TTCAGGTCCAGCAGCCACTTCT-3′
NFATc1	forward: 5′-CACCAAAGTCCTGGAGATCCCA-3′	reverse: 5′-TTCTTCCTCCCGATGTCCGTCT-3′
c-Myc	forward: 5′-CCTGGTGCTCCATGAGGAGAC-3′	reverse: 5′-CAGACTCTGACCTTTTGCCAGG-3′
c-Myc-ChIP	forward: 5′-ACTTTCGCAAACCTGAACGC-3′	reverse: 5′-GCAACCAATCGCTATGCTGG-3′

qRT-PCR was performed using StepOnePlus™ Real-Time PCR System (Applied Biosystems, Waltham, MA) using Power SYBR® Green Master Mix (Invitrogen).

3.7 RNA sequencing and gene set enrichment analysis (GSEA)

RNA-seq libraries were prepared using the NEBNext® Ultra RNA Library Prep Kit for Illumina (New England Biolabs, MA, USA) and validated using the 2100 Bioanalyzer (Agilent Technologies). Libraries were sequenced on a NovaSeq 6000 sequencer (Illumina, CA, USA). Clean reads were aligned to the human genome (hg37) using HISAT2 (version 2.0.5) after removing low-quality reads. The differential expression of C2N8 and PS control in U373 cells was computed using the fragments per kilobase of transcript per million mapped reads calculated by featureCounts (version 1.5.0-p1). Pathway analyses of differentially expressed genes were performed using GSEA as previously described[70]. The enrichment of differentially expressed genes in C2N8 and control PS group of U373 cells were analyzed using the Webgestalt Platform, a free online tool available at www.webgestalt.org.

3.8 Wound healing assay

KMG4, U373 and U138 cell lines were seeded in 6-well plates (with or without C2N8 hydrogel) and allowed to grow until reaching full confluence. Subsequently, a scratch was introduced to the cell monolayer using a 200-µL pipette tip. The detached cells were then removed by washing twice with PBS, and the remaining cells were cultured in DMEM supplemented with 10% FBS. Images were acquired using a light microscope at 0, and 24-h time points, with a magnification of ×4.

3.9 Drug resistance assay

KMG, U373 and U138 cells cultured on PS dish and C2N8 hydrogels were treated with or without different concentrations of Temozolomide (TMZ) (1, 10, 100, and 1000 µM), and further incubated for 72 hours. After 72 hours, the cell pellet was resuspended with 5ml PBS. The 0.4% trypan blue dye solution was added into 5 µl cell suspension at a ratio of 1:1 and injected into cell counting chamber slide (Invitrogen). Counting was performed with Countess II FL (Invitrogen), and the independent experiments were repeated for three times. The percentage of cell viability was calculated as follows: active cell rate (%) = (number of unstained cells/total cell number) × 100.

3.10 Immunofluorescence staining

The GBM cells cultured for 7 days in the DMEM were washed with pre-warmed PBS and fixed with 3% paraformaldehyde (PFA) solution for 15 min, treated with 0.1% v/v Triton X-100 for 4 min to make the cell membrane permeable, and incubated in the blocking solution (1% BSA in PBS) for 20 min. For each step, the samples were washed with PBS once. The samples were incubated with a mouse monoclonal antibody (anti-NFATc2 (Cell Signaling Technology; 5861) at a 1:400 dilution in PBT (containing 0.1% BSA and 0.05% Triton X-100 in PBS) at 4°C overnight, and then incubated with Alexa 594-conjugated anti-Rabbit IgG (Invitrogen) in PBT for 1 hour. The nuclei were stained with DAPI (1 μg/ml) for 20 min in PBT. The washing steps using PBT were included between each staining step. The fluorescence images were obtained with the Olympus IX83 inverted microscope. The obtained images were analyzed using the ImageJ software (National Institutes of Health, Bethesda, MD).

3.11 Knock-down of NFATc1 and c-Myc by siRNA transfection

siRNAs for NFATc1 and c-Myc were purchased from Dharmacon (https://horizondiscovery.com/en/dharmacon). According to the manufacturer's protocols, siNFATc1 and sic-Myc were transfected into the cells at a final concentration of 10 μM and 20 μM, respectively. The transfection efficiency was verified by qRT-PCR. Cell mRNA were collected at 48 h after transfection.

3.12 Immunohistochemistry and H&E staining using glioblastoma tissue

Immunohistochemistry (IHC) for c-Myc was performed using glioblastoma FFPE tissue with antigen retrieval by incubating at pH 9.0, 97ºC, for 20 min. The sections were incubated with 1% bovine serum albumin (BSA) for 10 min at room temperature for preventing non-specific binding of antibodies. After washing, the sections were incubated with anti-c-Myc antibody (ab32072, abcam) at 100× dilution. The subsequent processes were carried out according to the manufacturer's instructions using the Envision FLEX visualization system (Dako; Agilent Technologies, Inc., Santa Clara, CA). H&E staining was performed according to the general staining procedure.

3.13 Spatial transcriptome analysis by Xenium in glioblastoma tissue

The original H&E images are first normalized to [0, 1] per channel. The alignment between H&E images and ST spot i produces the histology image patches $\in \mathbb{R}^{P\times P\times C}$ (with P as the side length of the patch and C as the number of image channels, for example, C = 3 for RGB images and C = 1 for grayscale images). We set P = 26 by default to approximate the number of pixels surrounding each spot. The image patch yi is then flattened in the Starfysh model and assumed to be generated from the same latent variable zi that informs gene expression (Fig. 1c and Supplementary Fig. 1a) with a distribution p(yi|zi) parameterized by two neural networks gμ, gσ, for mean and variance of distribution for yi, respectively. Both consist of a linear layer followed by a batch normalization layer. They define:

$$p\left(\, y_i \,|\, z_i\right) = \mathrm{Normal}\left(\, g_\mu(z_i), g_\sigma(z_i)\right).$$

3.14 Statistical analysis

Statistical analyses of the mechanical testing, cell proliferation and gene expression were performed using one-way analysis of variance (ANOVA). P values less than 0.05 were considered statistically significant, and differences between samples within the groups were evaluated using a Student's t-test ($p < 0.05$).

4. Results

4.1 Synthesis and characterization of electrically charged hydrogels.

A synthetic hydrogel system was developed with a specific emphasis on modulating the concentration of charge while maintaining minor adjustments to the mechanical properties (stiffness) of the hydrogel. All polymers were synthesized via radical copolymerization and in situ cross-linking. The hydrophilic comonomer, N,N'-methylene-bis-acrylamide, was incorporated into the polymer network. The cationic monomer, (3-acrylamidopropyl) trimethylammonium chloride (APTMA), and the anionic monomer, 2-acrylamido-2-methylpropanesulfonic acid sodium salt (NaAMPS), were copolymerized with the neutral monomer, N,N-dimethylacrylamide (DMA). Ammonium persulfate (APS) and tetramethylethylenediamine (TEMED) were included as an initiator and a cross-linking agent, respectively. A series of five copolymers, designated A10 to C5N5 (where A represents anionic, N represents neutral, and C represents cationic), were fabricated by systematically varying the monomer ratios. Polystyrene (PS) tissue culture dishes were employed as a control substrate for comparative studies (**Fig. 1-3**). The surface charge properties of the hydrogels were characterized using the microelectrode technique (MET) to measure the zeta potential (ζ potential). The resulting ζ potential values ranged from -42.0 $\pm$ 2.7 mV (for A10) to +60.0 $\pm$ 7.9 mV (for C5N5), reflecting the controlled variation in cationic and anionic monomer concentrations. Microelectrode detection further confirmed that the surface potential distribution across the hydrogels was highly uniform, indicating a homogeneous copolymer composition (**Fig. 4**). Cell adhesion assays revealed distinct behaviors among different glioblastoma cell lines on the hydrogel substrates. The KMG4, U373, and U138 glioblastoma cell lines exhibited complete non-adherence to anionic (A5N5) and neutral (N10) hydrogels. In contrast, the A10 hydrogel displayed adherence to these cells. Interestingly, cationic hydrogels significantly promoted glioblastoma cell attachment (**Fig. 5**). Additionally, the effect of cationic charge concentration on cell viability was evaluated, with the C5N5 hydrogel showing reduced cell viability compared to other hydrogel types, suggesting a potential cytotoxicity associated with higher cationic charge densities (**Fig. 5**). Typically, cell adhesion to native extracellular matrices is mediated by specific biochemical interactions between the arginine-glycine-aspartic acid (RGD) peptide motif and integrin receptors on the plasma membrane. However, cationic surfaces, such as those created by poly-L-lysine or polyethyleneimine coatings,

facilitated cell adhesion predominantly through electrostatic interactions rather than specific molecular recognition[29]. This highlights the importance of charge-dependent physical interactions in mediating cell-material interfaces, particularly in synthetic hydrogel systems.

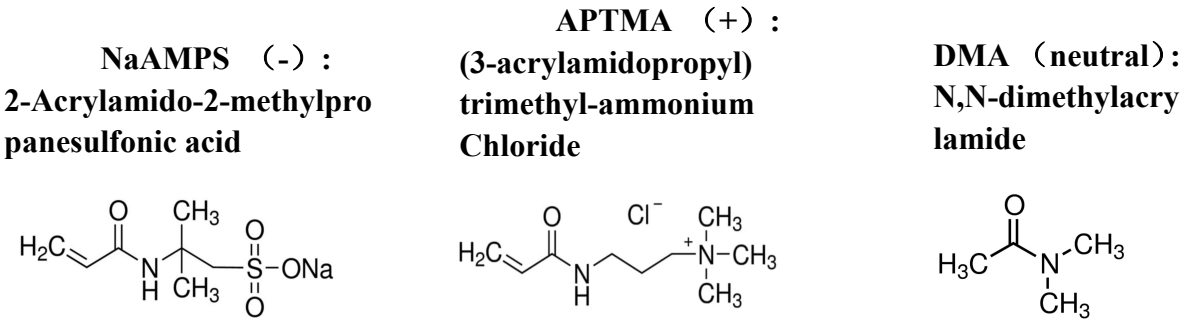

Figure 1. The synthesis of charged hydrogels involves three distinct types of monomers: NaAMPS (-), APTMA (+), and DMA (neutral).

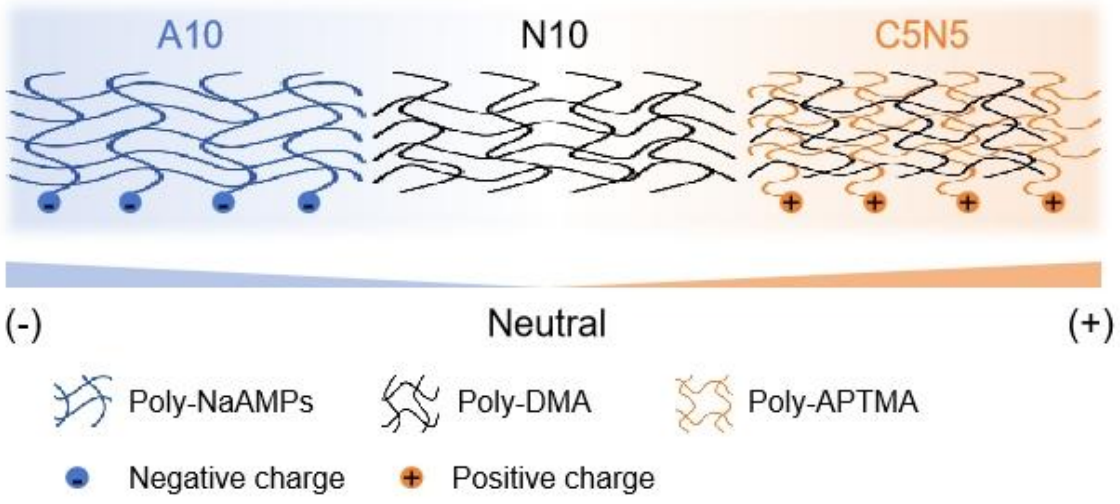

Figure 2. Crosslinker, Anti-coagulant, Initiator, and the monomer ratio of different charged hydrogels.

Crosslinker-MBAA: N,N'-Methylene-bis-acrylamide (4 mol%)

Monomer：1 mol/L

Anti-coagulant: 10% APS

Initiator: 0.1% TEMED

Name	APTMA (mol)	NaMPs (mol)	DMA (mol)	DDW (ml)	MBAA (ml)	APS (ml)	TEMED (µl)
A10-50 kPa	0	0.012	0	1.899	1.561	0.25	6
A5N5-50 kPa	0	0.0059	0.003	3.691	0.609	0.25	6
N10-50 kPa	0	0	0.006	4.454	0.676	0.25	6
C2N8-50 kPa	0.001	0	0.0048	4.523	0.427	0.25	6
C2N8-200 kPa	0.001	0	0.0048	2.831	2.119	0.25	6
C5N5-50 kPa	0.0027	0	0.003	3.824	0.876	0.25	6

Figure 3. Ratio of monomer, cross-linker agent and initiator of different charged hydrogels.

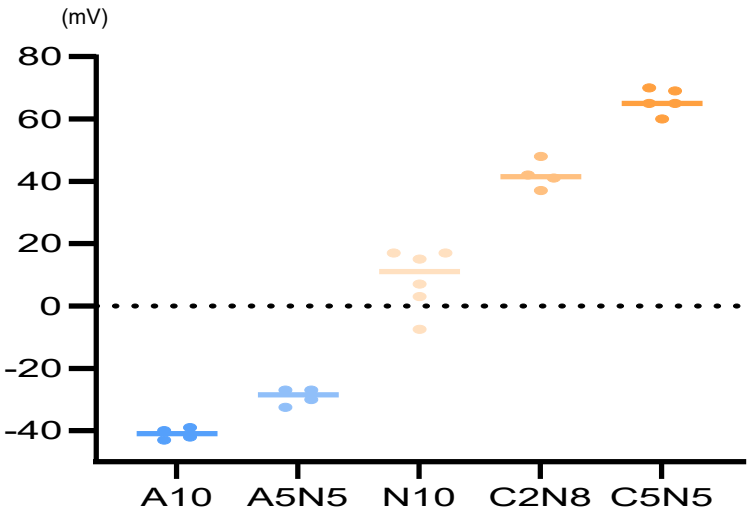

Figure 4. Specific ζ potential of different charged hydrogels.

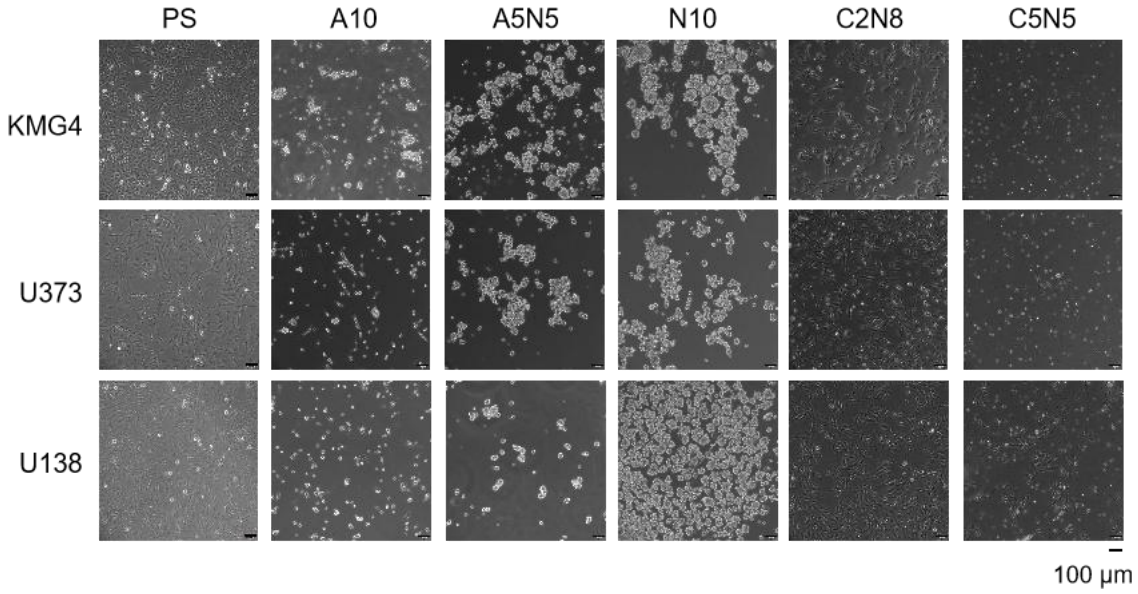

Figure 5. Cellular morphology of KMG4, U373 and U138 cell lines cultured on different charged hydrogels. Representative images are shown (magnification ×4). Scale bars, 100 μm.

4.2 Cationic hydrogels upregulate stemness markers in glioblastoma.

The maintenance and regulation of cancer stem cells (CSCs) are governed by a complex interplay of transcription factors, including Sox2, Nanog, and Oct4, which are pivotal regulators of self-renewal and pluripotency in CSCs. Among the various markers associated with CSCs, CD44, a non-kinase transmembrane glycoprotein, and CD133 (prominin-1), a five-transmembrane glycoprotein, are widely recognized as key identifiers of CSCs across multiple cancer types[31, 32]. Additionally, recent studies have highlighted the elevated activity of aldehyde dehydrogenase (ALDH) in CSCs, which serves as a functional marker for their identification and isolation[33]..In this study, we investigated the expression of these critical CSC-related factors in response to variations in the ζ potential of hydrogels. The KMG4, U373, and U138 glioblastoma cell lines exhibited differential expression of *Sox2*, *Nanog*, and *Oct4* when cultured on hydrogels with stiffness of 50 kPa and varying ζ potentials. Notably, the expression levels of these transcription factors were maximized on the C2N8 cationic hydrogel (**Fig. 6**). Furthermore, the expression of cancer stemness markers, including *CD44*, *CD133*, and *ALDH1A1*, was significantly upregulated on the C2N8 cationic hydrogel (**Fig. 7, 8**). Notably, comparative analysis revealed that the C2N8-50 kPa hydrogel exhibited stronger cancer stemness-inducing capacity than the 200 kPa counterpart (**Fig. 9)**.

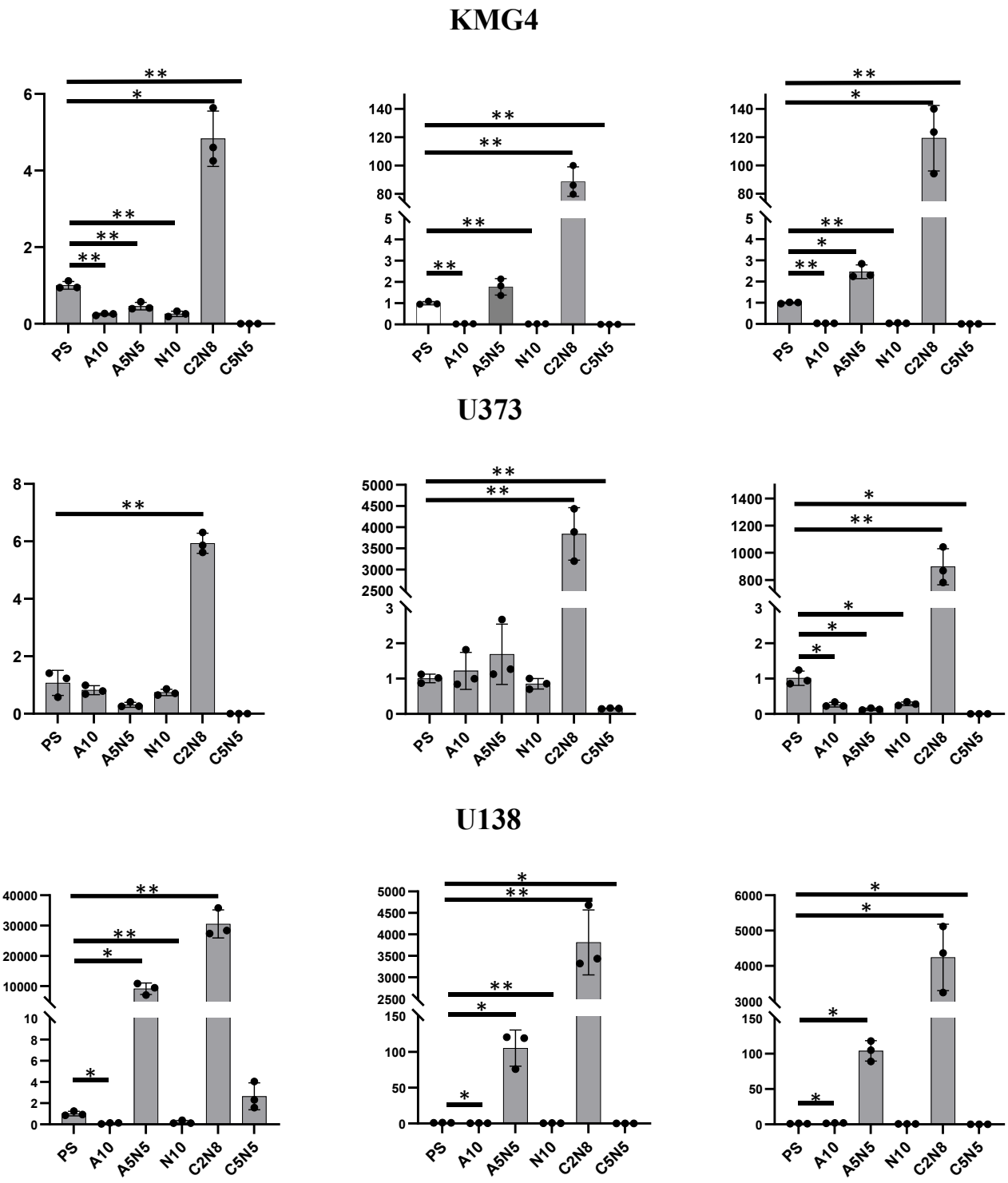

Figure 6. qPCR results showed that KMG4, U373 and U138 cells expressed Sox2, Nanog and Oct4 on A10, A5N5, N10, C2N8 and C5N5 hydrogels. Data were normalized to the GAPDH mRNA (mean ± SD, n = 3). two-tailed t tests; *P < 0.05; **P < 0.01.

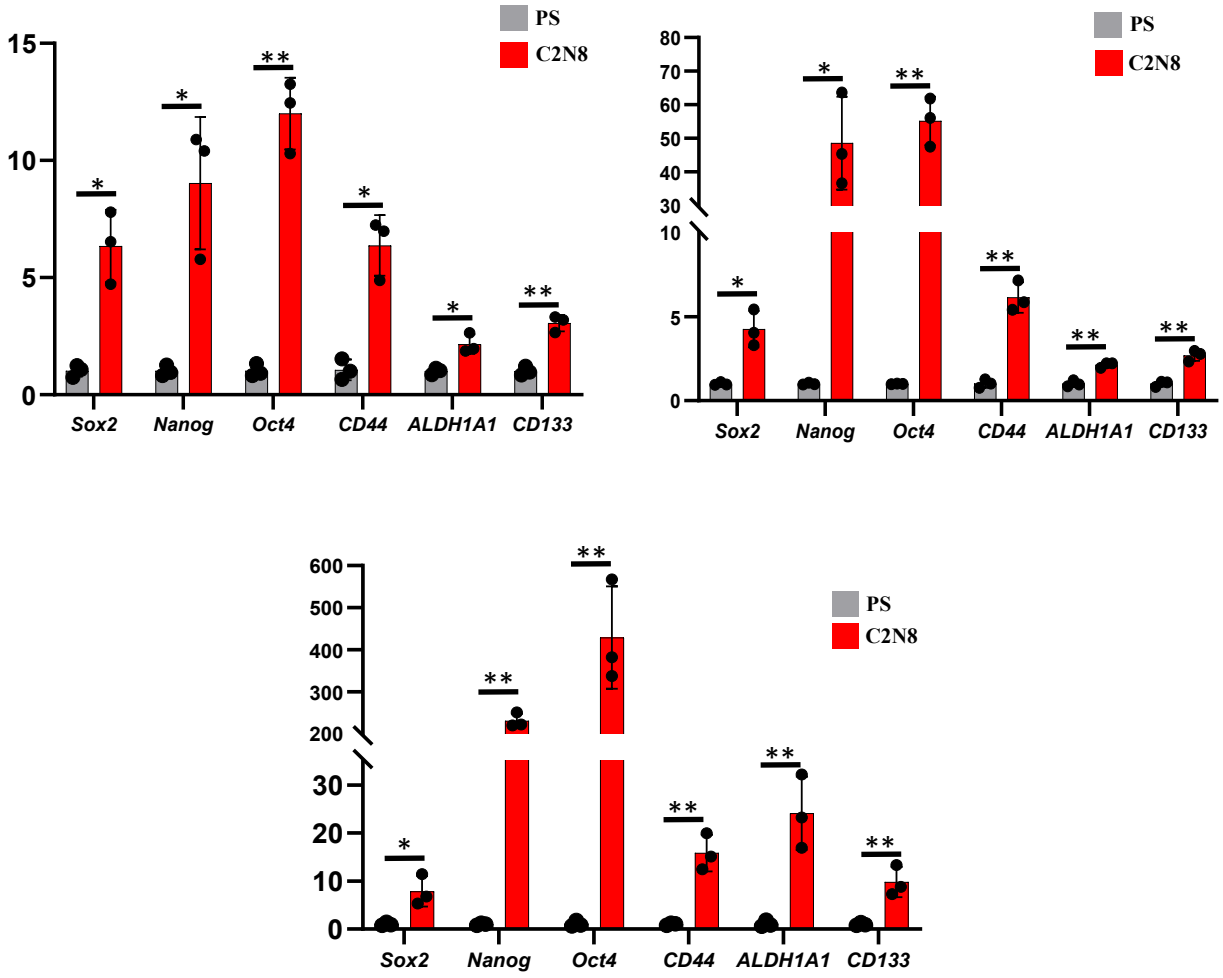

Figure 7. qPCR shows that C2N8 hydrogel increased Sox2, Nanog, Oct4, CD44, ALDH1A1 and CD133 levels in KMG4 cell, U373 and U138 cells. Data were normalized to the GAPDH mRNA (mean ± SD, n = 3). two-tailed t tests; *P < 0.05; **P < 0.01. (G) Western blotting shows that C2N8 hydrogel increased Sox2, Nanog, Oct4, and CD133 levels in KMG4 cell, U373 and U138 cells.

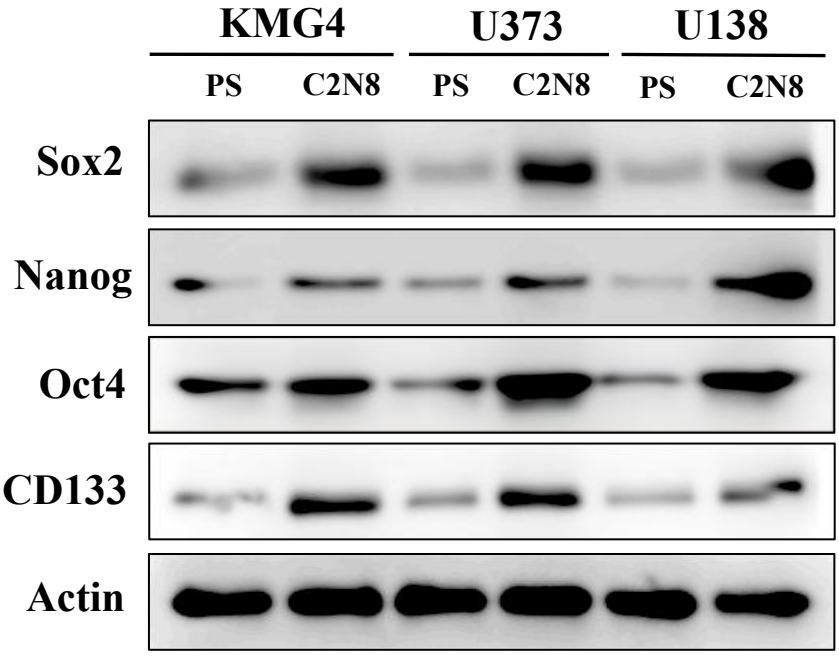

Figure 8. Western blotting shows that C2N8 hydrogel increased Sox2, Nanog, Oct4, and CD133 levels in KMG4 cell, U373 and U138 cells.

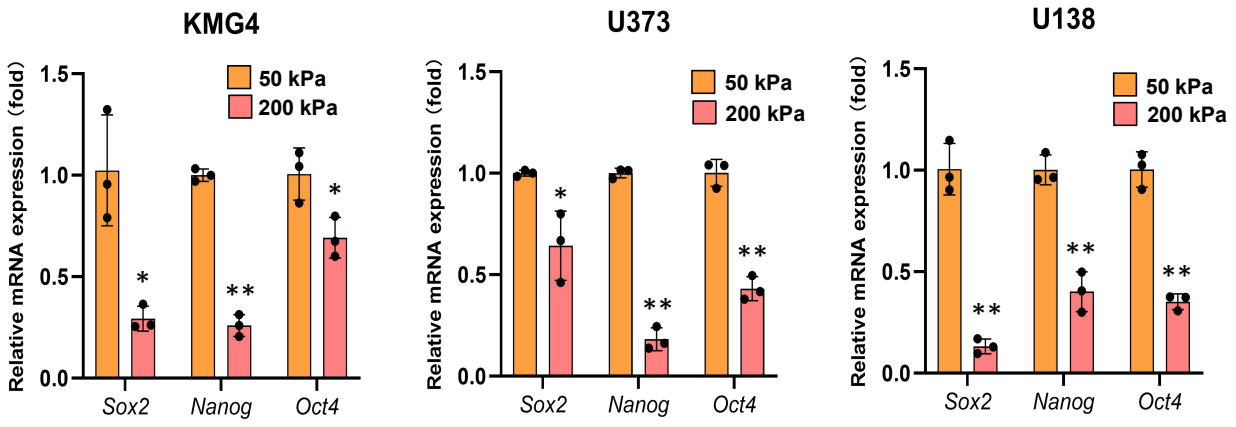

Figure 9. Western blotting shows that C2N8 hydrogel increased Sox2, Nanog, Oct4, and CD133 levels in KMG4 cell, U373 and U138 cells. Expression of stem cell markers cultured on different stiffness hydrogels. KMG4, U373, U138 glioblastoma cells were cultured on C2N8-50 kPa and C2N8-200 kPa hydrogels, and the mRNA expression levels of the indicated genes were examined by qRT-PCR. Data were normalized to the *GAPDH* mRNA (mean ± SD, n = 3). two-tailed t tests; **P* < 0.05; ***P* < 0.01.

4.3 Glial-mesenchymal transition (GMT) is induced in response to cationic C2N8 hydrogel.

The comprehensive transcriptomic profile of U373 glioblastoma cells cultured on distinct substrates was analyzed using high-throughput RNA sequencing (RNA-seq), providing insights into the transcriptional changes induced by the hydrogel environment (**Fig. 10A, B**). Differentially expressed genes (DEGs) were identified based on a stringent threshold of fold-change greater than 1.5, revealing a total of 2481 DEGs, including 1644 upregulated and 837 downregulated genes, in the C2N8 hydrogel sample compared to the control (**Fig. 11A**). This extensive transcriptional remodeling highlights the profound influence of the substrate properties on cellular gene expression. To uncover the biological significance of these transcriptional changes, a sophisticated pathway enrichment analysis was performed on the DEGs. GO enrichment analysis suggested that the genes associated with C2N8 hydrogel were enriched in extracellular matrix, calcium channel complex, and metal ion transmembrane transporter activity (**Fig. 12**). The Kyoto Encyclopedia of Genes and Genomes (KEGG) pathway enrichment analysis revealed that the pathways involved in the DEGs in the C2N8 hydrogel samples (**Fig. 13**). Hallmark analysis revealed associations with eight distinct biological pathways, with the epithelial-mesenchymal transition (EMT) pathway being one of the most prominently upregulated pathways (**Fig. 11B, 14**). The EMT is a critical developmental and pathological process that plays a central role in tumor progression and metastasis. By promoting cellular mobility, invasiveness, and resistance to apoptosis, EMT confers metastatic potential to cancer cells, making it a key target in cancer research.

Consistent with the transcriptomic findings, Western blotting confirmed the upregulation of N-cadherin and Vimentin in the C2N8 hydrogel group, alongside a significant downregulation of E-cadherin compared to the polystyrene (PS) control (**Fig. 15**). These changes are hallmark features of the EMT process, where the loss of E-cadherin and gain of N-cadherin and Vimentin are indicative of a transition from an epithelial to a mesenchymal phenotype[34]. Vimentin, a type III intermediate filament protein, is typically associated with mesenchymal cells and is known to be upregulated during cancer metastasis, further supporting the EMT-associated phenotypic transformation observed in these cells[35].

To assess the functional implications of these transcriptional and proteomic changes, a wound healing assay was conducted to evaluate cell motility. The results demonstrated significantly enhanced migratory capabilities in the C2N8 hydrogel group compared to the PS control (**Fig. 16,**

17). Specifically, at 24 hours post-wounding, the wound closure rates for KMG4, U373, and U138 cells cultured on C2N8 hydrogel were 75.29 ± 3.00%, 66.73 ± 5.59%, and 70.24 ± 4.76%, respectively — substantially higher than those observed on PS dishes (57.70 ± 2.59%, 34.80 ± 5.76%, and 43.74 ± 3.13%, respectively). These findings underscore the pro-migratory effects of the C2N8 hydrogel environment, which may contribute to its ability to promote cancer cell invasion and metastasis. Furthermore, LC-MS/MS analysis and qRT-PCR identified Filamin A (FLNA) as a significantly upregulated protein in U373 cells cultured on the C2N8 hydrogel with a modulus of 50 kPa (**Figs. 18A-C**). FLNA is a key regulator of cytoskeletal organization and mechanotransduction, playing a critical role in maintaining cell structure and signaling pathways. Its upregulation aligns with its known involvement in EMT processes, where it contributes to the reorganization of actin filaments and enhances cell motility and invasiveness. Together, these findings highlight the complex interplay between substrate properties, transcriptional regulation, and cellular behavior in modulating cancer cell aggressiveness.

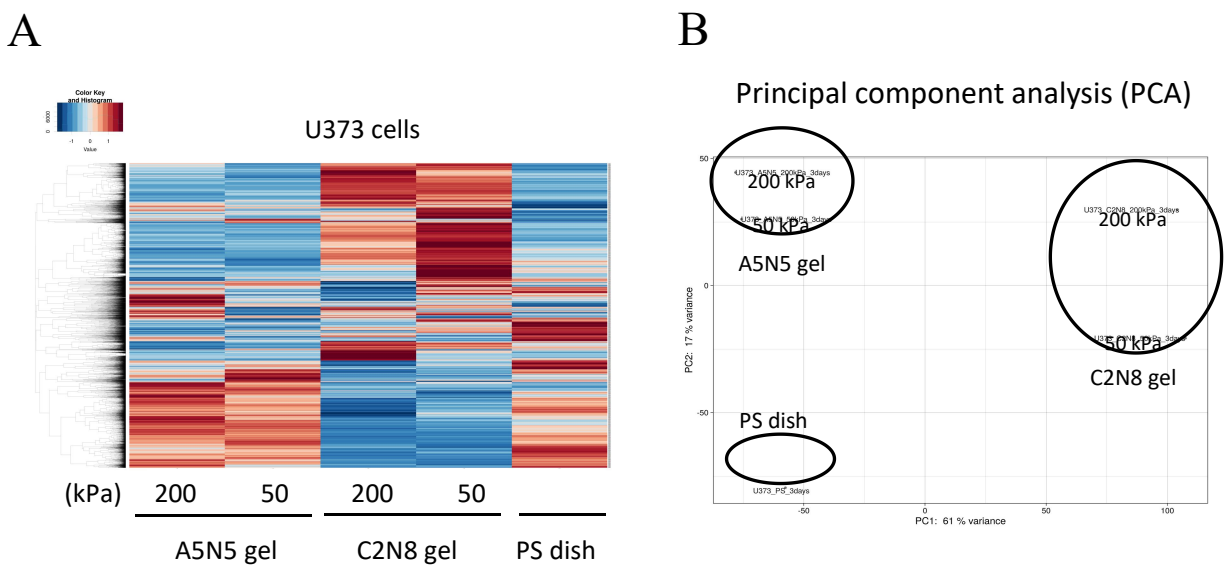

Figure 10. A Heatmap of RNA-seq expression profiles across five experimental groups: U373 cells were cultured on PS dish (control), A5N5 or C2N8 hydrogels (each with 50 kPa and 200 kPa) for 3 days. Rows and columns represent genes and samples, respectively, with hierarchical clustering illustrating expression patterns. Color intensity reflects normalized expression levels (Z-score). **B** Two-dimensional PCA projection of samples, marked by experimental groups. Principal component 1 (PC1) and PC2 explain 61% and 17% of the total variance, respectively.

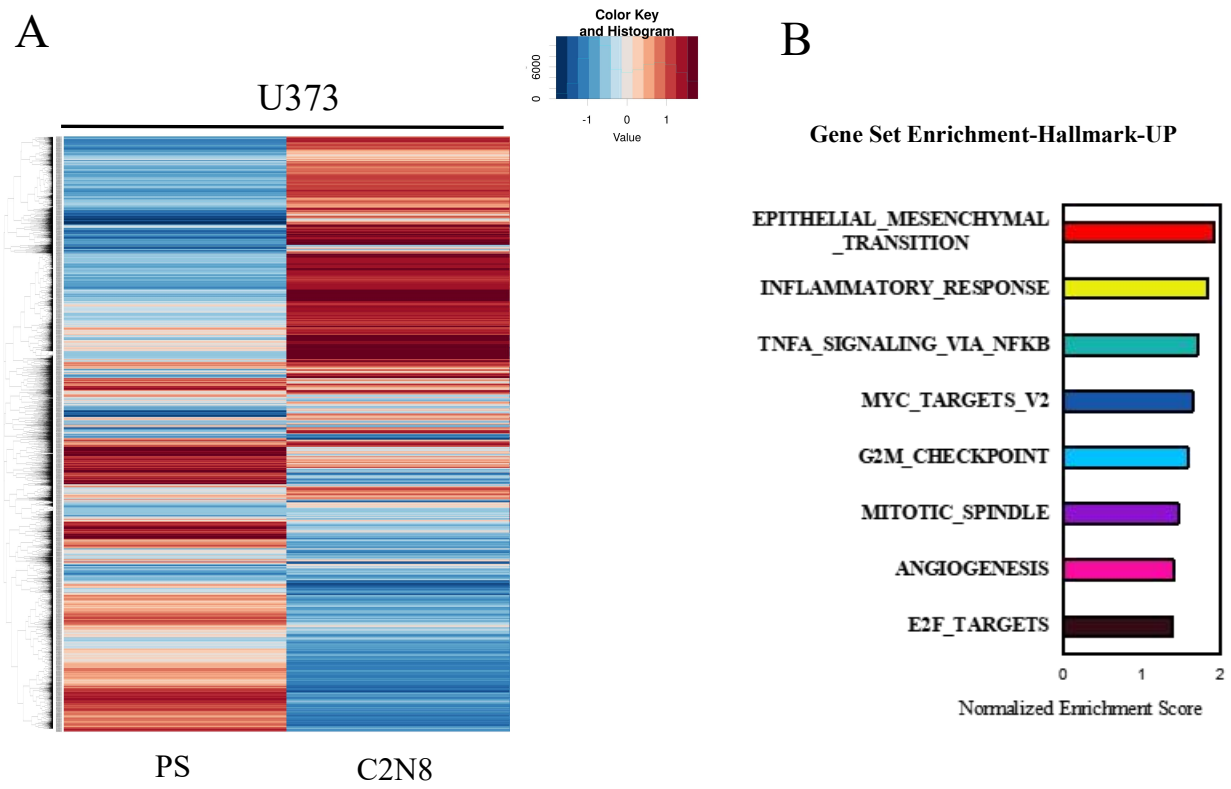

Figure 11. A Heatmap showing DEGs in U373 cell cultured on C2N8 hydrogel and PS dish. The color represents z-scores. U373 cells cultured in DMEM on C2N8 hydrogel or PS dish for 72 h, followed by processing for RNA-seq. **B** Analysis of C2N8 hydrogel group differential expression genes using the Hallmarker demonstrates a high correlation with the epithelial mesenchymal transition.

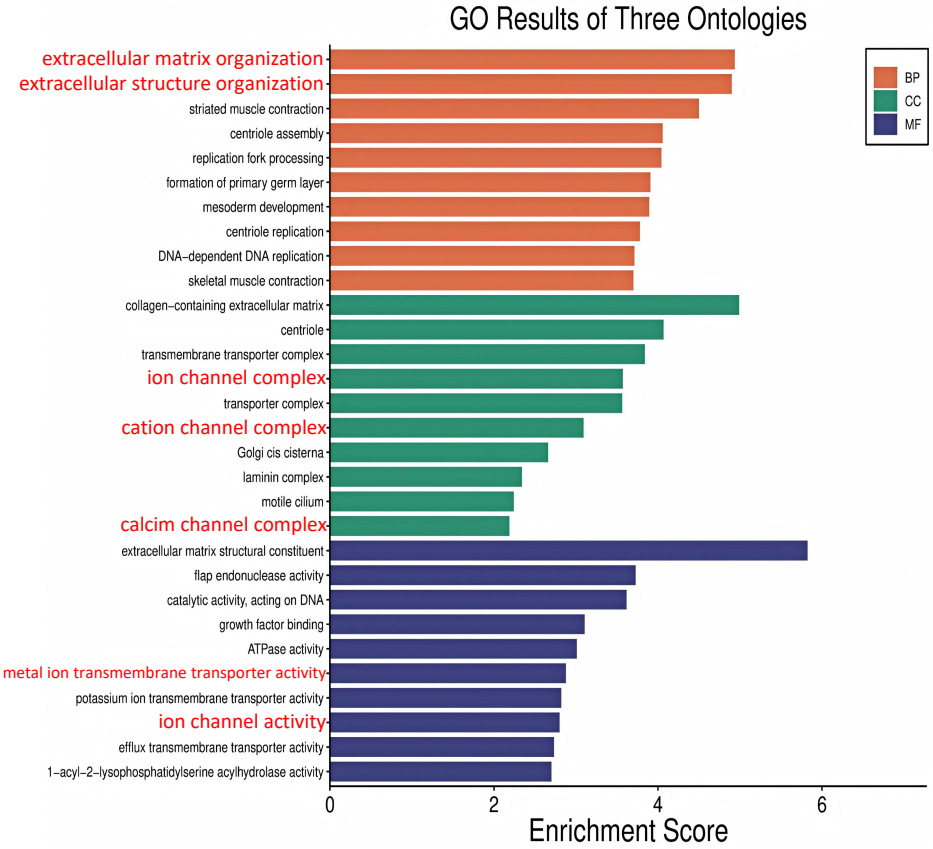

Figure 12. GO enrichment analysis of DEGs in C2N8 hydrogel group (Biological Progress, Cellular components and Molecular Function).

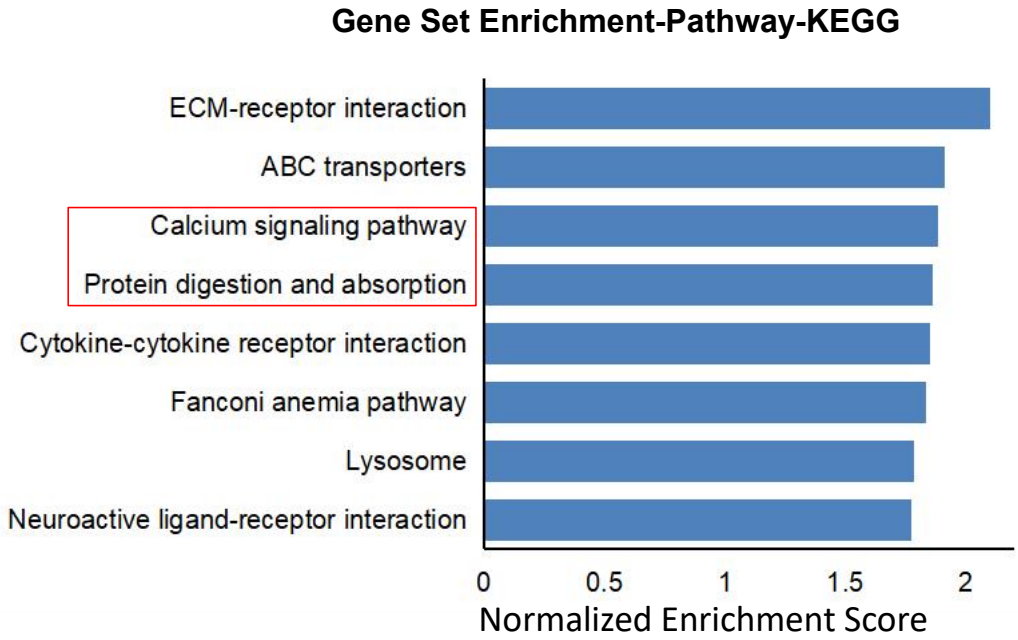

Figure 13. KEGG enrichment analysis of DEGs in C2N8 hydrogel group.

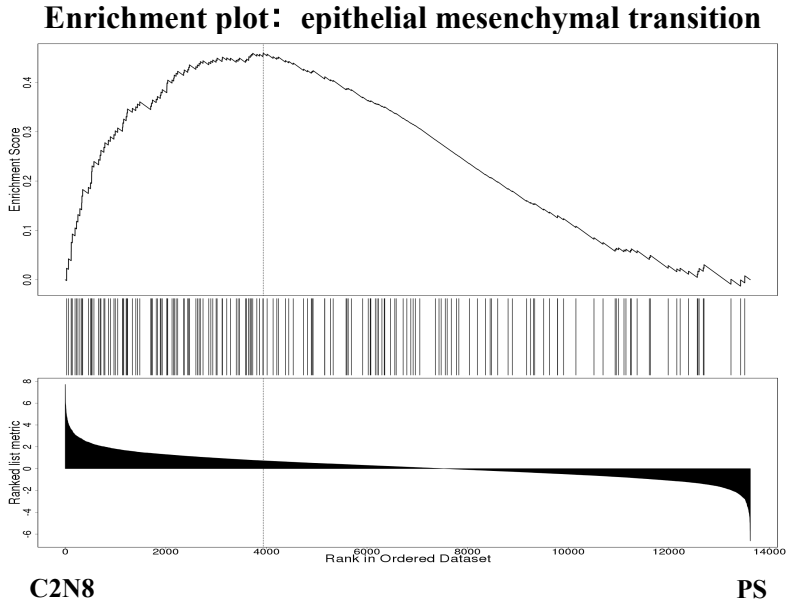

Figure 14. GSEA analysis of the differential expression C2N8 hydrogel gene set (epithelial mesenchymal transition) is displayed.

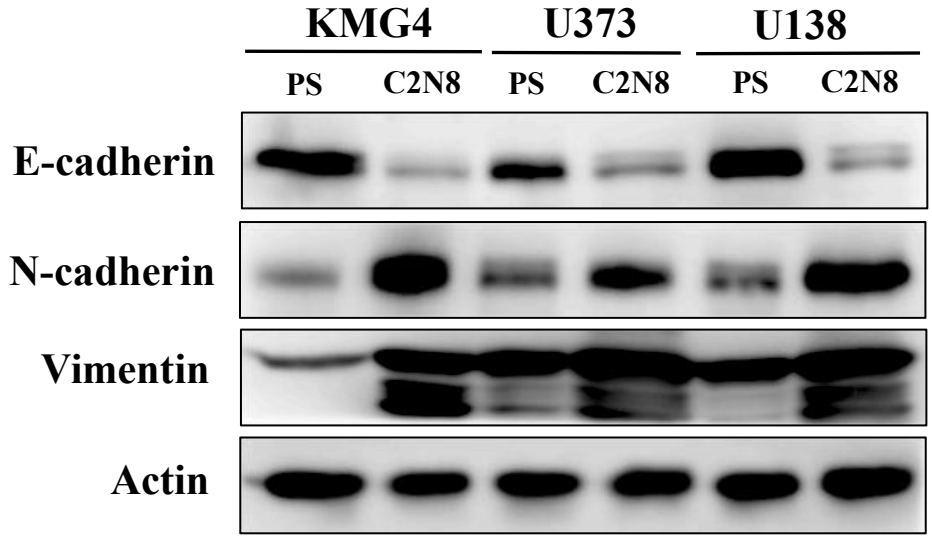

Figure 15. Western blotting showed that C2N8 hydrogel decreased E-cadherin levels, increased N-cadherin and Vimentin levels of KMG4, U373 and U138 cells.

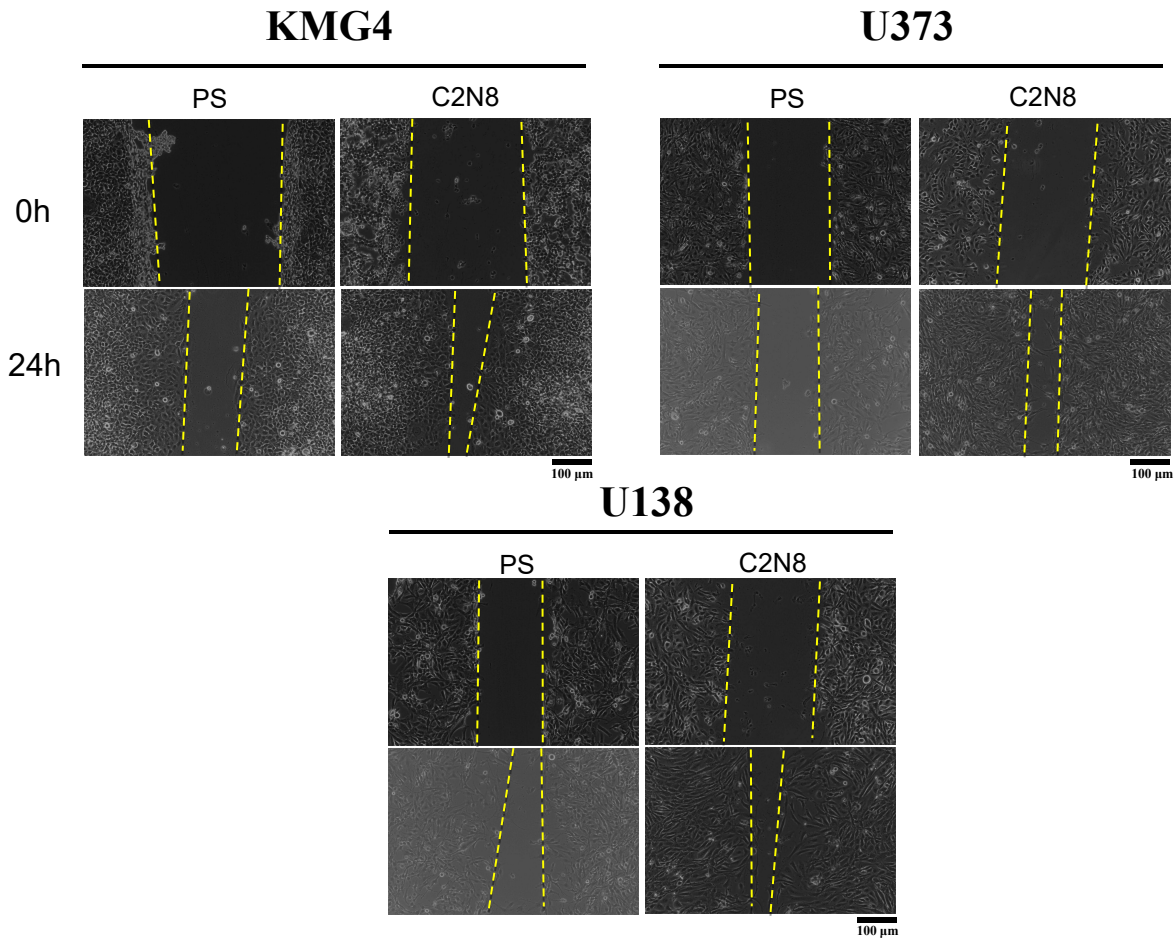

Figure 16. Wound healing assays were performed to assess the migratory capacity of KMG4, U373 and U138 cells on C2N8 hydrogel and PS dish. Representative images are shown (magnification ×4). Scale bars, 100 μm.

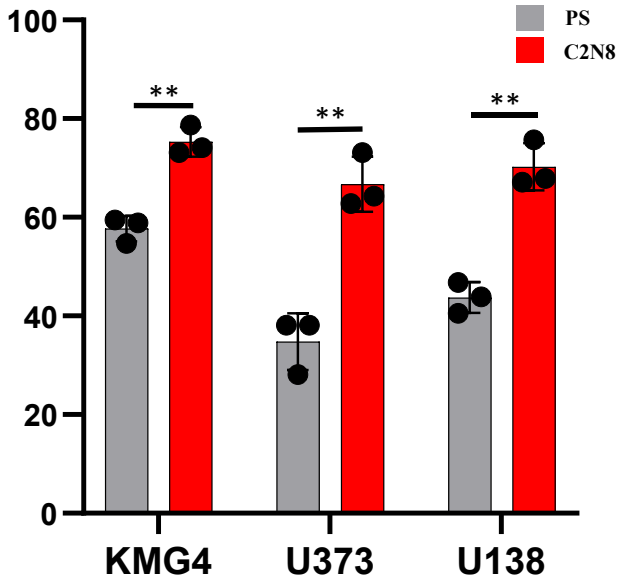

Figure 17. Wound healing assays were performed to assess the migratory capacity of KMG4, U373 and U138 cells on C2N8 hydrogel and PS dish. Data are shown as the mean ± s.e.m.; n = 3 independent experiments, two-tailed t tests; *P < 0.05, **P < 0.01.

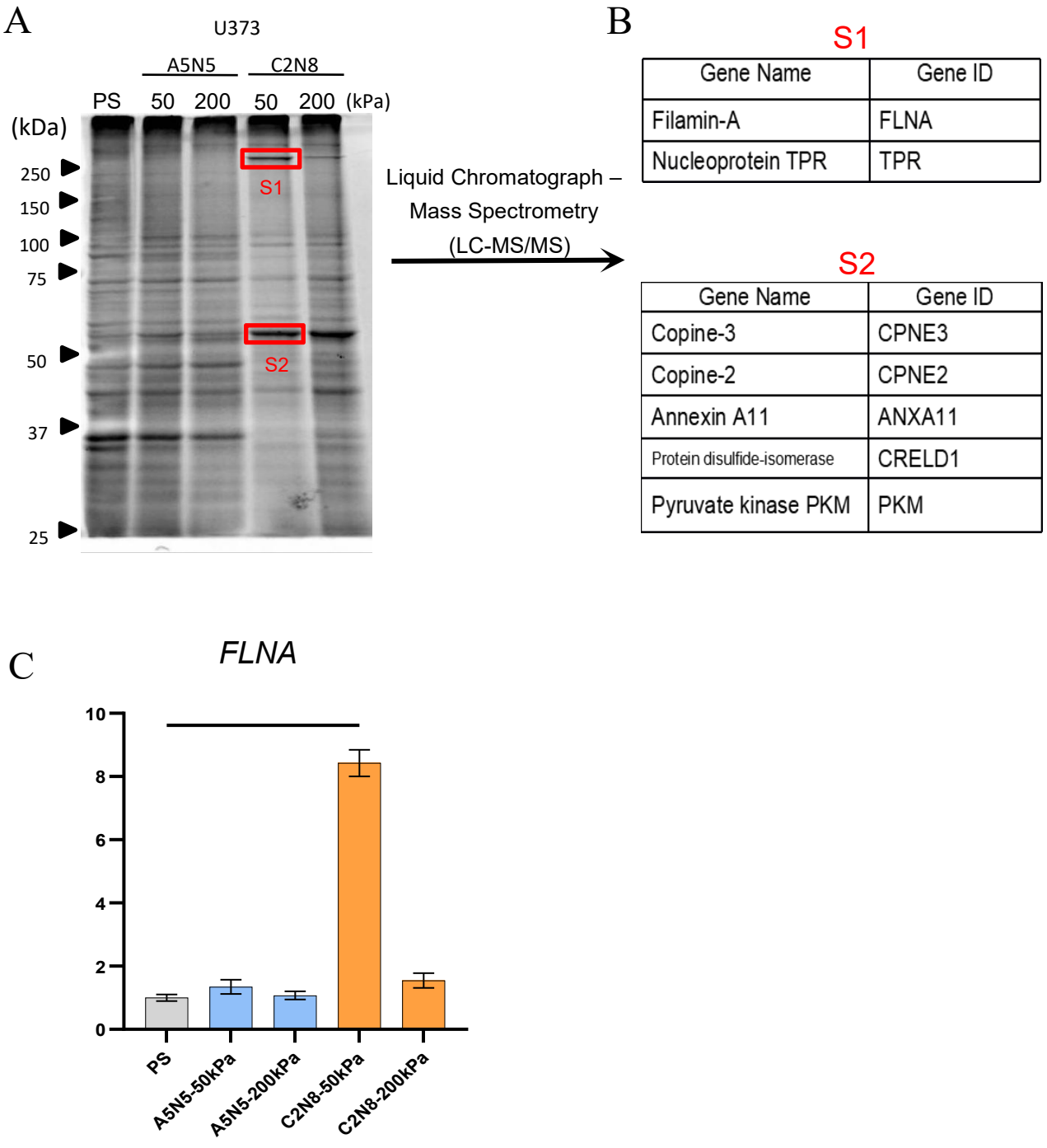

Figure 18. A Protein profiles of U373 cells cultured under indicated conditions were analyzed by SDS-PAGE and visualized by Coomassie Brilliant Blue staining. **B** Differentially enriched protein bands (S1 and S2) in C2N8-50 kPa hydrogel samples were excised and subjected to LC-MS/MS identification. **C** qRT-PCR analysis of mRNA expression in U373 cells cultured on PS dish or hydrogels (A5N5-50 kPa, A5N5-200 kPa, C2N8-50 kPa, C2N8-200 kPa). Data were normalized to GAPDH mRNA levels (mean ± SD, n = 3 biological replicates). Statistical significance was determined by two-tailed Student's t-tests (*P<0.05, **P<0.01).

4.4 C2N8 hydrogels induce molecular signatures showing low survival.

We performed a survival-associated gene enrichment analysis on the significantly upregulated genes in the C2N8 hydrogel samples, identifying a total of 32 survival-related genes (**Fig. 19**). Subsequent analysis of their expression patterns across various cancer types revealed that this specific gene set serves as a unique molecular signature for glioblastoma (GBM), with oligodendroglioma (LGG) also displaying a similar expression profile **(Fig. 20**). Importantly, further investigation into the relationship between this gene set and GBM patient survival demonstrated a statistically significant correlation: higher expression levels of these genes were strongly associated with poorer overall survival outcomes in GBM patients (**Fig. 21**).

These findings suggest that cells cultured on the C2N8 hydrogel exhibit molecular signatures indicative of aggressive tumor behavior and lower patient survival rates. This provides valuable insights into the underlying mechanisms of GBM pathogenesis and identifies potential therapeutic targets for improving clinical outcomes. Moreover, the identification of these survival-associated genes contributes to our understanding of the key molecular determinants influencing GBM prognosis, offering a robust foundation for future translational research in this field.

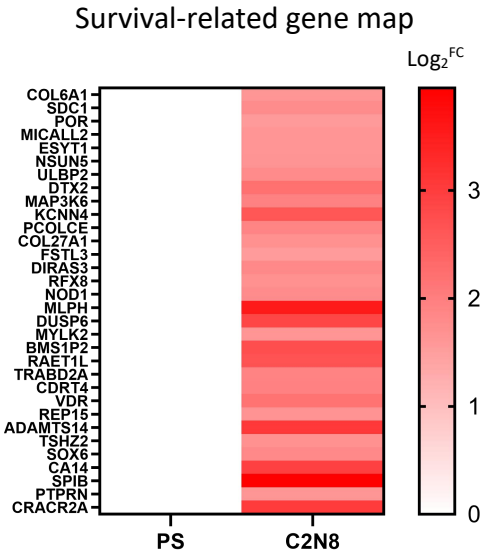

Figure 19. Differential expression of glioblastoma (GBM) survival-associated genes between C2N8 hydrogel and PS substrates.

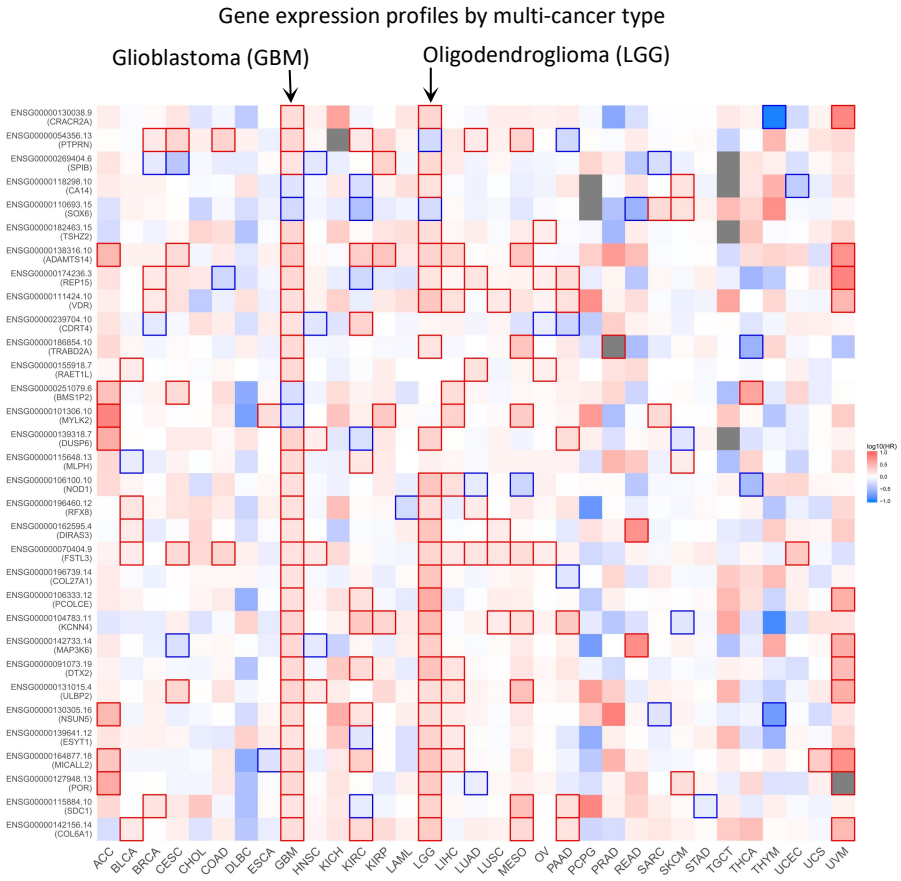

Figure 20. Expression patterns of 32 GBM survival-associated genes across 33 cancer types.

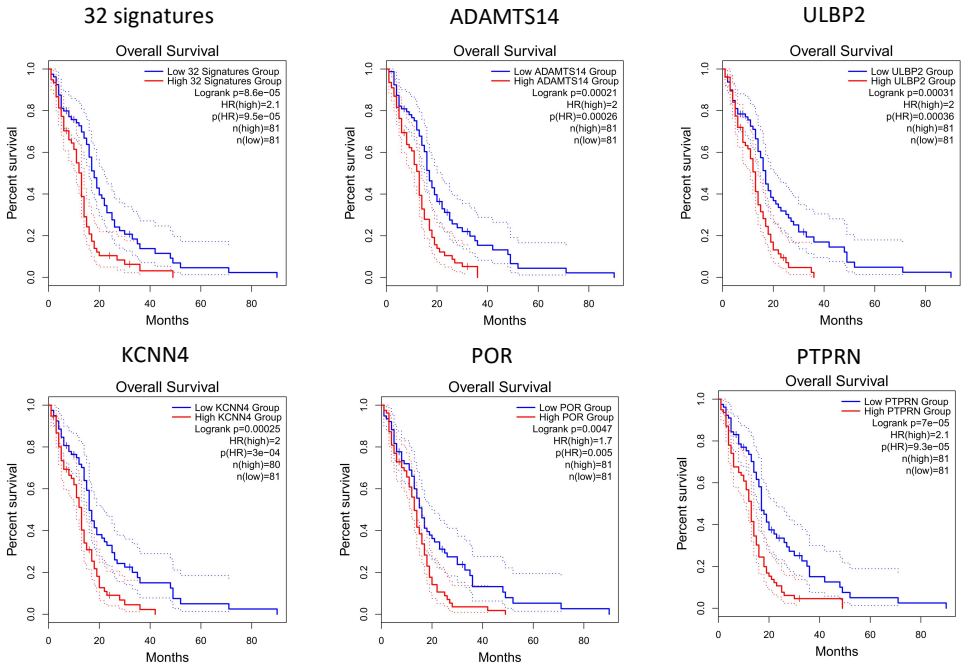

Figure 21. Prognostic analysis of the 32-gene panel in GBM survival; Kaplan-Meier curves for the combined gene set and five representative individual genes.

4.5 Drug resistance is increased on cationic C2N8 hydrogel.

The Kyoto Encyclopedia of Genes and Genomes (KEGG) pathway enrichment analysis revealed that the DEGs in the C2N8 hydrogel samples were predominantly involved in the ATP-binding cassette (ABC) transporter pathway (**Fig. 13, 22**). This finding highlights the critical role of ABC transporters in cellular functions, particularly in the context of drug resistance. Among these transporters, the multidrug resistance protein 1 (MDR1), also known as P-glycoprotein (P-gp), encoded by the ABC subfamily B member 1 (ABCB1) gene, has been extensively studied for its role in conferring resistance to cytotoxic drugs and targeted chemotherapy[36].

To investigate whether the C2N8 hydrogel influences the drug resistance of GBM to temozolomide (TMZ), a chemotherapeutic agent with alkylating properties, cell viability assays were conducted on GBM cells cultured on both polystyrene (PS) dishes and C2N8 hydrogels under TMZ exposure. TMZ, which is orally administered and capable of crossing the blood-brain barrier (BBB), was approved for GBM treatment in 2005 and is also used for various solid tumors, including advanced neuroendocrine tumors[37]. Three distinct GBM cell lines (KMG4, U373, and U138) were subjected to varying concentrations of TMZ for 72 hours (**Fig. 23**). The results demonstrated that low-dose TMZ had minimal impact on the viability of U373 and U138 cells. However, at higher TMZ concentrations, a significant reduction in cell mortality was observed in the C2N8 hydrogel group compared to the PS group (**Fig. 23**). This observation suggests that U373 and U138 cells exhibit inherent resistance to TMZ[38,39]. In contrast, KMG4 cells, which are more sensitive to TMZ, showed higher mortality in the PS group at low TMZ concentrations, while the C2N8 hydrogel group exhibited increased resistance (**Fig. 23**).

The multidrug resistance (MDR) protein ABCG2 is widely expressed across various cell types and plays a key role in the ATP-dependent efflux of endogenous and exogenous substances, thereby maintaining cellular homeostasis and protecting tissues from external insults. Another MDR-associated protein, ABCB5, has been implicated in chemotherapy-resistant cancer recurrence and is characterized by stem-like properties, including self-renewal, differentiation capacity, and therapeutic resistance[40,41]. qRT-PCR analysis revealed that all three GBM cell lines cultured on the C2N8 hydrogel exhibited increased expression levels of *ABCG2* and *ABCB5* compared to those cultured on PS dishes (**Fig. 24**). These findings suggest that the C2N8 hydrogel enhances the

expression of ABC transporters, modulating drug tolerance and highlights the importance of targeting ABC transporter pathways to overcome chemotherapy resistance in GBM.

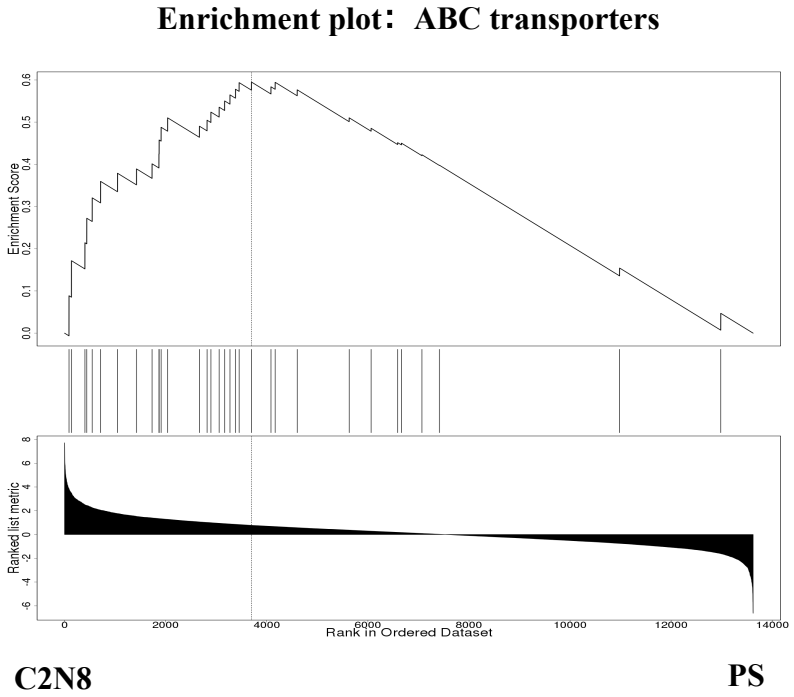

Figure 22. GSEA analysis of the differential expression C2N8 hydrogel gene set (ABC transporters) is displayed.

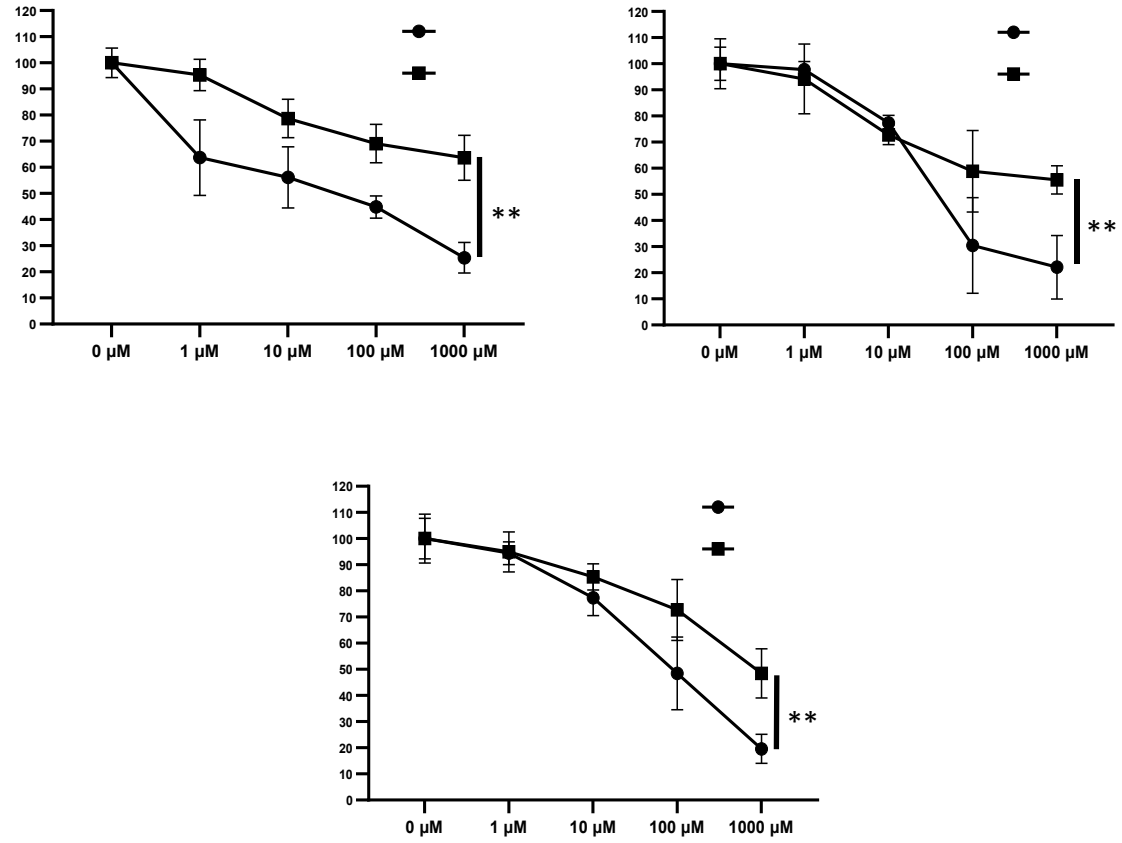

Figure 23. Compared with PS dishes, C2N8 hydrogel significantly improved the viability of KMG4, U373 and U138 cells under high concentration TMZ treatment (mean ± SD, n = 3), two-tailed t tests; *P < 0.05; **P < 0.01.

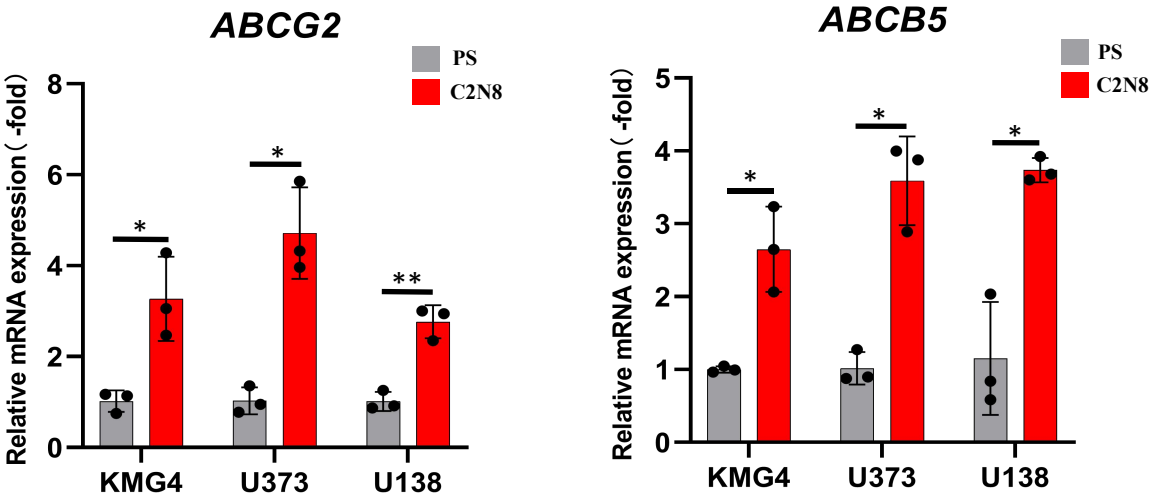

Figure 24. qPCR shows that C2N8 hydrogel increased ABCG2 and ABCB5 levels in KMG4 cell, U373 and U138 cells. Data were normalized to the GAPDH mRNA (mean ± SD, n = 3), two-tailed t tests; *P < 0.05; **P < 0.01.

4.6 C2N8 hydrogel promotes c-Myc expression and calcium ion signaling pathway in GBM.

Gene function enrichment network analysis (cellular components) revealed functional associations among core protein complexes involved in transmembrane ion transport (**Fig. 25**). The network highlights several key nodes, including the Transporter Complex, Cation Channel Complex, Transmembrane Transporter Complex, and Ion Channel Complex. Notably, the calcium channel complex emerges as a central hub within the network topology, showing significant functional connections with all other complexes ($p < 0.01$). This underscores its pivotal role in coordinating transmembrane ion dynamics and maintaining cellular ion homeostasis. KEGG pathway enrichment analysis demonstrated that the calcium ion signaling pathway was significantly enriched among the differentially expressed genes ($p < 0.001$, FDR < 0.001) (**Fig. 13, 26**). The core genes of this pathway include voltage-gated calcium channels (e.g., CACNA1D and CACNA1A), calmodulin (CALM3), and transcriptional regulators such as NFATc1 and NFATc2. These components are integral to calcium-mediated signaling processes. Sankey plots further illustrates the multidimensional regulatory network involving NFATc1/c2, which integrates ion dynamics and signal transduction pathways (**Fig. 27**). Metal ion transmembrane transporters play a critical role in shuttling ions such as calcium, zinc, iron, and copper across cellular membranes, ensuring intracellular metal ion homeostasis. This equilibrium is fundamental to numerous biological processes, including enzyme regulation, signaling cascades, cellular structure maintenance, and gene expression modulation[42,43]. Calcium ions (Ca^{2+}), acting as intracellular second messengers, are increasingly recognized for their roles in promoting cancer proliferation, progression, drug resistance, and migration[44]. The nuclear factor of activated T cells (NFAT) acts as a calcium sensor, linking calcium signaling to developmental, growth-related, immune, and inflammatory pathways. Calcium influx triggers NFAT activation and its translocation to the nucleus, where its transcriptional targets drive cancer initiation and progression[45].

In this study, immunoblotting of chromatin-bound proteins showed that C2N8 hydrogel culture promoted the binding ability of NFATc1 and NFATc2 (**Fig. 28**). In addition, NFATc2 was significantly translocated to the nucleus in cells cultured in C2N8 hydrogels (**Fig. 29**). Furthermore, the mRNA levels of the transient receptor potential (TRP) channel superfamily were significantly upregulated in cells cultured on C2N8 hydrogel (**Fig. 30**). TRP channels form functional homo- or heterotetramers, enabling sodium and calcium ion influx and influencing cellular functions through

membrane excitability and intracellular calcium signaling. Importantly, TRP channels are regulated by tumor microenvironment components, such as acidosis (proton-rich conditions), and contribute to hypoxic responses[46].

Collectively, these findings demonstrate that C2N8 hydrogel induces a pro-oncogenic environment in GBM by activating ion transmembrane transporters, enhancing calcium influx, and facilitating NFAT nuclear translocation. This underscores the potential of C2N8 hydrogel in modulating ion dynamics and signaling pathways to influence GBM biology.

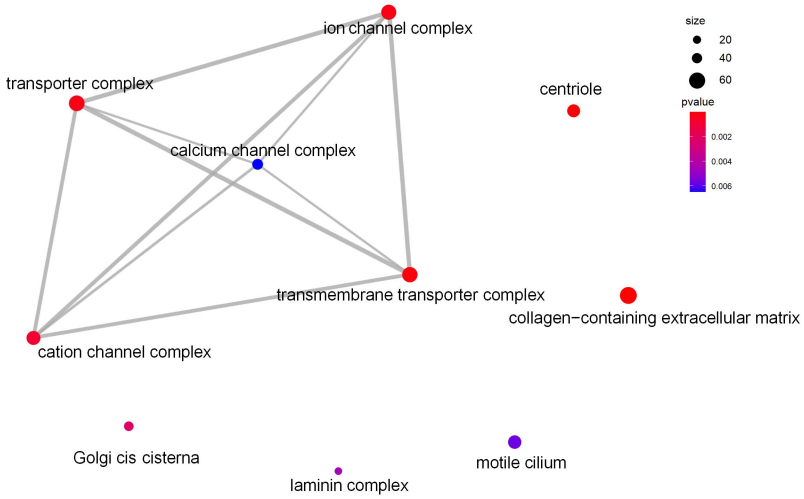

Figure 25. Correlation network of the cellular components enrichment functions on C2N8 hydrogel group.

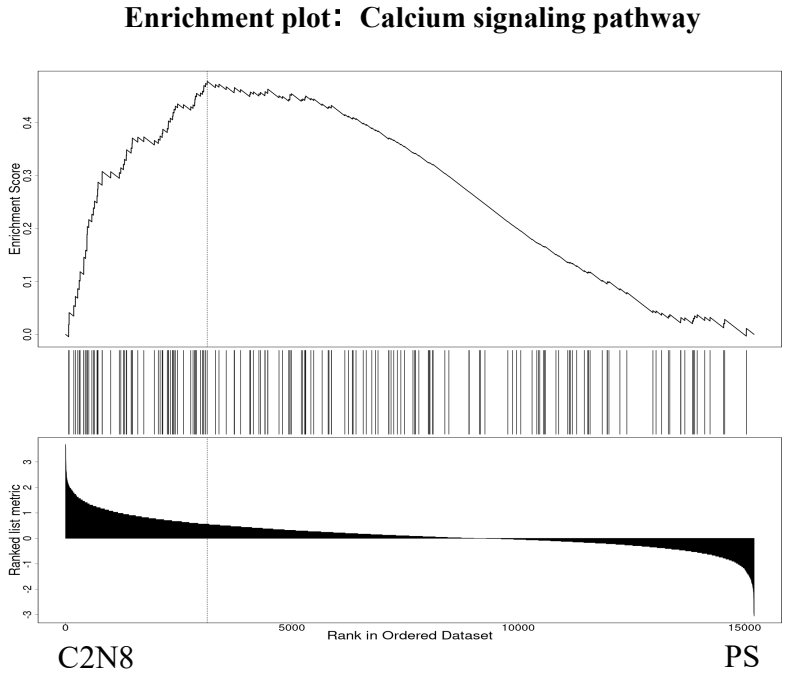

Figure 26. GSEA analysis of the differential expression C2N8 hydrogel gene set (metal ion transmembrane transpoter activity) is displayed

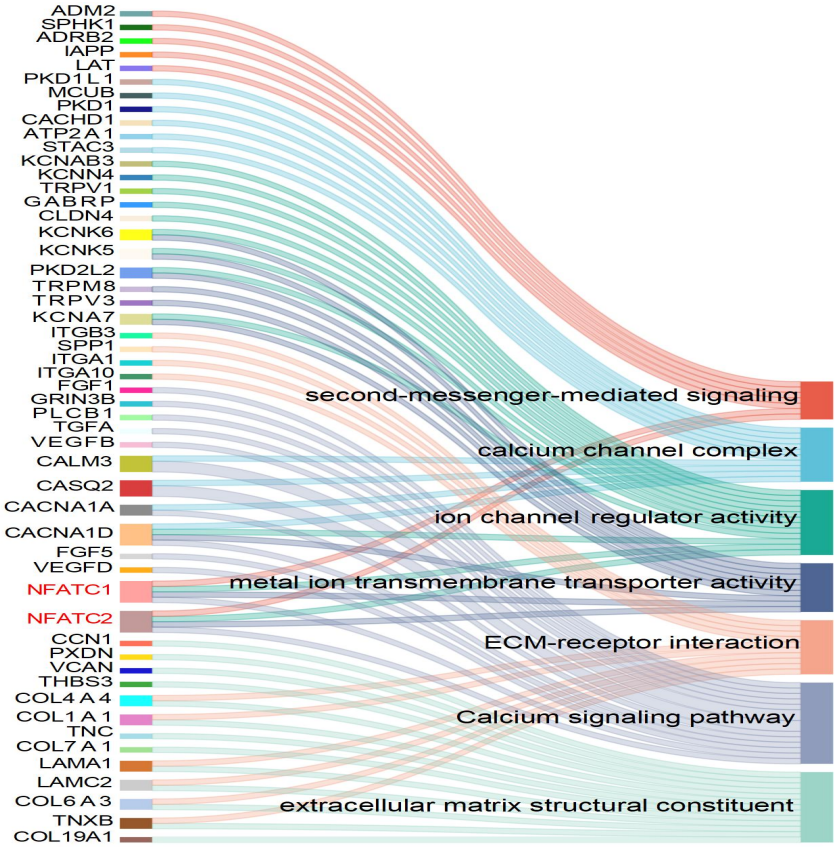

Figure 27. Sankey enrichment analysis on C2N8 hydrogel group.

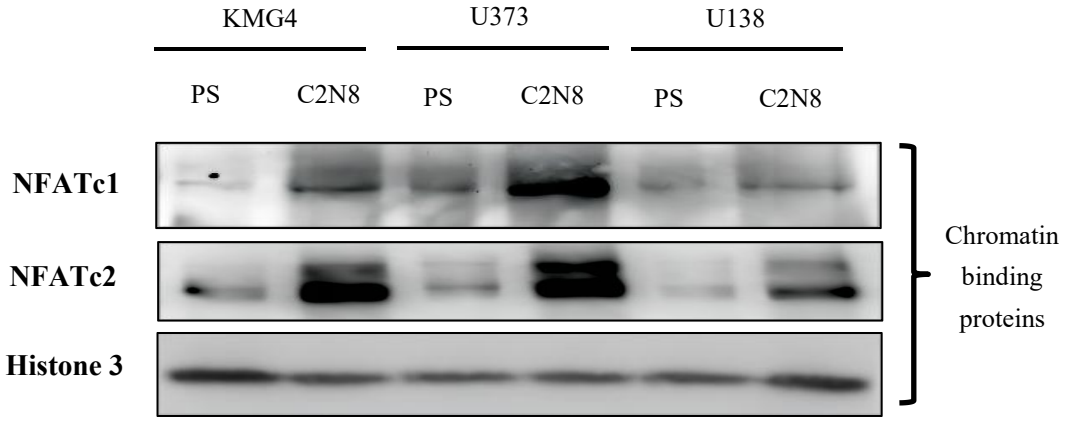

Figure 28. GSEA analysis of the differential expression C2N8 hydrogel gene set (metal ion transmembrane transpoter activity) is displayed

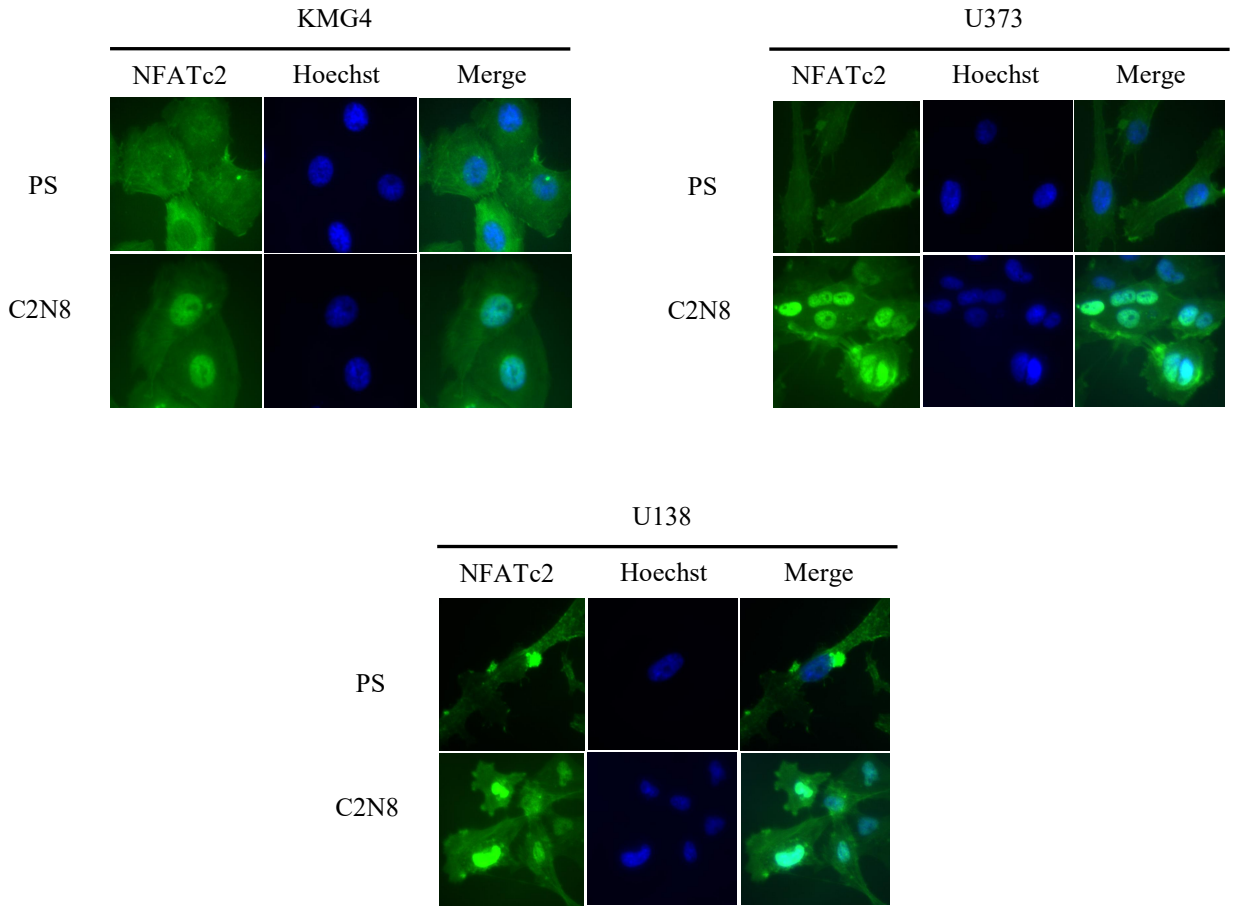

Figure 29. Immunofluorescence staining of NFATc2. Representative images are shown (magnification ×10). Scale bars, 50 μm

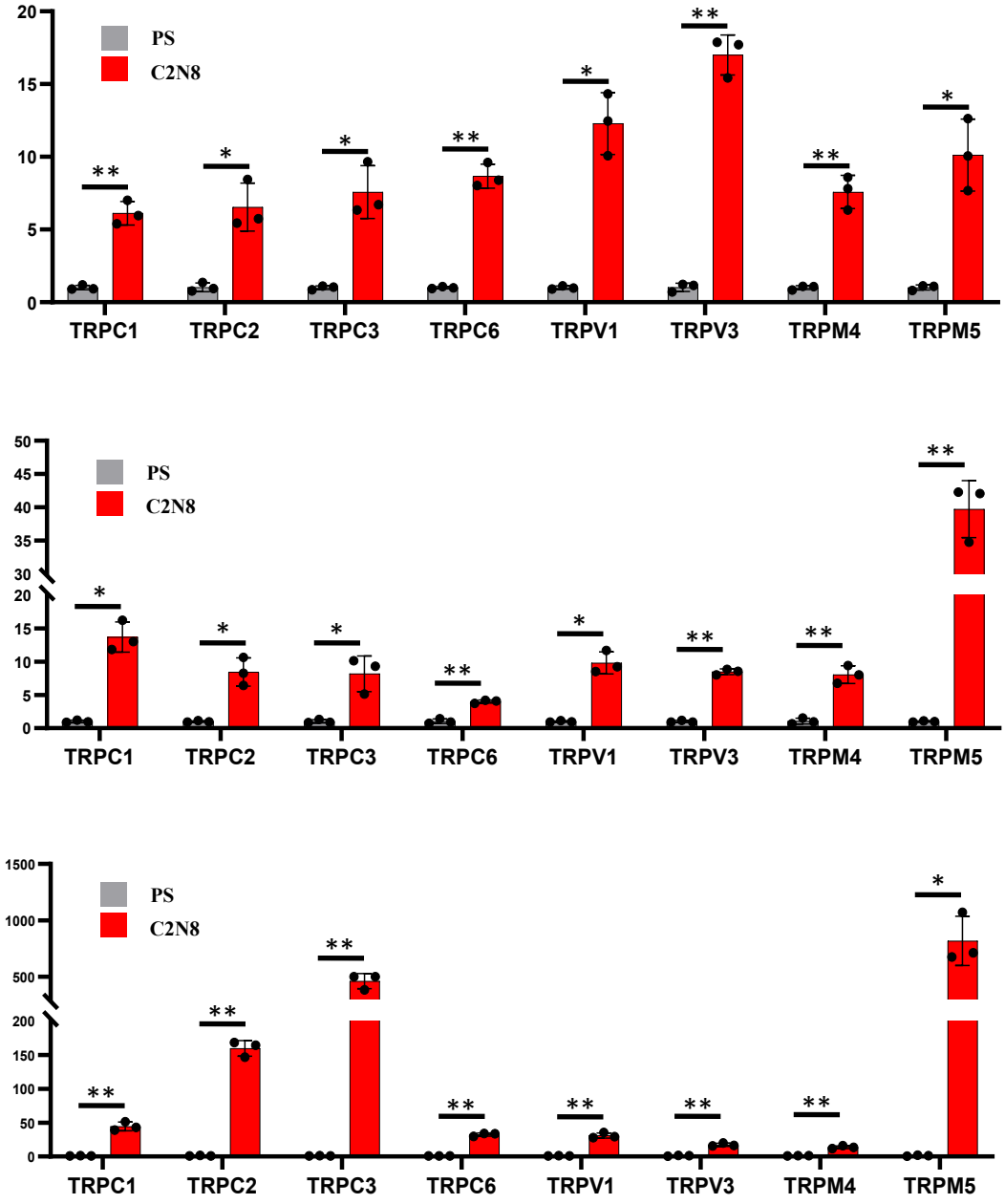

Figure 30. The cells were cultured on the PS dish and C2N8 hydrogel, and the mRNA expression levels of calcium channel such as *TRPC1*, *TRPC2*, *TRPC3*, *TRPC6*, *TRPV1*, *TRPV3*, *TRPM4* and *TRPM5* were examined by qRT-PCR.

4.7 NFATc1-transcribed c-Myc expression up-regulate SOX2 expression, leading to maintenance of stemness.

The Gene Set Enrichment Analysis (GSEA) revealed significant enrichment of pathways associated with c-Myc targets (**Fig. 11B, 31**). c-Myc is a critical regulator of glioma cancer stem cells[47] and is also implicated in maintaining the self-renewal capacity and chemotherapy resistance of colon cancer stem cells[48]. In this study, C2N8 hydrogel culture was shown to enhance c-Myc expression at both the mRNA and protein levels across three GBM cell lines (**Fig. 32, 33, 34**), highlighting the tumorigenic potential of c-Myc activation. To investigate the regulatory mechanism of NFATc1 in c-Myc transcription, we utilized the ISMARA database[49] to predict NFATc1 binding sequences (**Fig. 35A**). Subsequent analyses revealed that NFATc1 binds to multiple sites within the c-Myc promoter region, particularly 2 kilobases upstream of the transcription start site (**Fig. 35B**). Using the ENCODE database integrated into the UCSC Genome Browser, we further identified two distinct regions within the c-Myc promoter that are enriched for NFATc1 binding (**Fig. 36**), suggesting a potential role for NFATc1 in regulating c-Myc expression. To ascertain whether NFATc1 functions as a transcription factor for c-Myc in GBM cells, we conducted chromatin immunoprecipitation (ChIP)-qPCR assays using primers specific to the regions identified by the ENCODE database (**Fig. 37**). The ChIP-qPCR assay with an antibody against NFATc1 demonstrated a significant increase in immunoprecipitation within the c-Myc promoter region in the C2N8 hydrogel culture group compared to the PS control group across all three GBM cell lines (**Fig. 38**). These findings strongly suggest that calcium influx induces NFATc1 nuclear translocation, where it acts as a transcription factor to activate c-Myc expression. To further clarify the interplay between NFATc1, c-Myc, and the stemness factor Sox2, we performed knockdown experiments targeting NFATc1 and c-Myc in three GBM cell lines. qRT-PCR analysis confirmed a significant reduction in the expression of *NFATc1* and *c-Myc* upon siRNA treatment (**Fig. 39**). Western blotting of cell lysates from the C2N8 hydrogel group revealed that NFATc1 knockdown led to a reduction in both c-Myc and Sox2 protein levels. Conversely, c-Myc interference resulted in decreased Sox2 expression, while NFATc1 expression remained unaffected (**Fig. 40**). Collectively, these results confirm that c-Myc, acting downstream of NFATc1, is transcriptionally activated by NFATc1 and subsequently induces Sox2 expression, thereby maintaining the cancer stem cell phenotype.

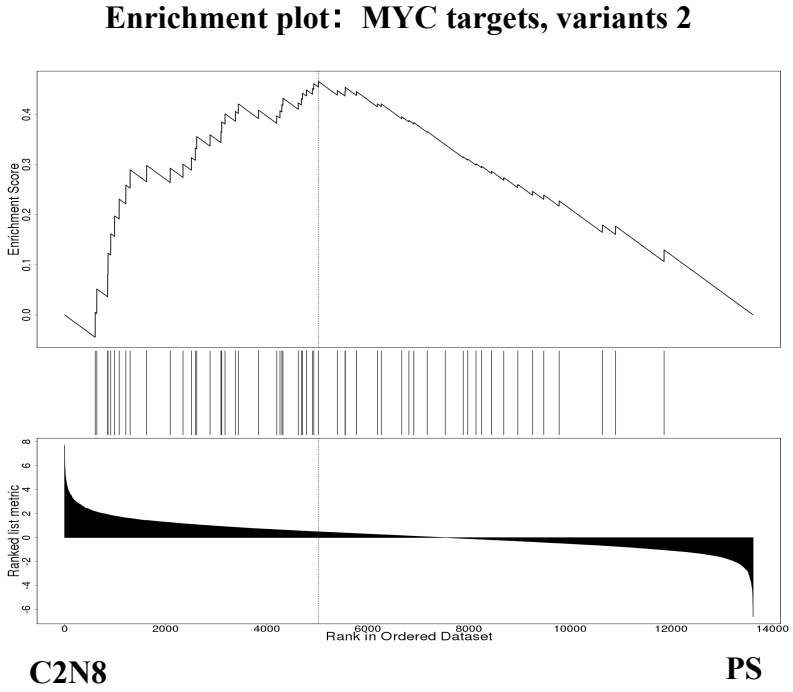

Figure 31. GSEA analysis of the differential expression C2N8 hydrogel gene set (MYC targets, variants 2) is displayed.

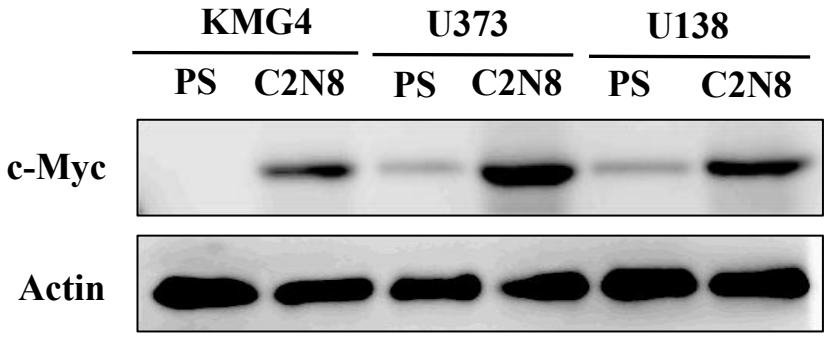

Figure 32. Western blotting shows that C2N8 hydrogel increased c-Myc levels in KMG4 cell, U373 and U138 cells.

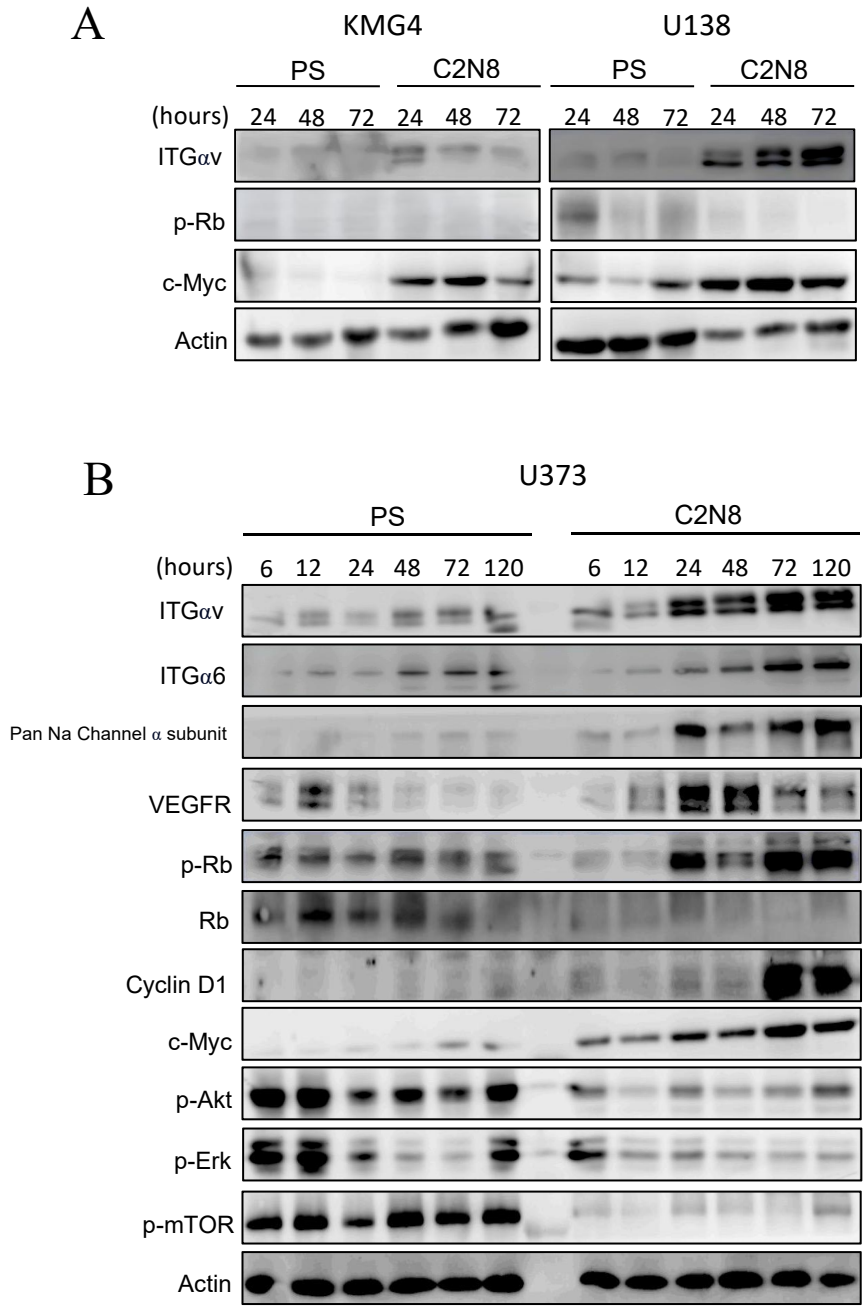

Figure 33. A KMG4 and U138 cells were cultured on PS dish and C2N8 hydrogel at 24, 48, and 72 hours, and subjected to Western blotting for ITGαv, p-Rb and c-Myc. **B** U373 cells were cultured on PS dish and C2N8 hydrogel at 6, 12, 24, 48, 72, 120 hours, and subjected to Western blotting for indicated molecules. Actin was used as a loading control.

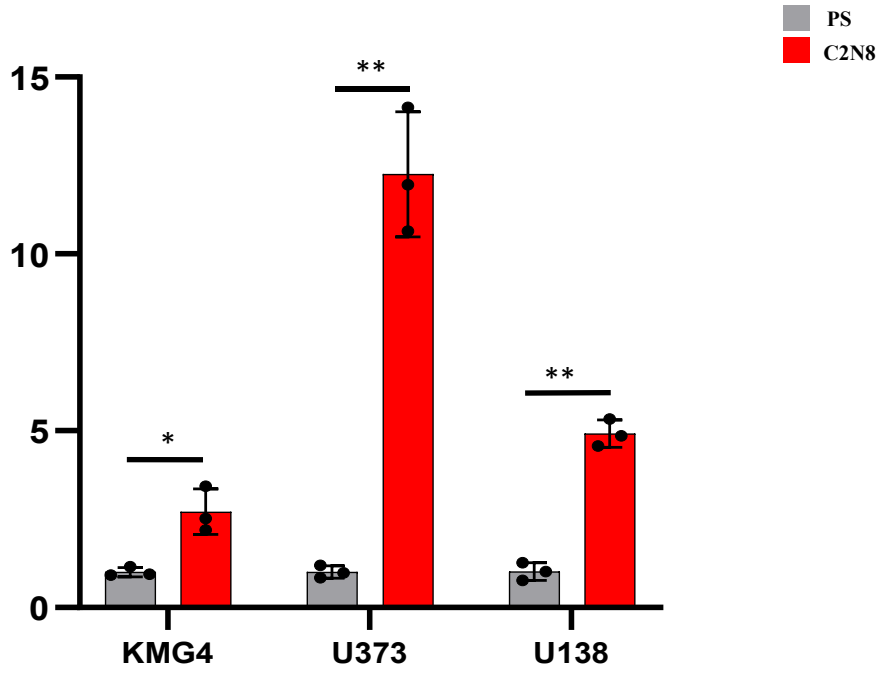

Figure 34. The KMG4, U373, and U138 cells were cultured on PS dish and C2N8 hydrogel, and the expression levels of c-Myc were examined by qRT-PCR.

A

B

Prediction of the sequence logo of NFATc1 by the ISMARA database

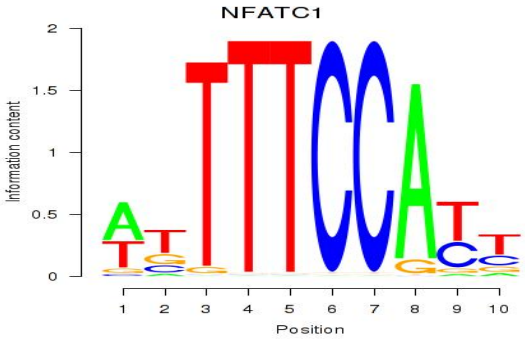

The binding sites of NFATc1 on the c-Myc promoter region were predicted by JASPAR

Name	Predicted sequence	Score
NFATc1	CATTTCCAAT	9.33267
	TTATTCCACG	8.647968
	AAGTTCCAGT	7.603209
	CCTTTCCAGG	7.4622316
	GTTTTCCTCC	7.4597917

Figure 35. A a Prediction of the sequence logo of NFATc1 by the ISMARA database. **B** The binding sites of NFATc1 on the c-Myc promoter region were predicted by JASPAR.

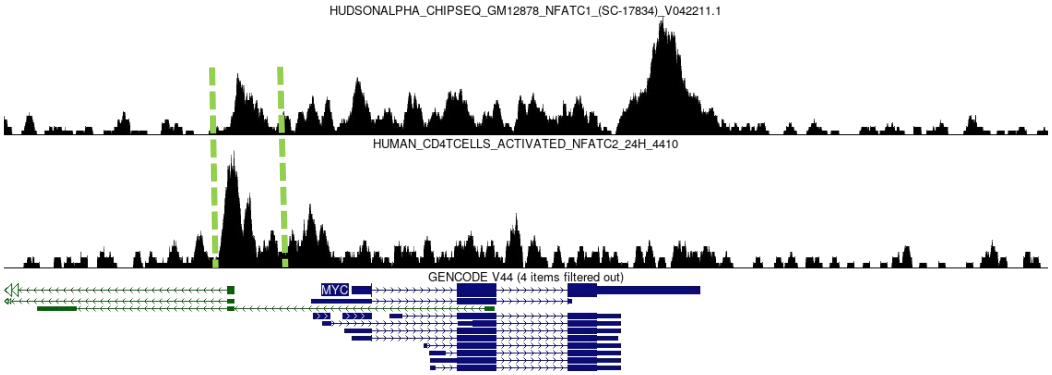

Figure 36. Chromatin occupancy of NFATc1 and NFATc2 at the c-Myc genomic locus. ChIP-seq profiles depict the distribution of NFATc1 (up) and NFATc2 (down) binding across the c-Myc locus (chr8:128,747,267-128,755,402, GRCh38/hg38).

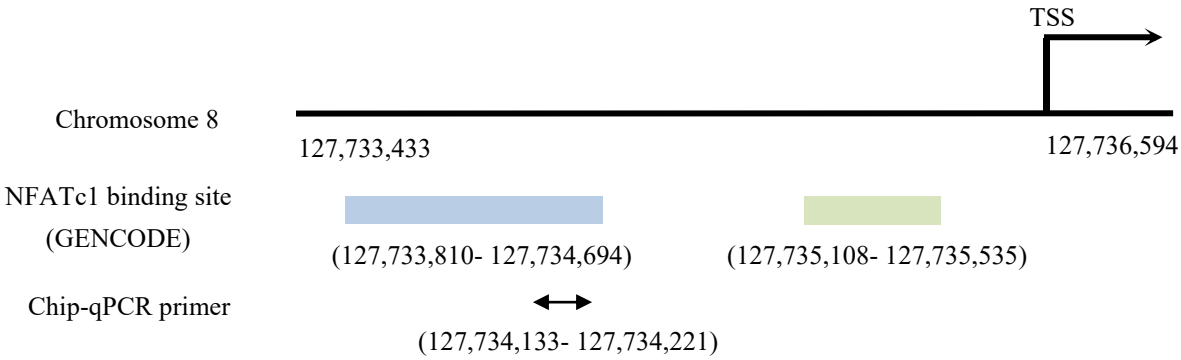

Figure 37. Schematics showing the three regions of NFATc1 enriched in the c-Myc promoter region by the GENCODE database.

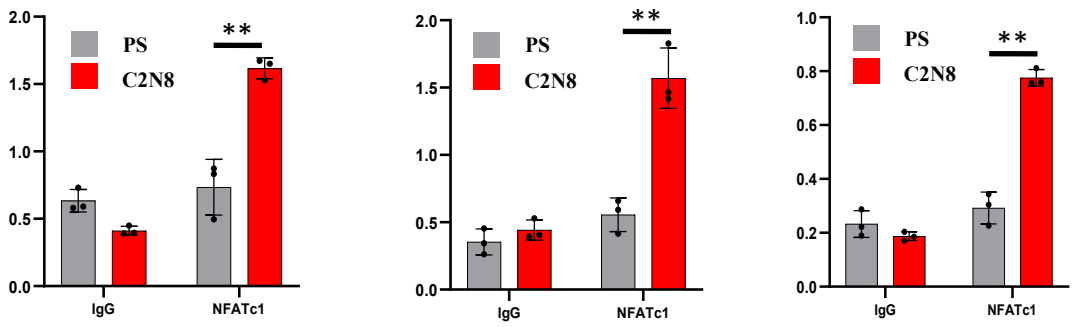

Figure 38. ChIP analysis was performed using an antibody against NFATc1 in KMG4, U373, and U138 cells cultured on control (PS) or C2N8 hydrogel. Normal IgG was used as a negative control.

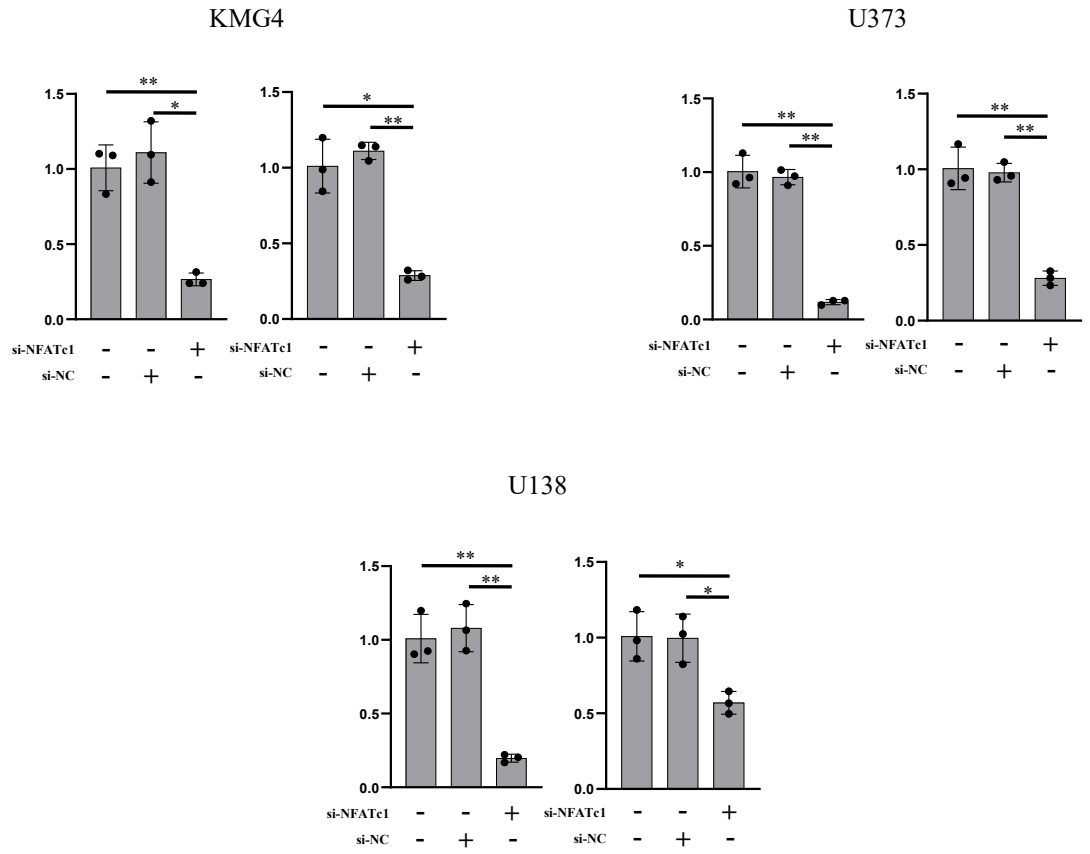

Figure 39. KMG4, U373, and U138 cells were transfected with or without si-NFATc1 or si-Myc, and the knock-down efficiencies were by qRT-PCR. The si-NC indicates negative control.

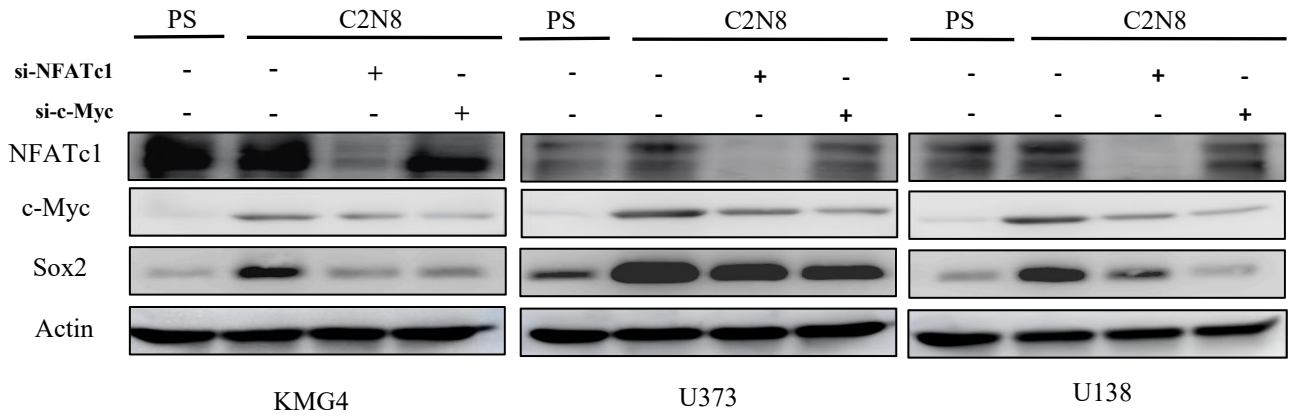

Figure 40. KMG4, U373, and U138 cells were transfected with or without si-NFATc1 and si-Myc on C2N8 hydrogel, and the expression levels of NFATc1, c-Myc, and SOX2 were examined by Western blotting. The cells cultured on PS dish was used as controls.

4.8 The GBM microenvironment *in vivo*.

To corroborate the clinical relevance and significance of c-Myc in glioblastoma stem cells (GSCs), spatial transcriptome analysis of c-Myc expression in human glioblastoma multiforme (GBM) tissue was conducted. The results were consistent with immunoblotting data (**Fig. 40**), revealing that c-Myc expression was generally low across the tumor tissue. However, notable elevation of c-Myc expression was observed in regions adjacent to palisading necrosis (cluster 2) and areas of microvascular proliferation (cluster 10), both hallmark features of GBM (**Fig. 41A, B**). Additionally, c-Myc expression was positively correlated with Nanog expression in these regions, further supporting its role in maintaining GSC characteristics. These findings were validated by immunohistochemical staining (**Fig. 41C**). Concomitantly, increased expression of vascular endothelial growth factor receptor (VEGFR) was observed in the U373 cell line cultured on C2N8 hydrogel (**Fig. 33B**). As a critical component of the GSC niche, the tumor vasculature plays a pivotal role in sustaining the tumor mass and promoting tumor margin invasion. Emerging evidence suggests that distinct vascular properties within these regions may induce unique functional states in resident GSCs, giving rise to heterogeneous subpopulations[50]. Furthermore, hypoxia has been identified as a key factor in maintaining GSCs and orchestrating their responses to the necrotic tumor microenvironment. Within human tumor tissues, a small fraction of cancer stem cells (CSCs) (approximately 1-2%) resides in a hypoxic necrotic niche (proton enrichment), which endows them with metastatic potential[51]. This hypoxic microenvironment provides a favorable setting for CSC migration and metastatic dissemination, underscoring its importance in tumor progression and therapeutic resistance. Together, these findings highlight the interplay between c-Myc, the tumor vasculature, and hypoxic conditions in shaping the behavior of GSCs within the GBM tumor ecosystem.

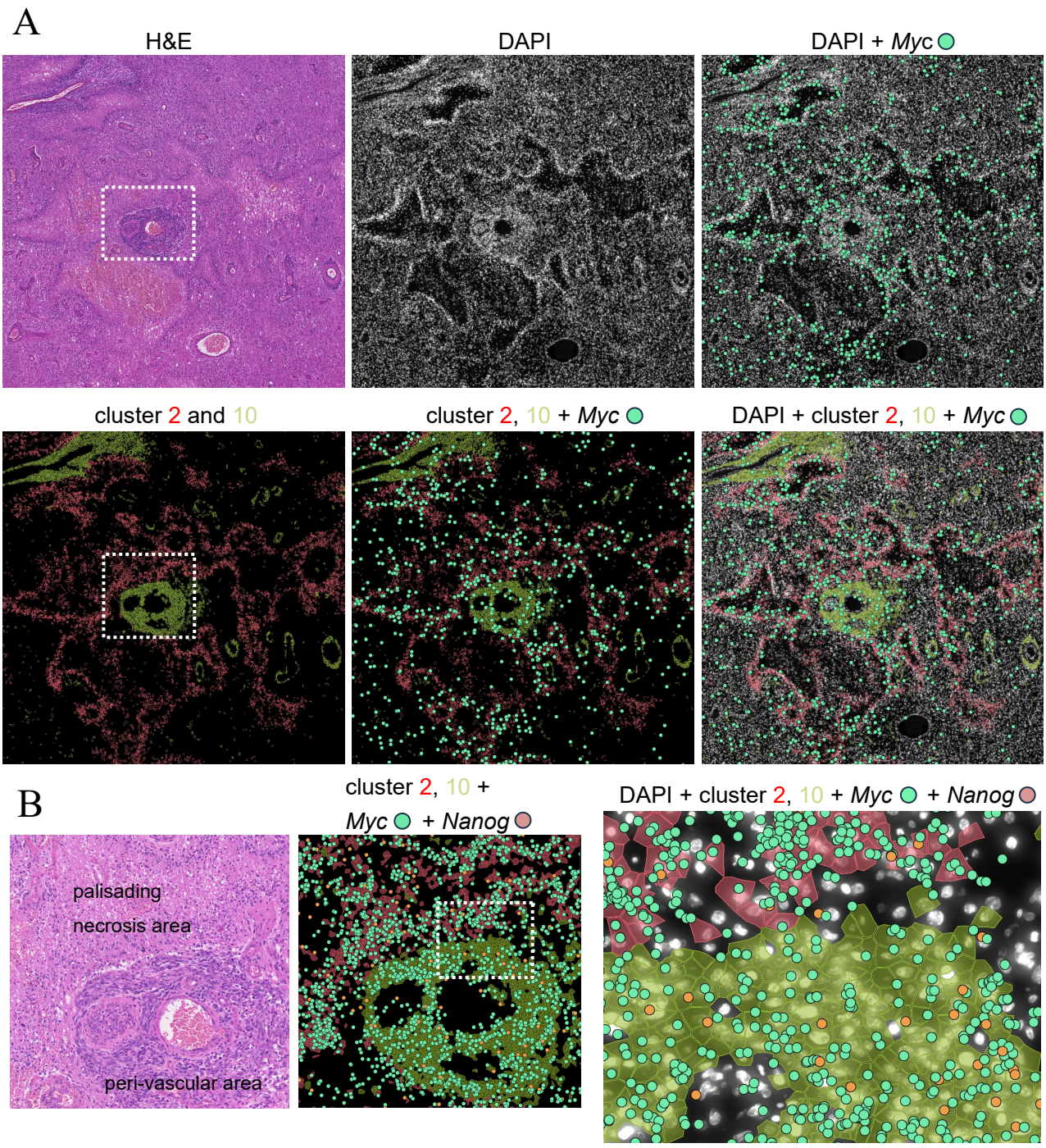
A
H&E
DAPI
DAPI + Myc
cluster 2 and 10
cluster 2, 10 + Myc
DAPI + cluster 2, 10 + Myc
B
cluster 2, 10 +
Myc + Nanog
DAPI + cluster 2, 10 + Myc + Nanog
palisading
necrosis area
peri-vascular area
C
c-MYC
c-MYC
palisading
necrosis area
peri-vascular area

Figure 41. A, B Human glioblastoma tissue with representative pathological features such as palisading necrosis (cluster 2) and perivascular region (cluster 10) were subjected to spatial-transcriptome analysis by Xenium, and *c-myc* expression was examined. **B** shows an enlarged image of the squared area in **A**. **C** IHC for c-Myc in glioblastoma clinical sample are shown. Brown colours indicate the expression of c-Myc.

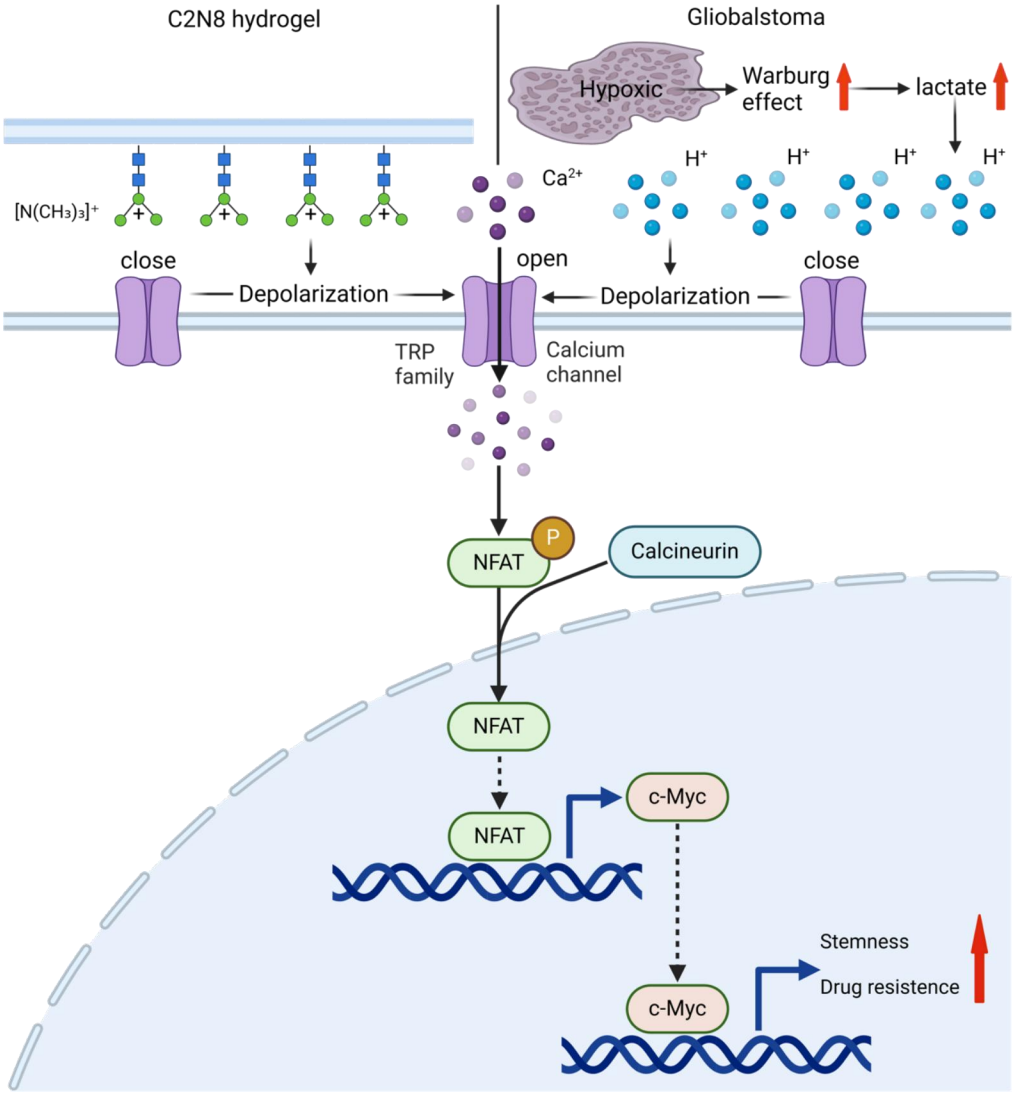

Figure 42. The positive ζ potential/calcium ion/NFAT/c-Myc axis in the context of GSCs. The c-Myc regulates the expression of stemness markers and genes involved in drug resistance in GSCs. Cationic C2N8 hydrogels developed in this study are useful for simulating the in vivo electric field microenvironment conducive to GSC development.

5. Discussion

GBM is characterized by pronounced intra-tumoral heterogeneity, and CSCs have been recognized as pivotal contributors to this complexity. The acquisition of stem cell properties is driven by genetic modifications and interactions within the tumor microenvironment (TME)[52]. The complex molecular mechanisms underlying CSCs generation in response to the stem cell niche and the signaling pathways leading to it have yet to be fully elucidated. Therefore, the elucidation of the complex dynamics of the stem cell niche and how microenvironments affects stem cell fate is crucial for the exploration of novel GBM treatment paradigms. Biomaterials serve as scaffolds, providing a complex environment for stem cell generation and growth. In physiological contexts, stem cells undergo differentiation into diverse tissues and organs, thus garnering considerable attention in highlighting their therapeutic potential. In tumors, to enhance the control of CSCs generation and differentiation, a deeper understanding of complex tissue development is essential, coupled with the strategic use of smart biomaterials that mimic various tumor microenvironments.

In our study, the impact of ζ potential heterogeneity on GSCs within *in vivo* tumor tissues was examined using hydrogels with distinct charges. Our findings revealed that cationic hydrogels can directly regulate the expression of stem-like phenotypes through cellular mechanical transduction. An extracellular positive ζ potential induces cell depolarization, stimulates the activity of transmembrane metal ion transporters, and promotes calcium influx, which activates NFAT and induces the transcription of the oncogene c-Myc, leading to cellular dedifferentiation, epithelial-mesenchymal transition, and drug resistance (**Fig. 42**). Study has revealed that membrane depolarization inhibits stem cell differentiation and plays a critical role in cytoskeletal remodelling[53]. Collagen I is abundant in vertebrates and a major component of the extracellular matrix (ECM), contributes to structural integrity and mechanical resilience. In an acidic environment, the positively charged groups on collagen are protonated, further enhancing the positive charge of collagen molecule[54]. Hypoxia is known to augment the Warburg effect in GBM cells, leading to the accumulation of lactic acid and the excretion of extracellular hydrogen ions, creating a cation-enriched acidic environment that promotes tumor cell invasion and metastasis[55,56]. At the same time, hypoxia depolarizes the cell membrane and opens voltage-gated calcium channels, leading to calcium influx[57]. An increase in intracellular Ca^{2+} activates the phosphatase calcineurin,

which dephosphorylates nuclear factor of activated T cells (NFAT). Thereafter, the dephosphorylated NFAT is translocated into the nucleus, where it induces the expression of lots of genes involved in various cellular pathways[58]. Therefore, the inherent bioelectrical properties of the tumor microenvironment promote the maintenance and dissemination of CSCs.

Despite the elucidation of the role of positive ζ potential in promoting cancer progression in neurological malignancies, the underlying mechanisms remain obscure. Here, through RNA sequencing and Gene Set Enrichment Analysis (GSEA), we identified metal ion transmembrane transporters and c-Myc targets as the most enriched pathways in GSC-like cells cultured on C2N8 hydrogels compared to PS controls.

Calcium signaling pathways are central to GBM progression, regulating diverse cellular functions, although the underlying regulatory mechanisms are yet to be fully elucidated[59]. Our studies revealed that calcium influx activates the nuclear translocation of NFAT, leading to c-Myc transcription and upregulating stem cell factors, and promoting GBM dedifferentiation, drug resistance, and EMT. EMT was once considered to be a critical event in cancer cell metastasis[60], but is now recognized for its role in chemotherapy resistance[61]. In this study, we revealed that C2N8 hydrogel induces a complex cellular response characterized by the inhibition of key growth pathways (Akt, Erk, mTOR) (**Fig. 33**) and the upregulation of stem cell characteristics, drug tolerance, and migration in cultured cells. This suggests a potential mechanism for controlling cell growth and differentiation, with implications for both cancer therapy and regenerative medicine. The findings highlight the need for further investigation into the specific properties of C2N8 hydrogel and its potential applications in biomedical research and clinical settings. Our findings demonstrated that C2N8 hydrogel upregulated the expression of integrin α6 (ITGA6) and integrin αv (ITGAV) (**Fig. 33A, B**). ITGA6 expression promotes EMT and metastasis *via* demethylation of NFATc2 gene, and is directly influenced by hypoxia-inducible factors to enhance tumor stem cell activity and aggressiveness[62,63]. ITGAV, a key gene in EMT, facilitates the enhancement of tumor cell migration and invasion when upregulated[64,65]. In addition, SDS-PAGE analysis of proteins extracted from U373 cells cultured on C2N8 hydrogel revealed two prominent protein bands, S1 and S2 (**Fig. 18A, B**), which were more intense compared to PS control and A5N5 hydrogel samples. LC-MS/MS analysis identified S1 as Filamin A (FLNA) (**Fig. 18A, B**). The upregulation of FLNA is associated

with Snail-induced EMT, where Snail represses E-cadherin, a key molecule in cell adhesion, promoting a more invasive cell phenotype[66]. We also noted the upregulation of p-Rb was observed in U373 cells, but not in the KMG4 and U138 cells cultured on C2N8 hydrogel (**Supplementary Fig. 33A, B**), a cell cycle regulatory protein involved in the proliferation and aggressiveness of CSCs. Rb phosphorylation promotes EMT and enhances CSC properties[67,68]. At the same time, c-Myc induces tumor cells to undergo EMT through the regulation of multiple signal pathways and transcription factors, and promotes tumor invasion and metastasis[69].

In summary, our findings reveal the previously unknown significance of the positive ζ potential/calcium ion/NFAT/c-Myc axis in the context of GSCs (**Fig. 42**), and delineates a method utilizing cationic C2N8 hydrogels to simulate the *in vivo* acidic field microenvironment conducive to GSC development. The further development of this approach is promising as a novel diagnostic and therapeutic target for clinical GBM therapy, providing new avenues for the treatment of this complex and aggressive malignancy.

6. References

1. Grech N. et al. Rising Incidence of Glioblastoma Multiforme in a Well-Defined Population. *Cureus* **12,** e8195(2020).

2. Wilson TA, Karajannis MA, Harter DH. Glioblastoma multiforme: State of the art and future therapeutics. *Surg Neurol Int* **5,** 64(2014).

3. Stupp, R. et al. Radiotherapy plus concomitant and adjuvant temozolomide for glioblastoma. *N Engl J Med* **352,** 987-996(2005).

4. Abadi B, Ahmadi-Zeidabadi M, Dini L, Vergallo C. Stem cell-based therapy treating glioblastoma multiforme. *Hematol Oncol Stem Cell Ther* **14,** 1-15(2021).

5. Biserova K, Jakovlevs A, Uljanovs R, Strumfa I. Cancer Stem Cells: Significance in Origin, Pathogenesis and Treatment of Glioblastoma. *Cells* **10,** 621 (2021)

6. Xie XP. et al. Quiescent human glioblastoma cancer stem cells drive tumor initiation, expansion, and recurrence following chemotherapy. *Dev Cell* **57,** 32-46(2022).

7. Charles N. et al. Perivascular nitric oxide activates notch signaling and promotes stem-like character in PDGF-induced glioma cells. *Cell Stem Cell* **6,** 141-152(2010).

8. Jhaveri N, Chen TC, Hofman FM. Tumor vasculature and glioma stem cells: Contributions to glioma progression. *Cancer Lett* **380,** 545-551(2016).

9. Li Z. et al. Hypoxia-inducible factors regulate tumorigenic capacity of glioma stem cells. *Cancer Cell* **15,** 501-513(2009).

10. Eyler CE. et al. Glioma stem cell proliferation and tumor growth are promoted by nitric oxide synthase-2. *Cell* **146,** 53-66(2011).

11. Chen X. et al. ADAM17 promotes U87 glioblastoma stem cell migration and invasion. *Brain Res* **1538,** 151-158(2013).

12. Seliktar D. Designing cell-compatible hydrogels for biomedical applications. *Science* **336,** 1124-1128(2012).

13. Tibbitt MW, Anseth KS. Hydrogels as extracellular matrix mimics for 3D cell culture. *Biotechnol Bioeng* **103,** 655-663(2009).

14. Lutolf MP, Hubbell JA. Synthetic biomaterials as instructive extracellular microenvironments for morphogenesis in tissue engineering. *Nat Biotechnol* **23,** 47-55(2005).

15. Mauretti A. et al. Design of a Novel Composite H2 S-Releasing Hydrogel for Cardiac Tissue Repair. *Macromol Biosci* **16,** 847-858(2016).

16. Loessner D. et al. Bioengineered 3D platform to explore cell-ECM interactions and drug resistance of epithelial ovarian cancer cells. *Biomaterials* **31,** 8494-8506(2010).

17. Caliari SR, Burdick JA. A practical guide to hydrogels for cell culture. *Nat Methods* **13,** 405-414(2016).

18. Gilbert PM. et al. Substrate elasticity regulates skeletal muscle stem cell self-renewal in culture. *Science* **329,** 1078-1081(2010).

19. Cosgrove BD. et al. Rejuvenation of the muscle stem cell population restores strength to injured aged muscles. *Nat Med* **20,** 255-264(2014).

20. Yosef A. et al. Fibrinogen-Based Hydrogel Modulus and Ligand Density Effects on Cell Morphogenesis in Two-Dimensional and Three-Dimensional Cell Cultures. *Adv Healthc Mater* **8,** e1801436(2019).

21. Suzuka J. et al. Rapid reprogramming of tumour cells into cancer stem cells on double-network hydrogels. *Nat Biomed Eng* **5,** 914-925(2021).

22. Watt FM, Huck WT. Role of the extracellular matrix in regulating stem cell fate. *Nat Rev Mol Cell Biol* **14,** 467–473(2013).

23. Saha K. et al. Substrate modulus directs neural stem cell behavior. *Biophys J* **95,** 4426–4438(2008).

24. Li H, Sun Y, Li Q, Luo Q, Song G. Matrix Stiffness Potentiates Stemness of Liver Cancer Stem Cells Possibly via the Yes-Associated Protein Signal. *ACS Biomater Sci Eng* **8,** 598-609(2022).

25. Li M. et al. Activation of Piezo1 contributes to matrix stiffness-induced angiogenesis in hepatocellular carcinoma. *Cancer Commun (Lond)* **42,** 1162-1184(2022).

26. Funk RH. Endogenous electric fields as guiding cue for cell migration. *Front Physiol* **6,** 143(2015).

27. Blackiston DJ, McLaughlin KA, Levin M. Bioelectric controls of cell proliferation: ion channels, membrane voltage and the cell cycle. *Cell Cycle* **8,** 3527-3536(2009).

28. Matos MA, Cicerone MT. Alternating current electric field effects on neural stem cell viability and differentiation. *Biotechnol Prog* **26,** 664-670(2010).

29. Samal SK. et al. Cationic polymers and their therapeutic potential. *Chem Soc Rev* **41,** 7147-7194(2012).

30. Takahashi K, Yamanaka S. Induction of pluripotent stem cells from mouse embryonic and adult fibroblast cultures by defined factors. *Cell* **126,** 663-676(2006).

31. Hassn Mesrati M, Syafruddin SE, Mohtar MA, Syahir A. CD44: A Multifunctional Mediator of Cancer Progression. *Biomolecules* **11,** 1850(2021).

32. Barzegar Behrooz A, Syahir A, Ahmad S. CD133: beyond a cancer stem cell biomarker. *J Drug Target* **27,** 257-269(2019).

33. Xu X. et al. Aldehyde dehydrogenases and cancer stem cells. *Cancer Lett* **369,** 50-57(2015).

34. Loh CY. et al. The E-Cadherin and N-Cadherin Switch in Epithelial-to-Mesenchymal Transition: Signaling, Therapeutic Implications, and Challenges. *Cells* **8,** 1118(2019).

35. Usman S. et al. Vimentin Is at the Heart of Epithelial Mesenchymal Transition (EMT) Mediated Metastasis. *Cancers (Basel)* **13,** 4985(2021).

36. Robey RW. et al. Revisiting the role of ABC transporters in multidrug-resistant cancer. *Nat Rev Cancer* **18,** 452-464(2018).

37. Ezierzański M. et al. Temozolomide (TMZ) in the Treatment of Glioblastoma Multiforme-A Literature Review and Clinical Outcomes. *Curr Oncol* **31,** 3994-4002(2024).

38. Bhandarkar S, Prabhakar B, Shende P. Quercetin-loaded platelets as a potential targeted therapy for glioblastoma multiforme cell line U373-MG. *Biotechnol J* **16,** e2100271(2021).

39. Kohsaka S. et al. STAT3 inhibition overcomes temozolomide resistance in glioblastoma by downregulating MGMT expression. *Mol Cancer Ther* **11,** 1289-1299(2012).

40. Kukal S. et al. Multidrug efflux transporter ABCG2: expression and regulation. *Cell Mol Life Sci* **78,** 6887-6939(2021).

41. Chen YC. et al. Pharmacological agents targeting drug-tolerant persister cells in cancer. *Pharmacol Res* **203,** 107163(2024).

42. Sun C. et al. Structural insights into the calcium-coupled zinc export of human ZnT1. *Sci Adv* **10,** eadk5128(2024).

43. Zhang MK. et al. Cytomembrane-Mediated Transport of Metal Ions with Biological Specificity. *Adv Sci (Weinh)* **6,** 1900835(2019).

44. Singh J, Meena A, Luqman S. New frontiers in the design and discovery of therapeutics that target calcium ion signaling: a novel approach in the fight against cancer. *Expert Opin Drug Discov* **18,** 1379-1392(2023).

45. Jiang Y. et al. NFAT1-Mediated Regulation of NDEL1 Promotes Growth and Invasion of Glioma Stem-like Cells. *Cancer Res* **79,** 2593-2603(2019).

46. Audero MM, Prevarskaya N, Fiorio Pla A. Ca2+ Signalling and Hypoxia/Acidic Tumour Microenvironment Interplay in Tumour Progression. *Int J Mol Sci* **23,** 7377(2022).

47. Wang J. et al. c-Myc is required for maintenance of glioma cancer stem cells. *PLoS One* **3,** e3769(2008).

48. Zhang HL, Wang P, Lu MZ, Zhang SD, Zheng L. c-Myc maintains the self-renewal and chemoresistance properties of colon cancer stem cells. *Oncol Lett* **17,** 4487-4493(2019).

49. Artimo P. et al. The ISMARA client. *F1000Res* **5,** ELIXIR-2851(2016).

50. Brooks LJ, Parrinello S. Vascular regulation of glioma stem-like cells: a balancing act. *Curr Opin Neurobiol* **47,** 8-15(2017).

51. Papale M. et al. Hypoxia, Inflammation and Necrosis as Determinants of Glioblastoma Cancer Stem Cells Progression. *Int J Mol Sci* **21,** 2660(2020).

52. Prasetyanti PR, Medema JP. Intra-tumor heterogeneity from a cancer stem cell perspective. *Mol Cancer* **16,** 41(2017).

53. Fennelly C, Wang Z, Criswell T, Soker S. Sustained Depolarization of the Resting Membrane Potential Regulates Muscle Progenitor Cell Growth and Maintains Stem Cell Properties In Vitro. *Stem Cell Rev Rep* **12,** 634-644(2016).

54. Uquillas JA, Akkus O. Modeling the electromobility of type-I collagen molecules in the electrochemical fabrication of dense and aligned tissue constructs. *Ann Biomed Eng* **40,** 1641-1653(2012).

55. Monteiro AR, Hill R, Pilkington GJ, Madureira PA. The Role of Hypoxia in Glioblastoma Invasion. *Cells* **6,** 45(2017).

56. Hjelmeland AB. et al. Acidic stress promotes a glioma stem cell phenotype. *Cell Death Differ* **18,** 829-840(2011).

57. Shimoda LA, Sham JS, Shimoda TH, Sylvester JT. L-type Ca(2+) channels, resting [Ca(2+)](i), and ET-1-induced responses in chronically hypoxic pulmonary myocytes. *Am J Physiol Lung Cell Mol Physiol* **279,** 884-894(2000).

58. Lin Y. et al. NFAT signaling dysregulation in cancer: Emerging roles in cancer stem cells. *Biomed Pharmacother* **165,** 115167(2023).

59. Leclerc C. et al. Calcium signaling orchestrates glioblastoma development: Facts and conjunctures. *Biochim Biophys Acta* **1863,** 1447-1459(2016).

60. Celià-Terrassa T, Kang Y. How important is EMT for cancer metastasis? *PLoS Biol* **22,** e3002487(2024).

61. Fischer KR. et al. Epithelial-to-mesenchymal transition is not required for lung metastasis but contributes to chemoresistance. *Nature* **527,** 472-476(2015).

62. Zhang J. et al. NFAT1 Hypermethylation Promotes Epithelial-Mesenchymal Transition and Metastasis in Nasopharyngeal Carcinoma by Activating ITGA6 Transcription. *Neoplasia* **21,** 311-321(2019).

63. Lathia JD. et al. Integrin alpha 6 regulates glioblastoma stem cells. *Cell Stem Cell* **6,** 421-432(2010).

64. Lopez-Cerda M. et al. IGF1R signaling induces epithelial-mesenchymal plasticity via ITGAV in cutaneous carcinoma. *J Exp Clin Cancer Res* **43,** 211(2024).

65. Taheri Baghmisheh S. et al. CASZ1 promotes migration, invasion, and metastasis of lung cancer cells by controlling expression of ITGAV. *Am J Cancer Res* **13,** 176-189(2023).

66. Savoy RM, Ghosh PM. The dual role of filamin A in cancer: can't live with (too much of) it, can't live without it. *Endocr Relat Cancer*, **20,** 341-356(2013).

67. Ho CM, Chang TH, Yen TL, Hong KJ, Huang SH. Collagen type VI regulates the CDK4/6-p-Rb signaling pathway and promotes ovarian cancer invasiveness, stemness, and metastasis. *Am J Cancer Res* **11,** 668-690(2021).

68. Huang P. et al. BMP-2 induces EMT and breast cancer stemness through Rb and CD44. *Cell Death Discov* **3,** 17039(2017).

69. Lin X. et al. C-myc overexpression drives melanoma metastasis by promoting vasculogenic mimicry via c-myc/snail/Bax signaling. *J Mol Med (Berl)* **95,** 53-67(2017).

70. Subramanian A. et al. Gene set enrichment analysis: a knowledge-based approach for interpreting genome-wide expression profiles. *Proc Natl Acad Sci U S A* **102,** 15545-15550(2005).

7. Acknowledgments

This research was financially supported by the Japan Society for the Promotion of Science (JSPS) KAKENHI Grants (Numbers JP19H01171 and JP24H00037, ST; JP21H03802 and JP24K03245, MT), AMED (20cm0106571h0001, 21cm0106571h0002, and 24ama221532h0001, S.T.), and JST SPRING, Grant Number JPMJSP2119. Institute for Chemical Reaction Design and Discovery (ICReDD) was established by World Premier International Research Initiative (WPI), MEXT, Japan. We acknowledge the technical support by the Laboratory of Soft & Wet Matter in Hokkaido University. We gratefully acknowledge all the GBM patients involved in the study.

.

Chapter 2

Mechanochemistry Induced Universal Hydrogel Surface Modification for Orientation and Enhanced Differentiation of Skeletal Muscle Myoblasts

Table of Contents

1. Abstract

Micropatterned surface substrates containing topographic cues offer the possibility of programming tissue organization as a cell template by guiding cell alignment, adhesion, and function. In this study, we developed and used a force stamp method to grow aligned micropatterns with tunable chemical properties and elasticity on the surface of hydrogels based on a force-triggered polymerisation mechanism of double-network hydrogels to elucidate the underlying mechanisms by which cells sense and respond to their mechanical and chemical microenvironments. In this work, we describe the impact of aligned micropatterns on the combined effects of microstructural chemistry and mechanics on the selective adhesion, directed migration, and differentiation of myoblasts. Our investigations revealed that topographically-engineered substrates with hydrophobic and elevated surface roughness significantly enhanced myoblast adhesion kinetics. Concurrently, spatially ordered architectures facilitated cytoskeletal reorganization in myocytes, establishing biomechanically favorable niches for syncytial myotube development through extracellular matrix (ECM) physical guidance. Reverse transcription PCR analysis and immunofluorescence revealed that the expression of differentiation-specific genes, myosin heavy chain, and myogenic regulatory factors *Myf5* and *MyoD* were upregulated in muscle cells on the aligned patterned scaffolds. These results suggest that the aligned micropatterns can promote muscle cell differentiation, making them potential scaffolds for enhancing skeletal differentiation.

Abbreviations

ANS: 8-aniline-1-naphthalenesulfonic acid

DN: double-network

ECM: extracellular matrix

EDTA: ethylenediaminetetraacetic acid

GFP: green fluorescent protein

hUC-MSCs: human umbilical cord mesenchymal stem cells

LCST: lower critical solution temperature

MyoD: Myoblast Determination Protein 1

MHC: myosin heavy chain

Myf5: myogenic Factor 5

MRF: myogenic regulatory factor

PNaAMPS: poly(2-acrylamido-2-methylpropanesulfonic acid sodium salt)

PNIPAm: poly(N-isopropylacrylamide)

PFA: paraformaldehyde

PAAm:polyacrylamide

qRT-PCR: Quantitative real time PCR

2. Introduction

Skeletal muscle damage due to trauma, myopathy, or tumor resection may impair muscle function and mobility, requiring the reconstruction of muscle tissue. Although skeletal muscle has a high regenerative capacity, the availability and morbidity of donor muscle tissue often limit the effectiveness of reconstructive surgery[1]. Muscle tissue regeneration using tissue-engineered extracellular matrix (ECM) scaffolds is a promising alternative solution for the treatment of defective or diseased skeletal muscle[2,3]. Since in *vivo* cellular behavior is critically reliant on tissue-specific microenvironments characterized by spatial architecture and mechanical rigidity, optimal muscle-inducing scaffolds must be engineered to deliver precise topographical patterns and biochemical signals that orchestrate cell-material interplay. The structure and orientation of myofibers in skeletal muscle tissue determine tissue function, and the organized alignment of muscle cells is essential for the formation of myotubes, which play a key role in myogenesis[4]. The ECM is pivotal in cell proliferation and differentiation and serves as an essential scaffold for cell adhesion, proliferation, and differentiation. Over the years, extensive efforts have been dedicated to developing synthetic and natural biomaterials that can mimic the complex nature of the ECM. These efforts aim to create optimal environments for tissue engineering applications that closely mirror the native conditions supporting cellular activities and tissue regeneration. Hydrogels are highly valued for their exceptional properties and are highly desirable in various biological applications. Their moist and pliable surfaces facilitate intimate contact with tissues and significantly reduce irritation and friction against adjacent tissues, thereby resulting in excellent biocompatibility[5-8]. Therefore, to engineer reconstructed muscle tissue, hydrogel scaffolds with chemically modified unidirectional surface patterns could be suitable candidates, which provide topographical cues for organizing muscle cell morphogenesis to form aligned myotubes, as well as maximizing the exposure of the material to physical and chemical cues to increase cell adhesion, proliferation, and differentiation.

To construct a hydrogel with chemically modified unidirectional surface patterns, we adopted the force-induced surface modification of double-network (DN) hydrogels. Typically, DN hydrogels consist of two interpenetrating networks with contrasting properties: the first network is rigid and brittle, often composed of a highly crosslinked polymer poly(2-acrylamido-2-methylpropanesulfonic acid sodium salt) (PNaAMPS), while the second network is soft and stretchable, usually made of

polyacrylamide (PAAm)[9]. The contrasting two networks result in the high toughness of DN hydrogels[10]. Recently, we have reported on the force-triggered surface modification of DN hydrogels[11]. Mechanical forces on DN hydrogels filled with monomer solutions preferentially break the brittle first network, which produces radicals at the broken end that can initiate the polymerization of surrounding monomers and improve the mechanical properties of DN hydrogels. The concept of using DN gels to achieve self-growing materials that experience bond breakage-initiated mechanoradical reactions will be applicable to a variety of DN gels and multi-network gels provided by monomers that undergo free radical polymerization[12-14]. In this method, when the surface of a monomer-containing DN gel is pressed with a thin plate, a convex linear pattern is formed on the DN hydrogel surface due to polymerization of the monomer in the pressed region. The resulting pattern mainly comprises newly synthesized polymers. Therefore, its chemical and mechanical properties are very different from those of the surrounding DN gel and can be controlled by the composition of the monomers introduced into the DN hydrogel beforehand.

Thus, this study aimed to construct chemically modified unidirectional surface patterns on DN hydrogels as a desired scaffold for inducing myoblast differentiation. Here, *N*-isopropylacrylamide (NIPAm) was selected as a monomer of poly(*N*-isopropylacrylamide) (PNIPAm) to construct a hydrogel surface pattern, forming micromodes with unidirectional alignment, hydrophobicity, and roughness. PNIPAm is a nondegradable thermoresponsive polymer with a lower critical solution temperature (LCST) of 32°C. For example, an innovative use of PNIPAm is in cell culture, where the polymer serves as a temporary scaffold but is not embedded. L929 cells are capable of spontaneously dissociating from the hydrogel surface in the absence of trypsin or ethylenediaminetetraacetic acid (EDTA). Subsequently, the dissociated cells can be re-cultured[15]. This technique preserves the existing extracellular matrix that cells contact and deposit, which is important for survival and proliferation upon transplantation. In this study, we constructed a PNIPAm unidirectional micropattern on DN hydrogels using the abovementioned method. These micropatterned substrates are expected to provide topographic cues similar to those found in native muscle tissue, which are critical for inducing cell alignment, differentiation, and maturation without exogenous differentiation-inducing reagents or soluble factors.

3. Experimental section

3.1 Materials and reagents.

The anionic monomer 2-acrylamido-2-methylpropanesulfonic acid sodium salt (NaAMPS, 49.7wt% aqueous solution) was provided by Toagosei Co., Ltd., (Japan) and used as received. All of the materials, including monomer acrylamide (AAm), *N,N*-Dimethylacrylamide (DMA), and *N*-isopropylacrylamide (NIPAm), crosslinker *N,N′*-methylenebis(acrylamide) (MBAA), 2-oxoglutaric acid (*α*-keto), were obtained from Wako Pure Chemical Industries, Ltd., Japan and used as received. 8-anilino-1-naphthalenesulfonic acid (ANS) was purchased from Tokyo Chemical Industry and used as received. All other reagents and solvents were purchased from Sigma-Aldrich and used as received.

3.2 Hydrogels preparation.

We used the previously-developed approach to prepare single-network hydrogels and double-network hydrogels with controlled surface[13,14]. Firstly, the PNaAMPS SN hydrogel was synthesized from its precursor aqueous solution (1.0 M monomer NaAMPS, 50 mM crosslinker MBAA, and 10 mM 2-oxoglutaric acid) via free-radical copolymerization. The synthesized PNaAMPS gel was immersed in the precursor aqueous solution for the PAAm second network (monomer concentration of 2.0 M, 0.2 mM MBAA, and 0.2 mM 2-oxoglutaric acid) for one day. Then the fully swollen PNaAMPS SN hydrogel was sandwiched between two flat plates. The plates were made of glass covered with a silicone-coated polyethylene terephthalate (PET) film. The reaction cell was compressed at a pressure of 0.8 MPa for at least 12 h. Then the reaction cell was irradiated with UV light (365 nm, 4 mWcm-2) for at least 8 h in an argon glove box to synthesize the PAAm network in the presence of the first PNaAMPS network[15,16].

3.3 Creating aligned microstructures on DN hydrogel surfaces.

The blade thickness is 113 μm, the space between the blades was controlled by silicone spacers (typically 500 μm). For reference, the DN hydrogel dishes (diameter was 12 mm) were immersed in an aqueous mixed solution of monomer NIPAm (1 M) and crosslinker MBAA (30 mM) overnight to incorporate the reagents. Then, each DN hydrogel containing monomers and

crosslinkers was moved to an argon glove box to remove oxygen. The DN hydrogel dishes were fixed on a rigid glass plate with glue and then selectively indented in the solution using the home-made stacked metal blade. The indentation depth was around 1 mm. Finally, the hydrogels were immersed in deionised water for at least two weeks to remove the residual monomers prior the cell culture.

3.4 Fluorescent of PNIPAm-ANS.

The DN hydrogels were immersed in NIPAm-ANS aqueous solution (NIPAm: 1.0 M, ANS: 0.3 mM) for overnight. The immersed DN hydrogels were fixed on a rigid glass plate by glue, moved to an argon glove box at least for two hours to remove oxygen, and indented by the stacked blade as mentioned above. The DN hydrogels with grown patterns were immersed in pure water for removing residual monomers and observed at high temperature (50^{o}C) under ultraviolet light (UV) irradiation[11].

3.5 Raman Spectra.

Raman spectra were acquired with confocal Raman microscope (RAMANtouch; Nanophoton, Osaka, Japan). The excitation wavelength of the laser was 532 nm; the sample was illuminated with the laser beam through a dry objective lens (Nikon 20X TU Plan Fluor/NA 0.45) with excitation power: 41 mW, exposure time: 2 s at each point in region of interest of 16 μm×16 μm selected from PNIPAm pattern on the patterned DN hydrogel.

3.6 Spectral processing.

Raman spectra were prepossessed using custom code written in MATLAB 2020b. At first, all raw Raman spectra were corrected for cosmic rays. Singular value denoising was used to increase signal-to-noise ratio, with the 13 most significant singular values being retained during reconstruction. The fluorescence background was removed using asymmetric least square method. Raman intensities in the silent region (1729-1837 cm^{-1}) and those less than 250 cm^{-1} were truncated from all the signals. Finally, spectra were normalized by dividing by the sum of intensities over the

remaining wavenumbers (250-1728 cm^{-1}, 2837-3030 cm^{-1}) and average spectra from each ROI is shown in the Figures.

3.7 Surface observation of different hydrogel surfaces by a three-dimensional (3D) laser microscope.

Different patterned DN hydrogel surfaces were observed in air by a 3D laser microscope (VK-9710, Keyence Co., Ltd.). Free water on hydrogel surfaces was wiped out by clean tissues prior to observation. The magnification was 10, and the resolution was 0.5 μm for each observation. Surface roughness value Ra was calculated by selecting a small square area (500 μm × 500 μm) on hydrogel surfaces. Different hydrogel surfaces, microstructures, patterns, and the reswollen zones were also observed by the microscope, profile and size of microstructures were measured by a software VK Analyzer.

3.8 Contact angle measurements of the PNIPAm hydrogel surfaces.

The static water contact angle of the PNIPAm hydrogel was measured by using a Dropmaster 300 (Kyowa Interface Science Co., Ltd.) in air at 25°C and 50°C. The PNIPAm hydrogel surface was washed with deionized water three times prior to the measurements. Free water on hydrogel surfaces was wiped off using cleaning tissues prior to each measurement. The water volume of 10 μL and the waiting time of 5 s were used for each measurement, respectively. The contact angle was the average value of three measurements.

3.9 Cell counting.

The cells resuspended in PBS were mixed with 0.4% trypan blue staining solution at a ratio of 1:1, and inserted into a cell counting chamber slide (Invitrogen). The cell numbers were counted using Countess II FL (Invitrogen), and the independent experiments were repeated for three times.

3.10 Muscle cell culture and live imaging.

Mouse myoblast cell line C2C12, labelled with green fluorescent protein (GFP), was kindly provided by Dr. S. Kohsaka. The cells were cultured in the growth medium (GM), which was Dulbecco's modified Eagle's medium (DMEM, Invitrogen, Carlsbad, CA) supplemented with 10% fetal bovine serum (FBS, Invitrogen) and 1% penicillin-streptomycin (Invitrogen). The cells were cultured in a culture dish in a humidified incubator (37oC, 5% CO2). Prior to cell seeding, all hydrogels were sterilized, placed in 24-well culture plates, and incubated in DMEM at 37oC overnight. Phase contrast and epifluorescence imaging were performed using a Delta Vision system (Applied Precision Inc.) on an Olympus IX83 inverted microscope equipped with a cooled CCD camera.

3.11 Immunocytochemistry.

The muscle cells cultured in the DMEM for 7 days were washed with pre-warmed PBS and fixed with 3% paraformaldehyde (PFA) solution for 15 minutes, treated with 0.1% v/v Triton X-100 for 4 minutes to make the cell membrane permeable, and incubated in the blocking solution (1% BSA in PBS) for 20 min. The samples were incubated overnight at 4° C with a mouse monoclonal antibody (anti-Myod (sc-377460), Santa Cruz) at a 1:400 dilution in PBT (PBS containing 0.1% BSA and 0.05% Triton X-100), followed by the incubation with a 1:250 dilution of Alexa 594-conjugated anti-Rabbit IgG (Invitrogen) in PBT for 1 hour. The nuclei were stained with DAPI (1 μg/ml) for 20 minutes in PBT. The fluorescence images were obtained with the Olympus IX83 inverted microscope, and analyzed using the ImageJ software (National Institutes of Health, Bethesda, MD). The cellular orientations of C2C12 myoblasts or myotubes were quantitatively analyzed to determine the angle between the pattern direction and the longest axis of the cells. The aspect ratio of myoblasts, defined as the ratio between the body length of the longest axis and that of the shortest axis across the nuclei, was also analyzed.

3.12 Time-lapse imaging.

A set of two-dimensional (2D) time-series images from muscle cells obtained using wide-field microscopy. Detection and tracking of cell clusters in time-lapse microscopy images were carried out in a humidified incubator (37^{o}C, 5% CO_2) for two days. Buffer solutions containing pH stabilizer were used.

3.13 Quantitative real time PCR (qRT-PCR).

Total RNA was extracted from the C2C12 myoblasts using a RNeasy Mini Kit (Qiagen, Valencia, CA) according to the manufacturer's protocols and reverse transcribed into cDNA using the SuperScript® VILO™ cDNA Synthesis Kit (Invitrogen, Carlsbad, CA). Relative expression levels of RNA were normalized to *glyceraldehyde-3-phosphate dehydrogenase* (*GAPDH*). qRT-PCR samples were prepared with the same amount of cDNA, Power SYBR green PCR master mix, and the following primers: *GAPDH* (forward: 5′-AGC CAC ATC GCT CAG ACA C-3′, reverse: 5′-GCC CAA TAC GAC CAA ATC C-3′); *MyoD* (forward: 5′-GCC TGA GCA AAG TGA ATG AG-3′, reverse: 5′-GCA GAC CTT CGA TGT AGC G-3′); *MHC* (forward: 5′-AGC AGA CGG AGA GGA GCA GGA AG-3′, reverse: 5′-CTT CAG CTC CTC CGC CAT CAT G-3′); *Myf5* (forward: 5′-CCT GTC TGG TCC CGA AAG AAC-3′, reverse: 5′-GAC GTG ATT CGA TCC ACA AT G-3′). qRT-PCR was performed using StepOnePlus™ Real-Time PCR System (Applied Biosystems, Waltham, MA) using Power SYBR® Green Master Mix (Invitrogen).

3.14 Statistical analysis.

Statistical analyses of the mechanical testing, cell proliferation and gene expression were performed using one-way analysis of variance (ANOVA). P values less than 0.05 were considered statistically significant, and differences between samples within the groups were evaluated using a Student's t-test ($P < 0.05$).

4. Results

4.1 Synthesis and characterization of microstructures based on DN hydrogels.

Our mechanochemical strategy for force-triggered microstructure growth is shown in **Figure 1**. DN hydrogels comprises two interpenetrating networks with distinct structural and mechanical properties. The first network with PNaAMPS, which is highly cross-linked and prestretched, acts as a rigid but fragile backbone at the molecular scale. The second network with PAAm, which is sparsely cross-linked and relatively concentrated, is soft and stretchable[18-20]. Owing to this contrasting structure, many of the first network chains break during deformation without causing catastrophic failure of the hydrogel because once a chain in the first network breaks, the second network takes on the load[21]. The scission of chains in the first brittle network usually occurs due to the homolytic scission of covalent bonds, which generates mechanoradicals at the ends of polymer chain scissions[22]. The concentration of mechanoradicals is high enough to initiate polymerization within monomer-fed DN hydrogels, enabling force-triggered DN hydrogel growth in the presence of active monomers as building elements, similar to nutrients in the natural growth of living things.

The polymer chain rupture in the DN hydrogel immersed in the monomer solution, which is caused by the force applied by a metal blade to the DN hydrogel, rapidly induces radical polymerization of the monomers to form a surface pattern **(Figure 2**). When NIPAm was used as the monomer, the reconstructed surface pattern made from poly(*N*-isopropylacrylamide) (PNIPAm) was 50 μm high and 90 μm wide, with a spacing of 500 μm between the two patterns (**Figure 2, Figure 3A, 3B**). To confirm the formation of PNIPAm, the fluorescent molecular probe 8-aniline-1-naphthalenesulfonic acid (ANS) was used for fluorescent staining of hydrophobic PNIPAm at high temperature,[23,24] and parallel fluorescence patterns were observed (**Figure 4**). To distinguish between the chemical characteristics of PNIPAm and untreated DN hydrogels, Raman spectroscopy was employed to characterize the chemical signal of PNIPAm. The peaks of 1616, 1657, and 1667 cm^{-1}, associated with Amide 1 and Amide 2, were more intense in the PNIPAm pattern[25] than in the DN pattern (**Figure 5**). We also generated poly(*N,N*-dimethylacrylamide) (PDMA), poly(2-acrylamido-2-methylpropanesulfonic acid sodium salt) (PNaAMPS), and poly(acrylamide) (PAAm) patterns on the DN hydrogels by changing the composition of the monomer solution. In addition, we also prepared a reswollen pattern, which was similarly made by

mechanical indentation to the DN hydrogel immersed in pure water without any monomers inside, as a control.

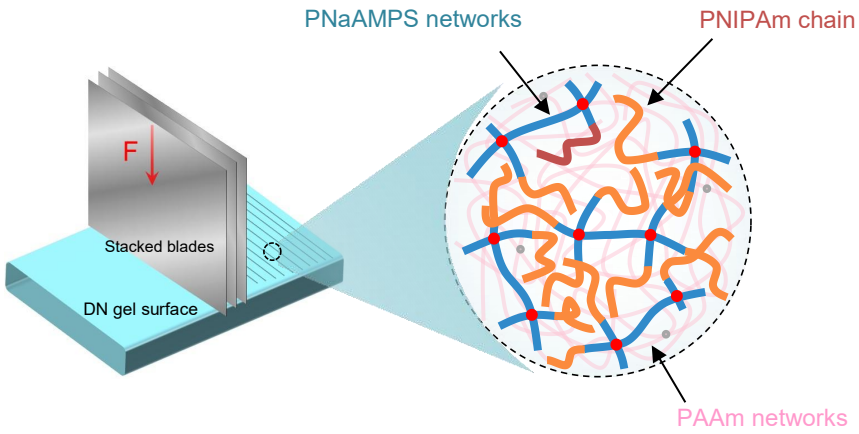

Figure 1. Mechanochemical strategy for inducing microstructure growth under mechanical force.

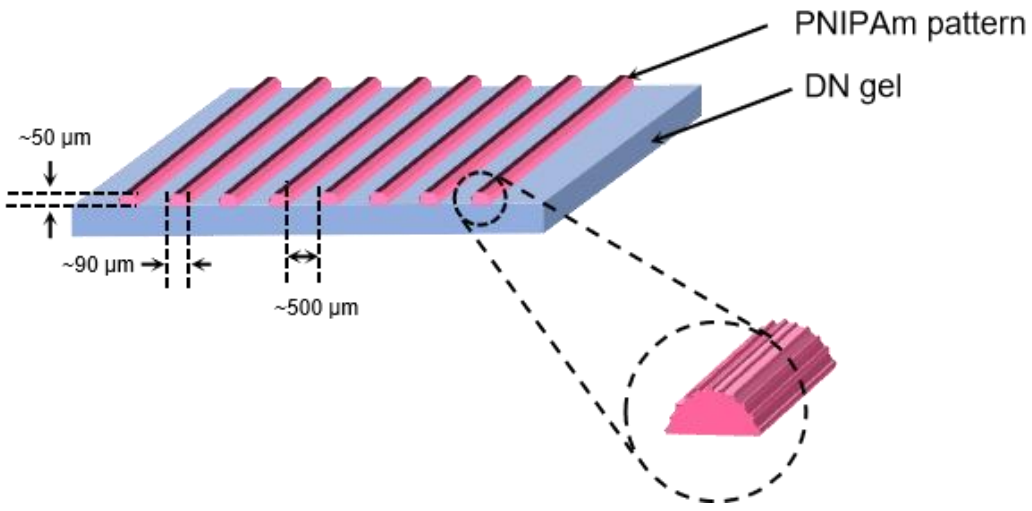

Figure 2. An illustration delineating the microstructural composition of the micropatterns.

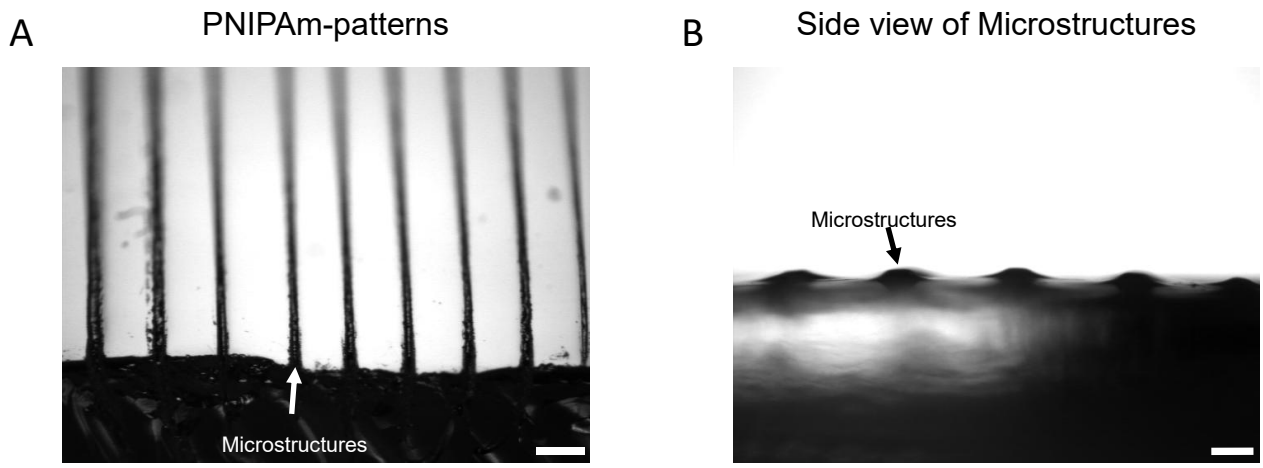

Figure 3. (A) Optical photographs of micropatterns. Scale bars: 500 μm. (B) Optical photographs of Microstructures (Side view). Scale bars: 90 μm.

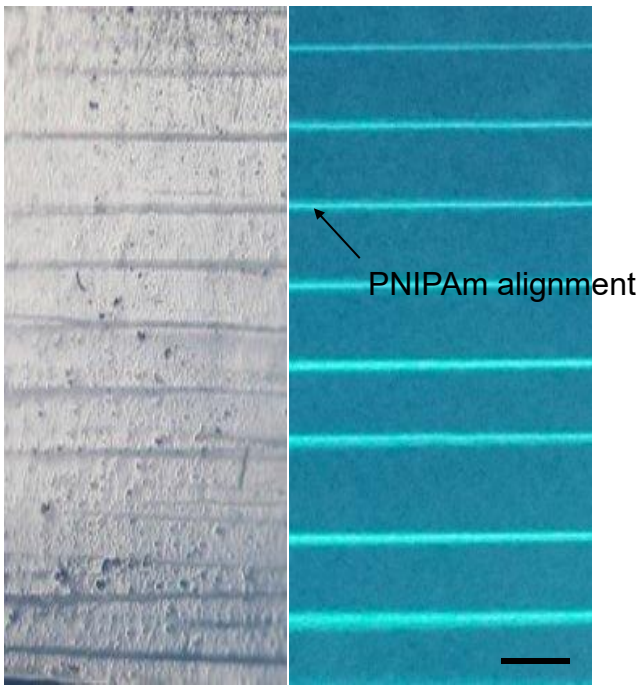

Figure 4. Fluorescence photographs showing the aligned structure formed by force triggered growth of PNIPAm on the DN hydrogel. Scale bar: 5 mm.

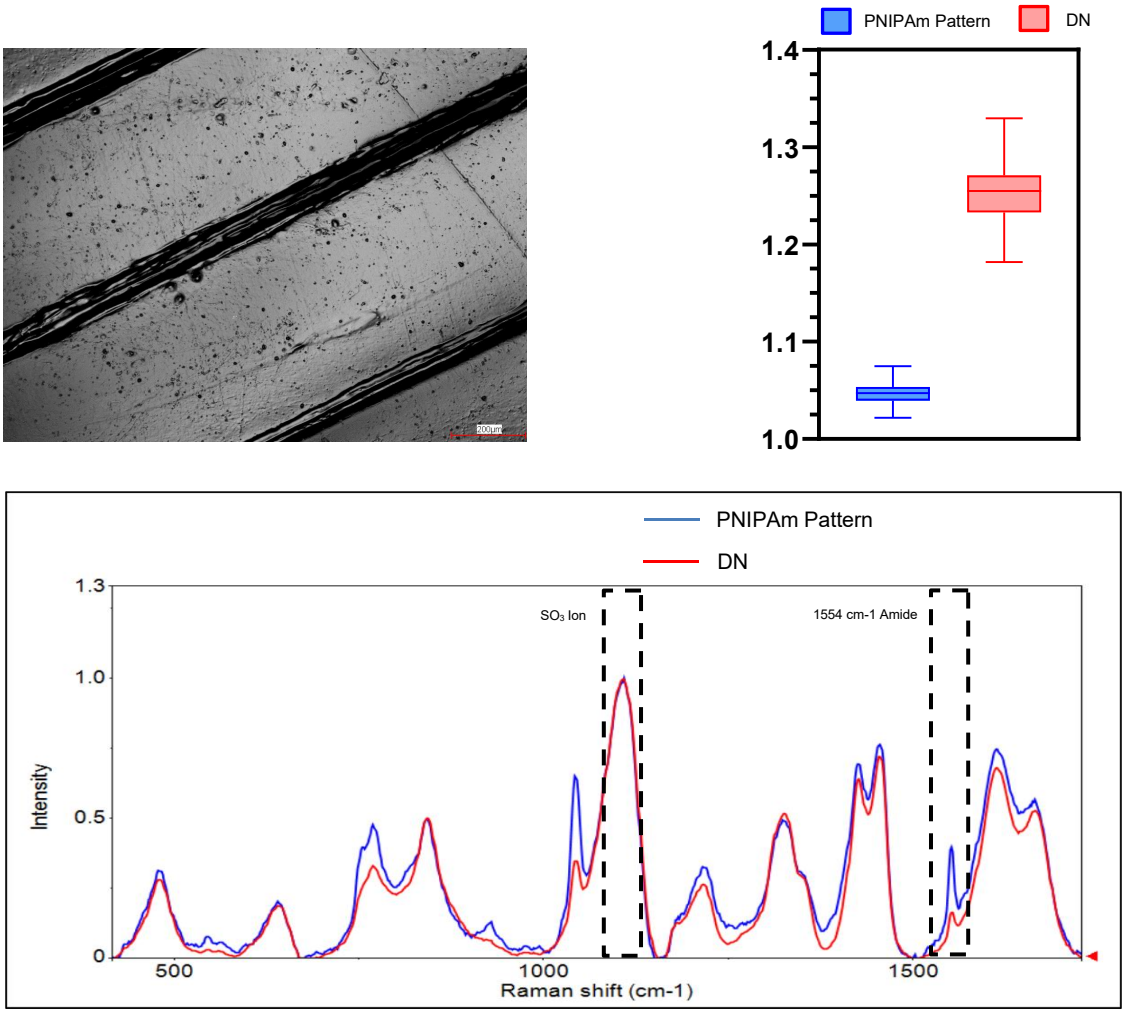

Figure 5. Optical photograph of micropatterns (upper left). Raman spectra (lower) and ratio maps at 1105 and 1554 cm−1 (upper right) for the chemical double network (DN) and PNIPAm-patterned domain. Scale bars: 200 μm.

4.2 Morphological response of C2C12 myoblasts to micropatterns.

Cells fine-tune morphology and cellular function through continuous cell–cell interactions and movement. Cell morphology can be evaluated as an indicator of various cell functions and dysfunctions. To adequately describe the morphology of the cells on the hydrogel surface, fractal analysis of the cells is very important for characterizing the cell status. Here, C2C12 myoblasts labeled with green fluorescent protein (GFP) were cultured in growth medium and photographed under a fluorescence microscope. The ability of myoblasts to selectively adhere to different polymer patterns with controlled alignment properties was assessed (**Figure 6**). After 7 days of culture, the C2C12 cells attached to the PNIPAm, PDMA, and PNaAMPS patterns and grow in bundles, but no parallel cell bundles were observed in the PAAm patterns, and the reswollen patterns were used as a control group (**Figure 6**). In contrast, no cell extension or bunching was observed on the 250–300-μm wide PNIPAm pattern (**Figure 7**). In addition, in the hydrogels with PDMA–PNIPAM and PDMA–PAAM cross patterns, only cell bundles between the PDMA and PNIPAm patterns were observed (**Figure 8A, 8B**), indicating that the cells exhibited different adhesion abilities and morphologies based on different properties of the substrate, such as surface charge, hydrophobicity, roughness, and chemical residues.

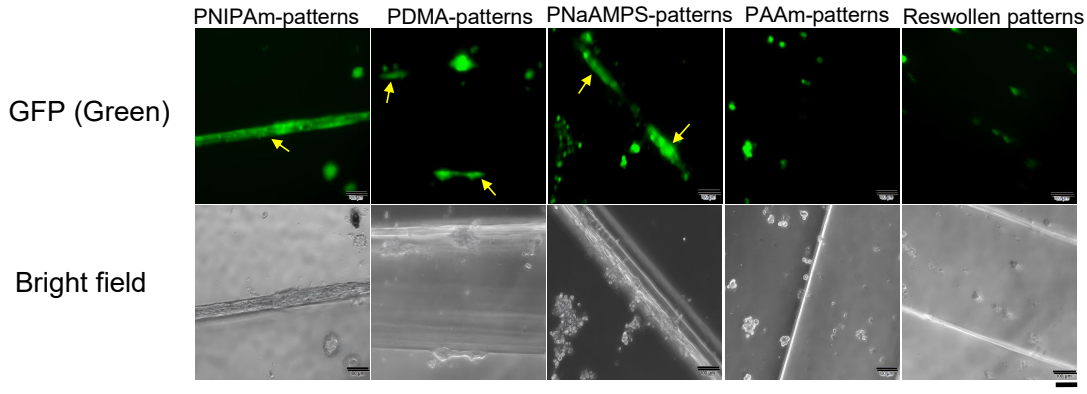

Figure 6. Cellular morphology of C2C12-GFP cells cultured for seven days on micropatterns, such as the PNIPAm-pattern, PDMA-pattern, PNaAMPS-pattern, PAAm-pattern, and reswollen pattern. Scale bars: 100 μm.

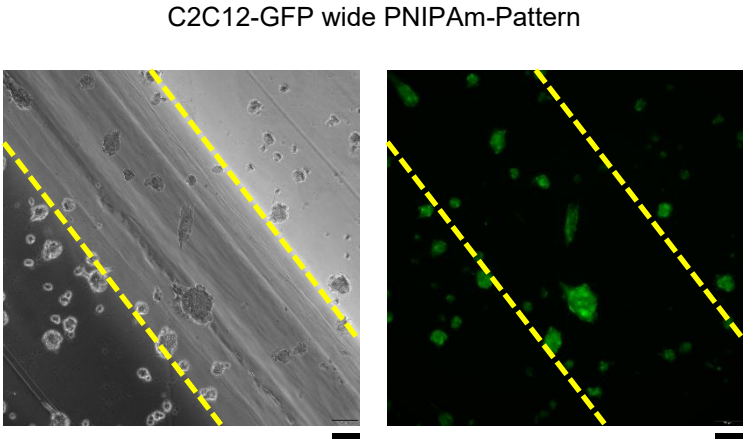

Figure 7. Cellular morphology of C2C12-GFP cells cultured on a broad PNIPAm pattern. Scale bar: 50 µm.

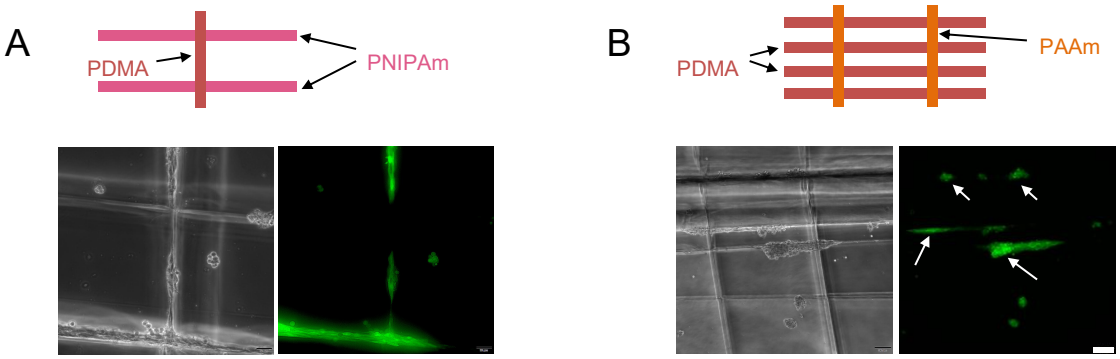

Figure 8. (A and B) Cellular morphology of C2C12-GFP cells cultured on PNIPAm-PDMA and PDMA-PAAm dual-pattern hydrogels for 7 days. The arrow denotes the area of cell attachment and survival. Scale bars: **(A)** 100 and **(B)** 50 µm.

4.3 Adhesion mechanism of C2C12 cells on the PNIPAm micropattern.

Contact between cells and implanted biomaterials results in biospecific and nonbiospecific interactions. The former mainly interacts with the receptors, whereas the latter involves electrostatic interactions, hydrogen bonding, hydrophilic and hydrophobic binding[26]. To investigate the nonbiospecific interactions of PNIPAm and the original PNaAMPS/PAAm DN, the ability of PNIPAm and DN hydrogels to support myoblast proliferation was evaluated (**Figure 9**). After 3 days of culture, there was no significant difference in the number of cells between the PNIPAm and DN hydrogels, indicating equal attachment to the PNIPAm and DN hydrogels. After one week of culture, the number of myoblasts on the PNIPAm was nearly 9 times greater than that on the DN hydrogel (**Figure 9**), suggesting that the biocompatibility of PNIPAm exceeds that of the DN hydrogel. The myoblasts could attach to the DN hydrogel, but cell proliferation was inhibited (**Figure 9**). It is well known that aqueous PNIPAm can switch between hydrophilicity and hydrophobicity at temperatures below or above the LCST of PNIPAm hydrogels[27]. The surface of a hydrogel is typically covered by water hydrated on a hydrophilic polymer network. Once a PNIPAM hydrogel becomes hydrophobic with increasing temperature, the chemical potential of the water molecules on the gel surface also increases due to dehydration. Such water molecules move from the surface into the bulk, resulting in a reduction in the total free energy and exposure of the hydrophobic PNIPAM on the gel surface. This outcome provides a strong thermodynamic driving force for the adsorption of proteins onto hydrophobic surfaces, resulting in a stronger ability to adsorb to cell membranes than on hydrophilic surfaces. We measured the water contact angle of the PNIPAm hydrogel at 25°C and 50°C, and the contact angle at 50°C was greater than that at 25°C, reflecting its hydrophobicity (**Figure 10**). The attachment of cells on the PNIPAm patterns at 37°C and 20°C was examined to confirm the effect of the hydrophobicity of PNIPAm on cell adhesion, and many cells detached at 20°C (**Figure 11**, arrow); hence, the hydrophobicity of PNIPAm is important for cell adhesion. In the short-bundled cell groups, all cells will detach (**Figure 12**), while only some cells will detach spontaneously in the long-bundled cell groups (**Figure 11**). This detachment was more pronounced under the 5°C condition (**Figure 13**). To examine the viability of the cells that spontaneously detached from the PNIPAm pattern at 20°C, the detached cells were reseeded on regular polystyrene (PS) dishes. The cell viability reached 87% even at 20°C, and the cells could proliferate normally on PS dishes (**Figure 14, 15**). In contrast, the physical properties of the substrate, such as surface roughness, also

significantly affect the cell–substrate interactions. Rough surfaces provide more anchor points for cell attachment than smooth surfaces, enhancing cell attachment. Here, we quantified the surface roughness of PNIPAm micropatterns and the DN substrate using three-dimensional (3D) laser microscopy. The results revealed that the surface roughness of the PNIPAm patterns was much greater than that of the DN substrate (**Figure 16**). The surface roughness of the PNIPAm pattern was the highest among all the polymer patterns (**Figure 17, 18**). Therefore, the cells adhered topologically to more anchor points on the PNIPAm pattern.

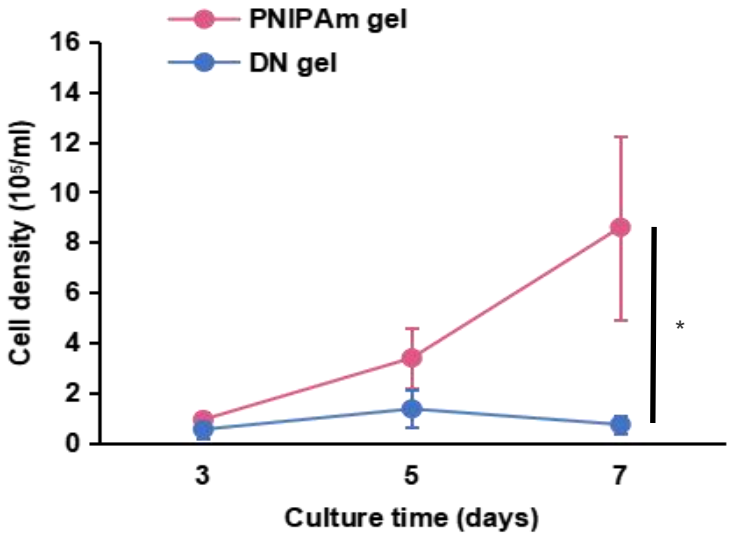

Figure 9. Proliferation of C2C12 cells cultured on double-network (DN) hydrogels and PNIPAm hydrogels.

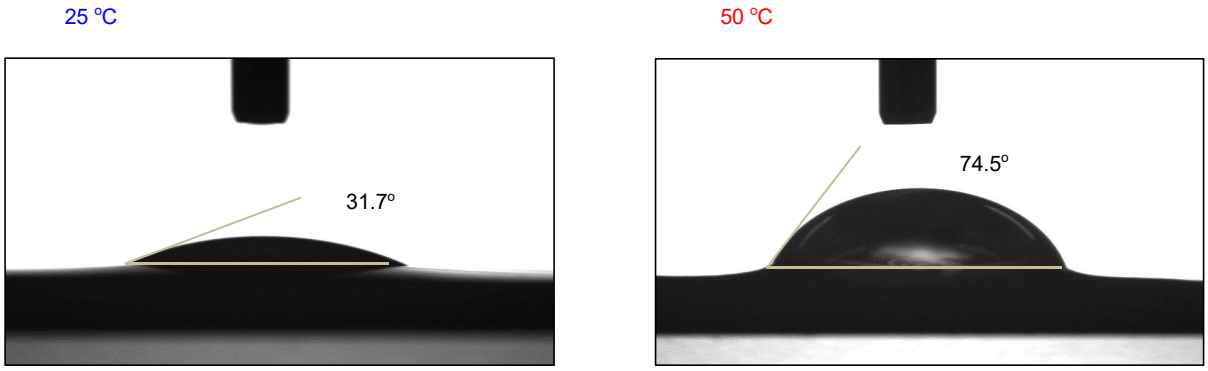

Figure 10. Contact angle of water on the PNIPAm hydrogel at 25°C and 50°C.

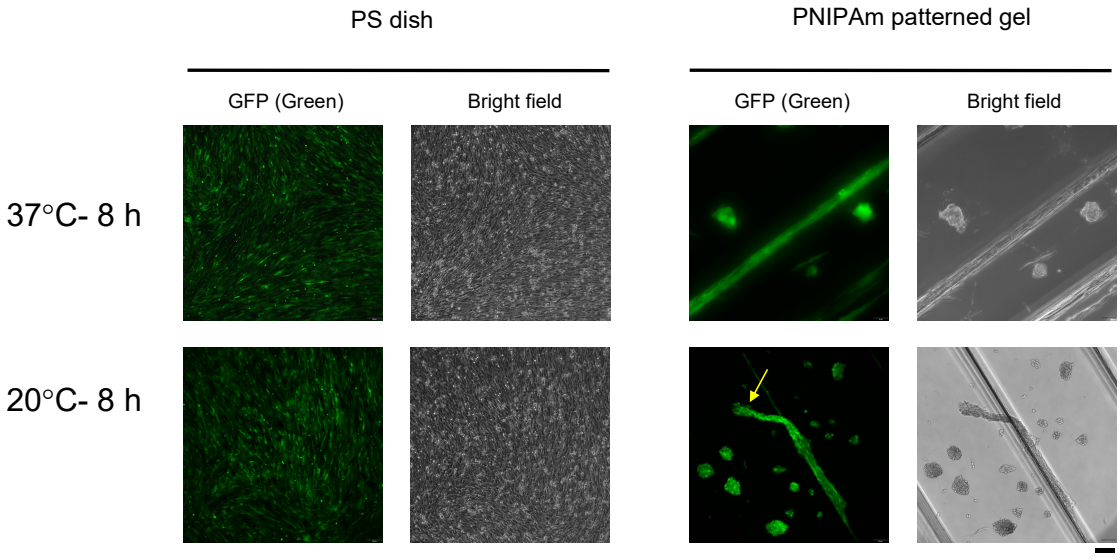

Figure 11. Cellular morphology of C2C12-GFP cells cultured on PS dishes and the PNIPAm-patterned gel at 37°C and 20°C for 8 h. The arrow indicates cell desorption bunking. Scale bars: (**C**) 50 μm.

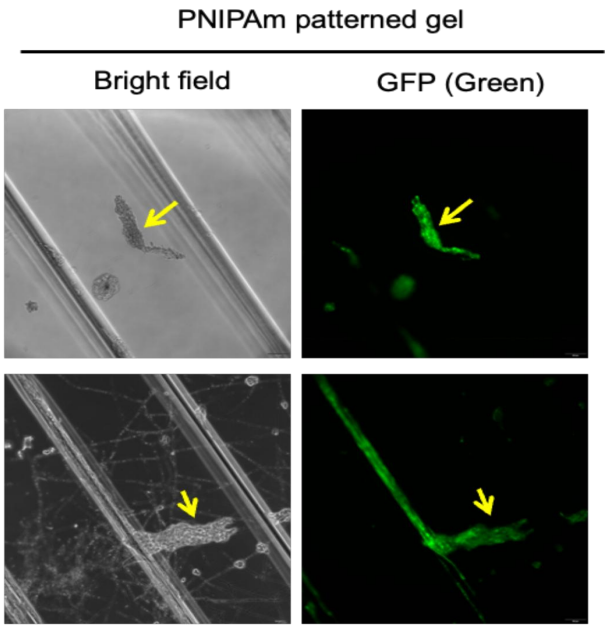

Figure 12. Cellular morphology of C2C12-GFP cells cultured on PS dishes and the PNIPAm-patterned gel at 20°C for 8 h. The arrow indicates cell desorption bunking.

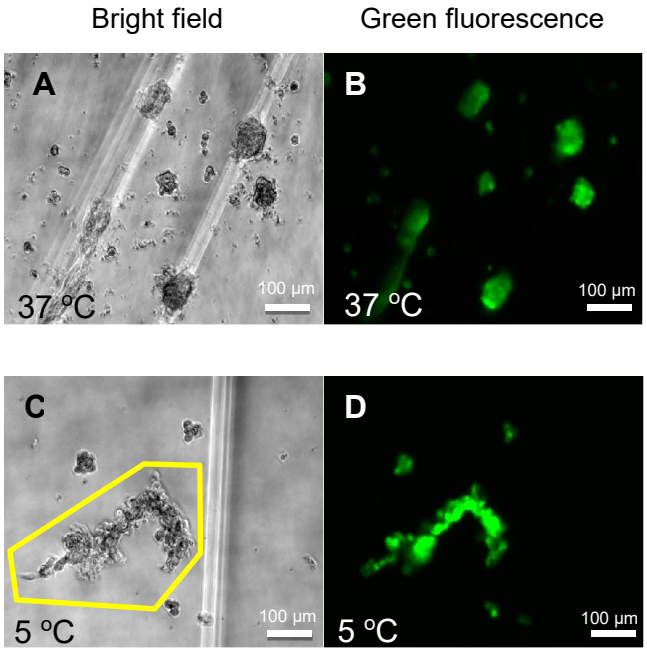

Figure 13. (A, B) Thermo-responsive adhesion and detachment of C2C12 cells on the PNIPAm patterned DN hydrogels. a,b. At 37°C, most cells significantly adhered to the PNIPAm pattern. **(C, D)** At 5°C, the cell clusters detached from the PNIPAm pattern automatically. Cells were incubated at 5°C for 10 hours prior to the microscopic observation. The yellow box in **Figure c** represents the detached cell clusters.

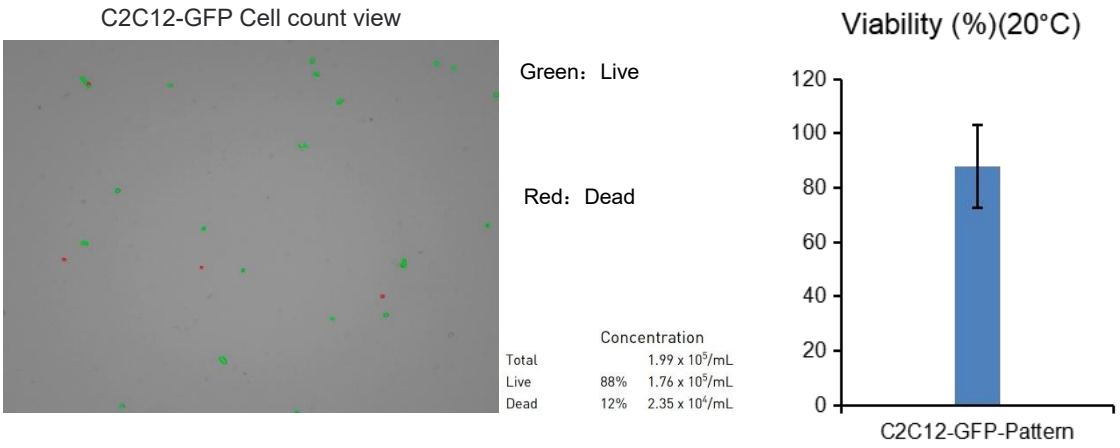

Figure 14. Viability of C2C12-GFP cells after low-temperature detachment from the PNIPAm-patterned hydrogel. (left) Green and red spots indicate living and dead cells, respectively, and cell viability is shown as the mean ± SD from three different areas in the graph.

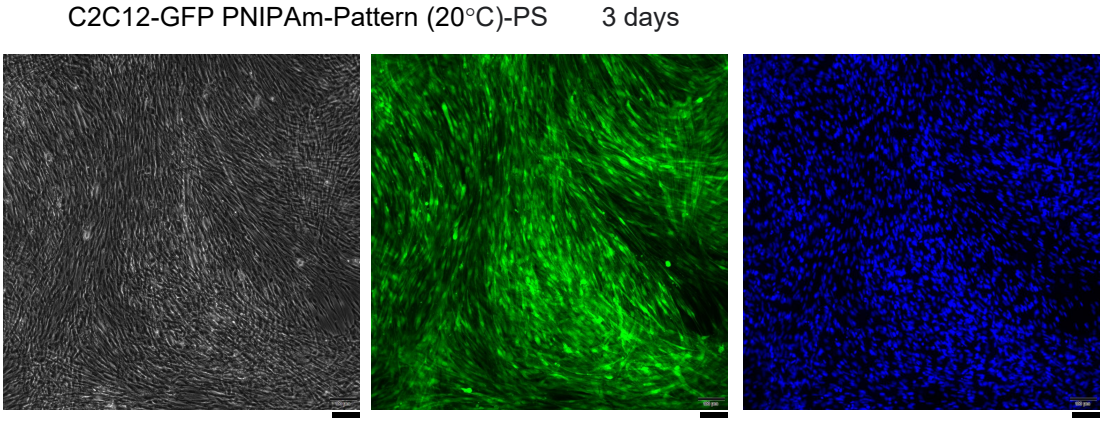

Figure 15. Cellular morphology of C2C12-GFP cells transferred to PS dishes after low-temperature detachment from the PNIPAm-patterned hydrogel. Left: phase contrast image; middle: GFP showing C2C12 cells; right: DAPI staining the nucleus. Scale bar: 50 μm.

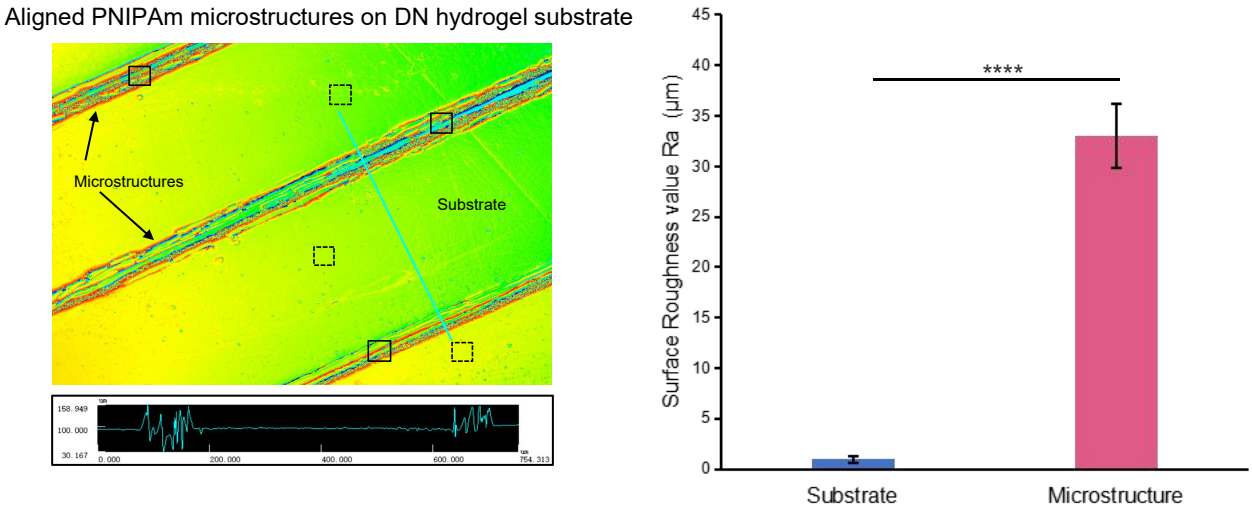

Figure 16. Surface roughness characteristics of the DN hydrogel and PNIPAm microstructures. Significant differences in surface roughness values were observed (****P < 0.001). The squares on the image (left) indicate the measurement area on the DN gel and PNIPAm microstructures (each n = 3), and the means ± SDs of the values are shown in the graph.

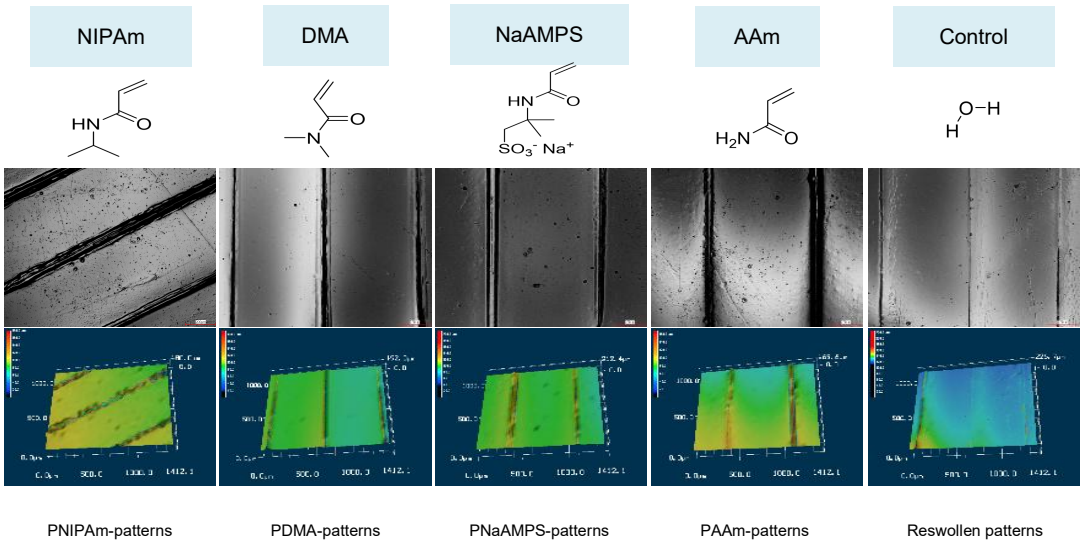

Figure 17. Three-dimensional laser scanning microscope images of microstructures reconstructed from various monomer solutions. PNIPAm-pattern, PDMA-pattern, PNaAMPS pattern, PAAm-pattern, and the reswollen pattern were used as controls. Scale bar: 200 μm.

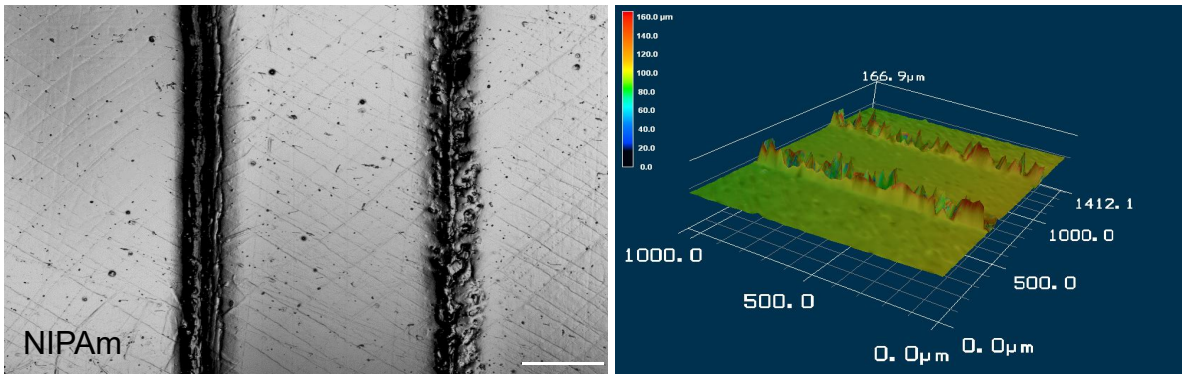

Figure 18. Topographical and morphological images of PNIPAm patterns. The magnified views reveal the rough surface and stripe-like details of the PNIPAm pattern on DN hydrogel surfaces (Temperature is 25°C).

4.4 PNIPAm patterns induced differentiation of C2C12 cells.

We further investigated the effects of the PNIPAm patterns on myoblast differentiation. The expression of the differentiation-related marker Myoblast Determination Protein 1 (MyoD) was examined by immunofluorescence in the C2C12 cells cultured on PS dishes (control), DN hydrogel, and PNIPAm-patterned DN hydrogel for 7 days (**Figure 19**). MyoD binds to the gene regulatory region of skeletal muscle and is an early determinant of differentiation and myotube formation28. After 7 days of culture, the intracellular MyoD in the control group was essentially located in the nucleus. In contrast, in the PNIPAm and DN hydrogels, it diffused from the nucleus to the cytoplasm (**Figure 19**). We compared the MyoD fluorescence intensity between the PNIPAm pattern and the DN gel in the same region under the same conditions. The expression levels of MyoD on the PNIPAm-patterned DN gel significantly exceeded those on the DN gel substrate (**Figure 20**).

The relative expression of differentiation-related genes, such as myosin heavy chain (MHC), a representative marker of myotube cells; myogenic Factor 5 (Myf5), a key regulator during muscle differentiation or differentiation; Mrf4, a member of the myogenic regulatory factor (MRF) family that regulates differentiation and regeneration in skeletal muscle[28], increased in a time-dependent manner (**Figure 21**). Compared with the PS dish and DN gel, the PNIPAm-patterned DN gel significantly increased the expression levels of MHC and Myf5, and Mrf4 (**Figure 21**).

Oriented architectures establish a biomimetic platform for cellular proliferation while guiding morphological adaptation through contact guidance mechanisms. This topographical regulation proves critical for achieving spatially controlled cellular development, particularly in myocyte alignment processes essential for functional tissue formation. The aspect ratio was considered the ratio of the maximum length to the maximum width, and the aspect ratio of cells on the PNIPAm patterns of the DN gels at 7 days significantly exceeded those of the PS dishes and nonpatterned DN hydrogels (**Figure 22**). Myocyte alignment orientation was determined through angular deviation calculations between cellular longitudinal axes and a predefined substrate reference line, using quantitative analysis of immunofluorescence microscopy datasets.(**Figure 23**). A minimum directional angle of 0° indicates that the cells are aligned parallel to the axis, whereas a maximum of ±90° indicates vertical alignment. The percentage of cells in the directional range of −18° to 18° was approximately 100% on the aligned PNIPAm-patterned matrix compared with those on the flat matrix (PS dish and DN gel) (**Figure 23**), indicating that cells cultured on the PNIPAm-aligned

pattern were preferentially oriented along the pattern. Time-lapse microscopic analysis demonstrated that cell clusters attached to the PNIPAm patterns and migrated in an aligned manner along the patterns (**Figure 24**). On day 7, cells cultured on the PNIPAm-patterned matrices began to show significant differences in myotube formation, cell alignment, and elongation, which were not evident on the flat matrices. The myoblasts grown on the PNIPAm alignment substrate were highly organized and aligned homotropically, whereas the cells grown on the flat substrate were randomly organized with no obvious preferred direction (**Figure 23**).

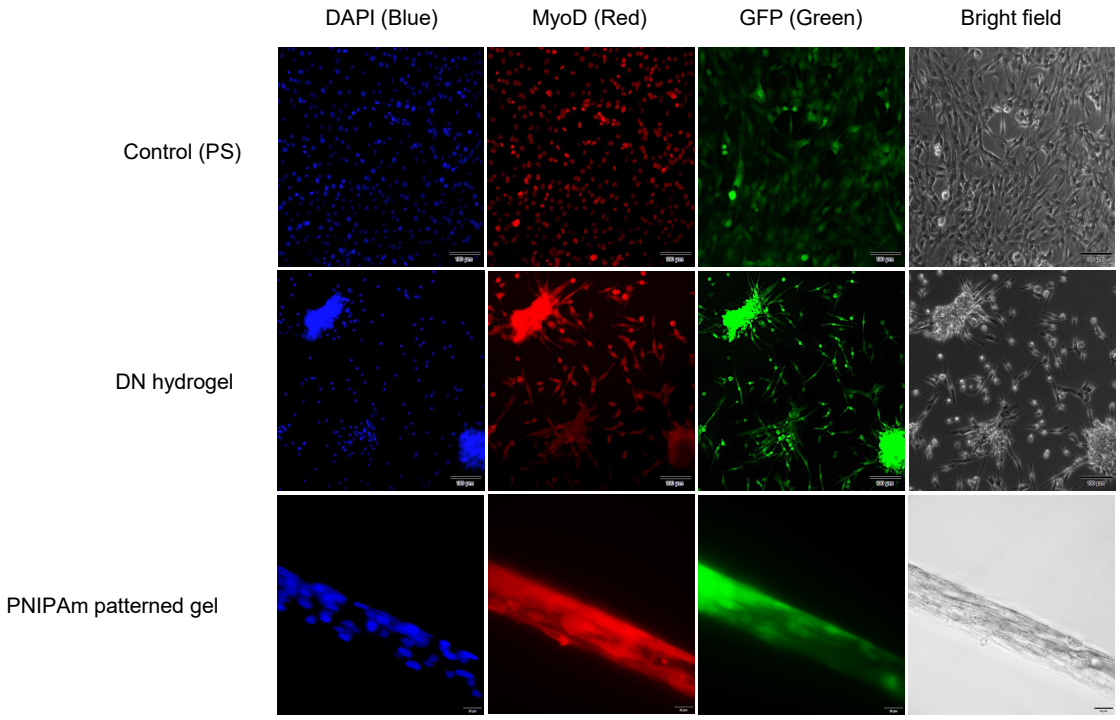

Figure 19. Representative images of C2C12-GFP cells cultured on PS dishes, DN hydrogels, and PNIPAm-patterned gels. The blue and red colors indicate DAPI-stained nuclei and MyoD-stained nuclei, respectively. The green color indicates GFP. Scale bars: (PS; DN hydrogel) 100 μm and (PNIPAm patterned gel) 20 μm.

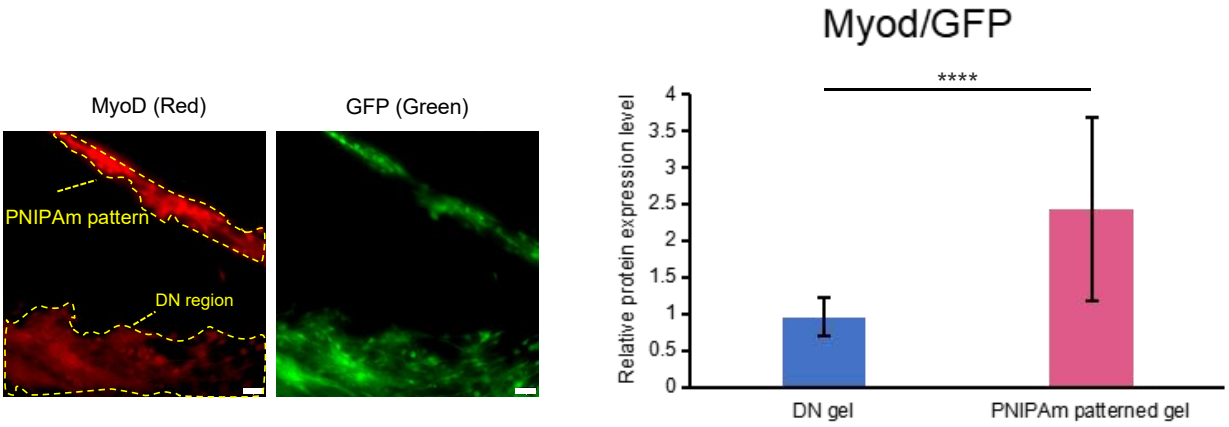

Figure 20. Immunofluorescence analysis of MyoD expression in C2C12-GFP cells cultured on PNIPAm-patterned DN hydrogels for seven days. A representative area is shown (left), and the fluorescence ratios of MyoD/GFP in the DN region and the PNIPAm-patterned region are shown (right). Scale bars: 50 μm.

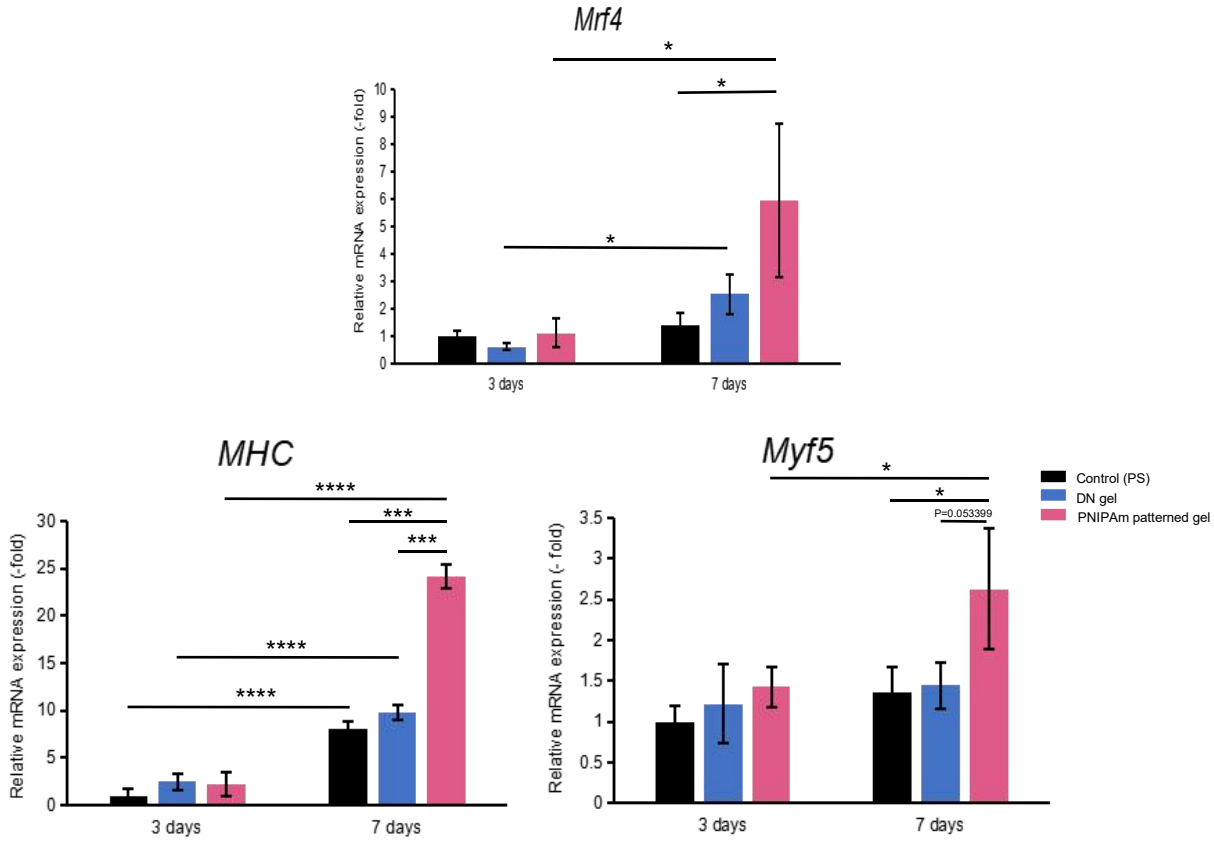

Figure 21. C2C12-GFP cells were cultured on PS dishes, DN hydrogels, or PNIPAm-patterned gels for three and seven days. The expression levels of MHC and Myf5 were examined by qRT–PCR. The PS dish was used as the negative control. Significant differences are shown in the graphs (****P < 0.001, ***P < 0.01, and *P < 0.05). The expression levels of genes are shown as the means ± SDs (n = 3).

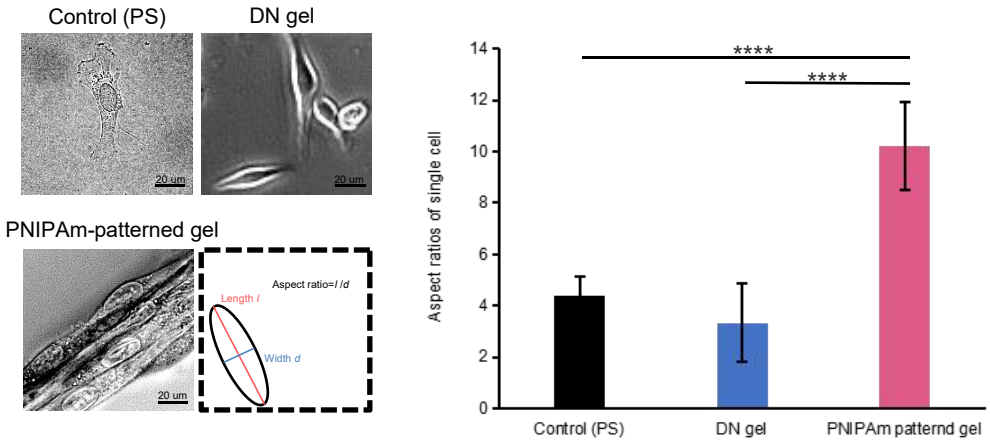

Figure 22. Cell morphological analysis of PS dishes, DN hydrogels, and PNIPAm-patterned gels. The aspect ratio was defined as the ratio of the major and minor axes of the cell. Scale bar: 20 μm. (****P < 0.001)

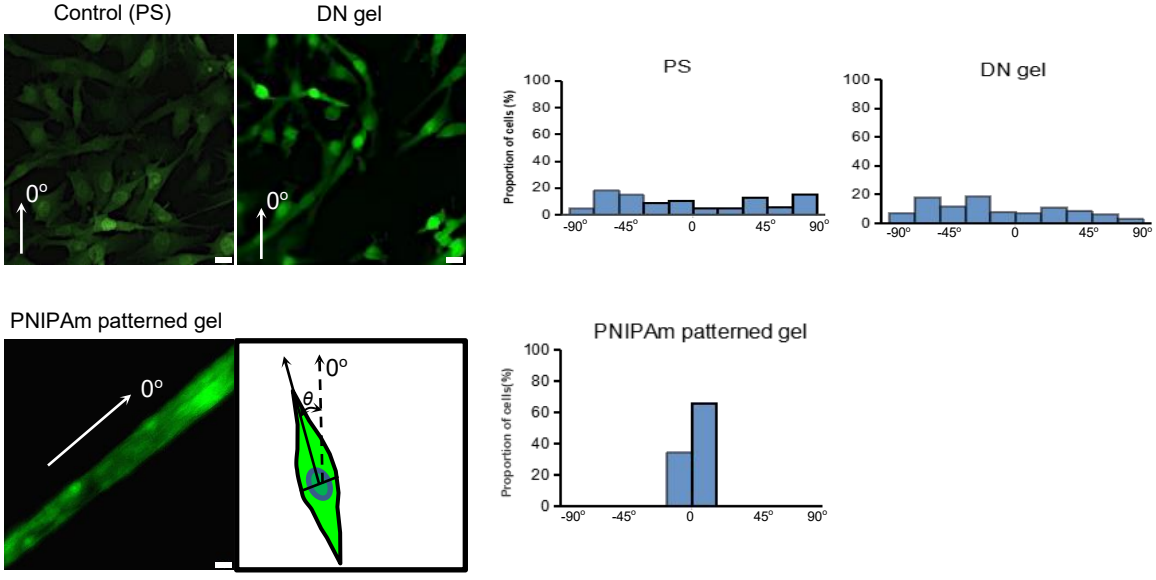

Figure 23. Histograms illustrating the distribution of angles of orientation for C2C12-GFP cells cultured on PS dishes, DN hydrogels, and PNIPAm-patterned gels. Scale bar: 20 μm.

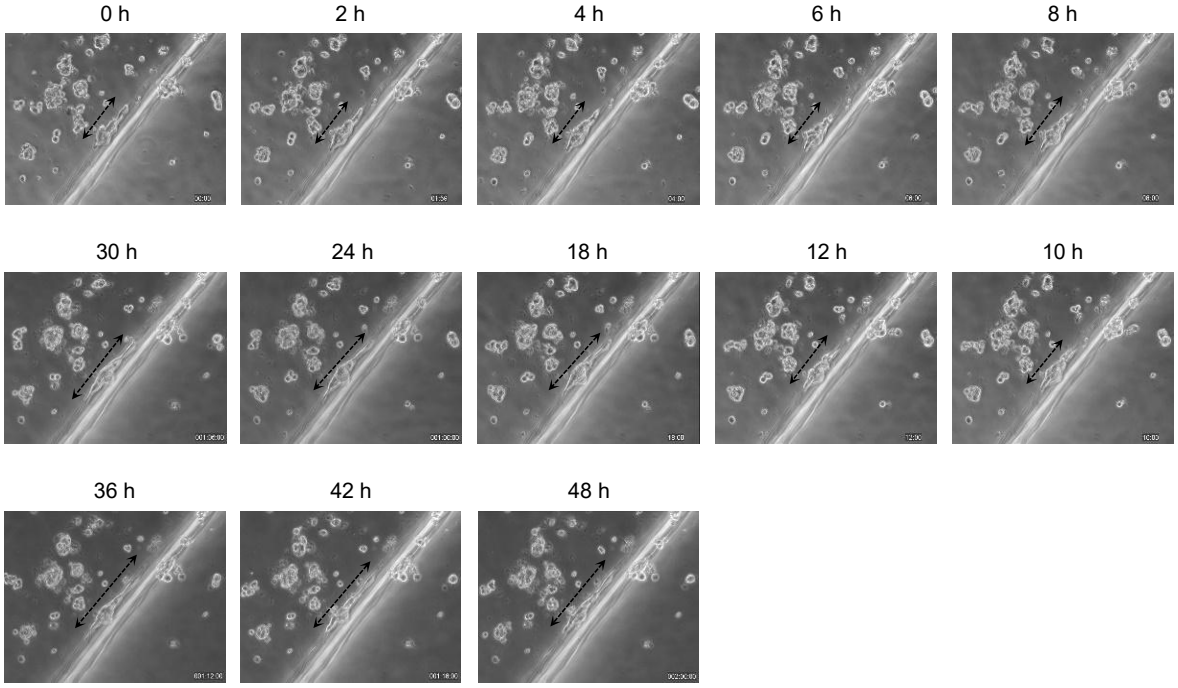

Figure 24. Time-lapse images of C2C12-GFP cells cultured on PNIPAm patterns. The cells were cultured in standard DMEM for 48 h.

4.5 Effect of substrate stiffness on myoblast differentiation.

Biomechanical analyses consistently identify substrate stiffness as a critical modulator of tissue-specific cellular responses, exerting regulatory control over both physiological processes in *vivo* and engineered constructs in *vitro*. The mechanical properties of substrates affect the adhesion, diffusion, proliferation, and differentiation of muscle cells[29,30]. Here, the stiffness of the PNIPAm pattern of the DN hydrogel was adjusted by changing the concentration of the crosslinker in the NIPAm aqueous solution (0, 2, 10, and 20 mol%). After 7 days of culture, fluorescence images revealed that the stiffness of the patterns had no effect on cell adhesion, and the cells could proliferate on the PNIPAM patterns regardless of stiffness (**Figure 25**). In contrast, the expression level of *MHC* was highest in the PNIPAm pattern with a 0 mol% crosslinker concentration and decreased as the gel stiffness increased (**Figure 26**). The expression level of *MHC* on the pure PNIPAm polymer was even lower than that on the control PS dish (**Figure 26**).

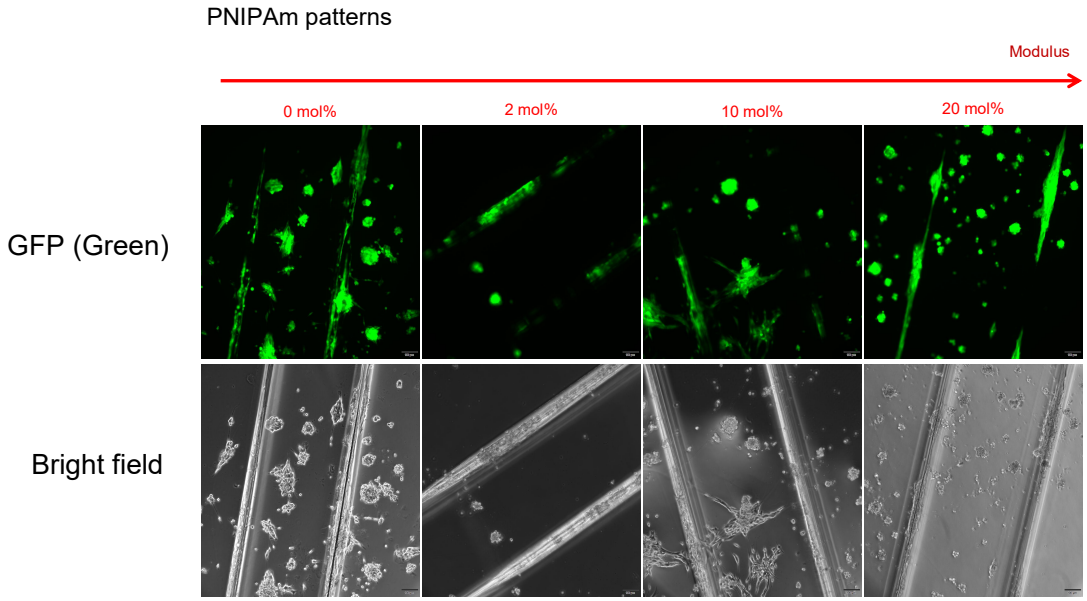

Figure 25. Morphology of C2C12-GFP cells cultured on reconstructed PNIPAm patterns immersed in different concentrations of PNIPAm solution (due to the opaqueness of the PNIPAm hydrogel, capturing the cellular morphology is not feasible). Scale bars:50 μm.

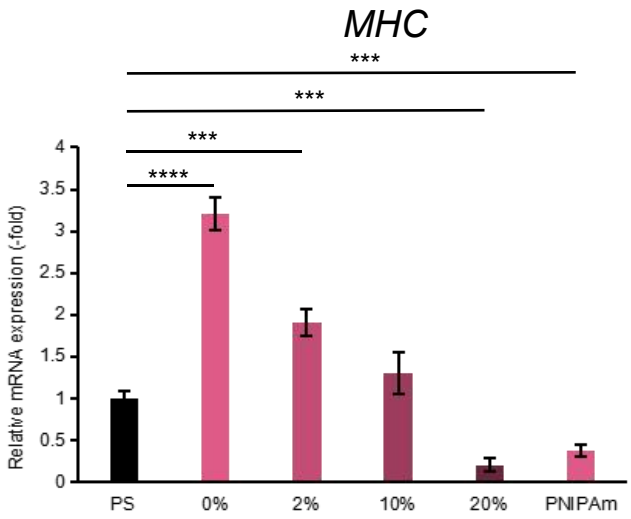

Figure 26. Expression levels of MHC were examined by qRT–PCR. A PS dish was used as the negative control. Significant differences are shown in the graph (****P < 0.001 and ***P < 0.01). Each symbol represents the mean (n = 3), and when not visible, the vertical error bar (±SD) is smaller than the symbol.

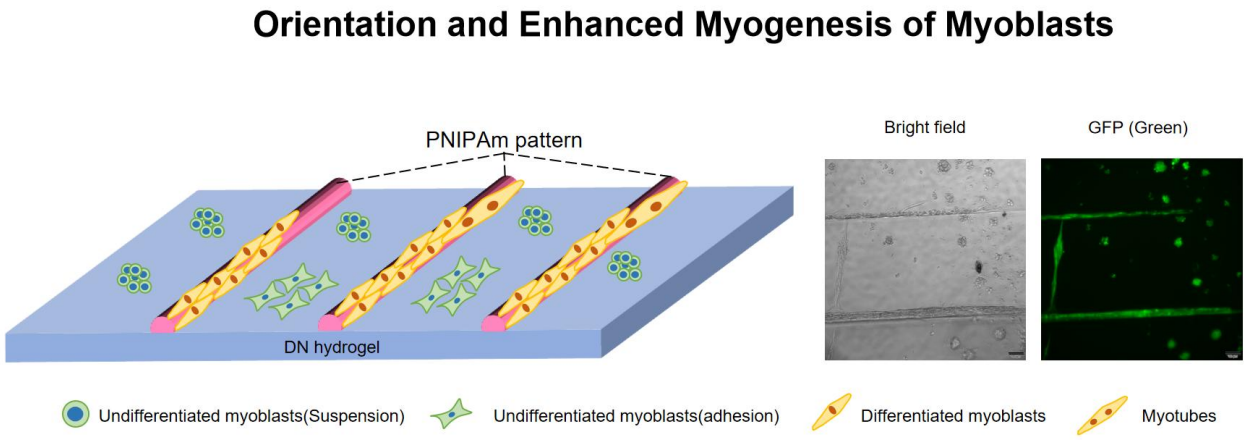

5. Discussion

The native skeletal muscle system features aligned collagen bundles in its ECM network, a structural blueprint that (1) guides anisotropic cell assembly through contact guidance effects, and (2) generates mechanical synergy for directional contraction via strain energy transfer mechanisms inherent to the fibrous architecture. Therefore, parallel alignment of muscle fibers is required for mechanically functional skeletal muscles, and transplanted muscle tissue must integrate with the orientation of the host muscle tissue. By engineering biomaterials comprising micropatterns that trigger surface alignment of rapidly growing hydrogels by force, it is possible to mimic the topographical cues of the native ECM and induce myoblasts cultured on these substrates to organize and form mature anisotropically aligned skeletal muscle tissue. To achieve this goal, tissue engineering substrates should enable individual cells to distribute, adhere, proliferate, differentiate, and mature to a functional state.

The observed tendency of cell alignment on a nanomodel substrate can be described by an engineered cytoskeleton in response to cues provided by surface features[31]. The discovery that these nanomodel substrates enhance cell elongation and anisotropy orientation suggests that long-term culture can lead to engineered skeletal muscle tissues that are morphologically similar to native skeletal muscle tissues. Interestingly, the elongation of cells cultured on patterned substrates was significantly greater than that of cells cultured on flat substrates (**Figure 22**). Since cell elongation in this case is a function of proper adhesion and myotubule formation, these results suggest that the presence of biomimetic micropatterns accelerates these events. Furthermore, the increased metabolic activity of cells cultured on the patterned substrate may be caused by an increase in cell–biomaterial interactions on the basis of penetration into the space between the nanogrooves[32].

The key factor influencing the fusion of myoblasts is the pattern width. Generally, myotubes are usually formed by the fusion of several myoblasts. When the pattern width is approximately 90 μm, it can allow 3 - 4 cells to adhere to it. This sufficient spatial condition is highly conducive to the interaction between cells, thereby promoting cell fusion and creating a favorable microenvironment for the differentiation of myoblasts into myotubes. At a proper width, the contact and signal transmission between cells are more efficient, which helps to activate key signaling pathways related to muscle differentiation, ultimately leading to the differentiation of myoblasts.

Similar to its impact on cell differentiation, a pattern width of around 90 μm also plays an important role in the directional migration of myoblasts. This width can restrict the random growth of cells, guiding them to migrate along the direction of the pattern. Compared with wider or narrower

patterns, a pattern of the appropriate width provides cells with a physical constraint and guiding cues, making cells more likely to move in a specific direction during migration, reducing their non - directional diffusion and being more beneficial for the formation of an ordered tissue morphology. In this study, we found that cell alignment was observed on the PNIPAm pattern with the width of 90 μ m (**Figure 19**), but the cells did not align on the wider PNIPAm pattern (250-300 μm) (**Figure 7**).

The roughness (height and width) of the pattern may significantly affect the selective adhesion of myoblasts. A rougher surface can provide more adhesion anchor points for cells because the surface irregularities increase the contact area and interaction sites between the cells and the material surface. Numerous studies have confirmed that cells are highly sensitive to the topological structure of the adhesion substrate. A rough surface can mimic the microscopic characteristics of the extracellular matrix, facilitating stronger binding of cells to the surface through adhesion molecules such as integrins, thus achieving selective adhesion[33]. This selective adhesion not only affects the initial attachment of cells but also further influences subsequent cell behaviors such as migration and differentiation.

An increased degree of alignment and elongation of individual myoblasts was observed in the PNIPAm micropattern culture (**Figure 19**), indicating enhanced myocyte maturation. This finding was confirmed by the increased expression of myogenic markers (**Figures 20, 21**). These results suggest that the topographical cues of micropatterns promote myogenic differentiation and maturation of myoblasts. In time-lapse photography (**Figure 24**), not all cells adjacent to the micropatterns exhibited the characteristic morphology of myotube formation. Since our primary objective was to observe the movement of cells on the PNIPAm patterns, we reduced the cell seeding density, which might affect the efficiency of cell fusion for myotube formation. Meanwhile, the degree of cell differentiation was not high enough because the observation was started on the second day after cell seeding. Furthermore, unlike most other studies, we only used regular DMEM medium in this study, instead of differentiation-inducing medium. Here, we only focus on investigating the myogenic effect of mechanical and chemical interface factors in the material microenvironment on myoblasts. Notably, we observed a diffuse cytoplasmic distribution of MyoD on the DN hydrogel and PNIPAm pattern (**Figure 19**), which has not been reported previously and may be an important feature of myogenic differentiation of cells on biomaterials.

The ECM is not only an important part of the body but also one of the main factors that constitute the cell microenvironment. Cell behavior through the surface roughness and stiffness of the matrix regulates cell growth, differentiation, migration, proliferation, and other biological

behaviors[34-37]. The mechanical properties of substrates influence the adhesion and differentiation of muscle cells. Different matrix stiffnesses have different effects on cell fate. Soft stroma (13–16 kPa) has been reported to induce cardiac differentiation of human umbilical cord mesenchymal stem cells (hUC-MSCs) compared with hard stroma (62–68 kPa)[38]. Myoblasts were inoculated on Matrigel-coated polyacrylamide gel matrices with different stiffnesses to simulate young ("soft", 0.5 kPa) and old ECMs ("stiff", 20 kPa), as well as on Matrigel-coated glass matrices with a very high stiffness (40 MPa), where, compared to cells on soft substrates, proliferation was enhanced while differentiation was reduced[39]. Consistent with this report, although the cells could attach to the PNIPAm pattern with different stiffnesses, only the soft substrate with 0 mol% crosslinking agent showed the greatest induction of myogenic differentiation in myoblasts (**Figure 24,25**). This indicates that the increase in ECM stiffness related to age and disease may lead to a reduction in the regenerative ability of myoblasts, providing a hint for subsequent muscle formation. Given the large cellular demands of muscles and taking into account both the proliferation and differentiation of myoblasts, a substrate with a stiffness of less than 5 kPa could be an optimal choice.

Transplantation of myogenic progenitor cells has emerged as a therapeutic strategy for Duchenne muscular dystrophy and related neuromuscular degeneration conditions. While current clinical protocols predominantly utilize intramuscular delivery via localized injections, significant limitations persist regarding cellular engraftment efficiency and long-term viability. Crucially, the structural mismatch between transplanted cell clusters and native muscle architecture often impedes functional integration, leading to compromised graft sustainability and diminished therapeutic outcomes in functional restoration.[40-43]. These shortcomings suggest that while myotubes in the host tissue may serve as a template for the alignment of injected cells, this does not occur easily because of the transient nature of myocyte–myotube or stem cell–myotube interactions. Similarly, polymer scaffolds have been used for the reconstruction of several tissues, but the inflammatory response that occurs during implantation and biodegradation is a significant issue[44].

In this research endeavor, using mechanical force as an alternative trigger, to grow and chemically remodel the surface of hydrogels could be a biomimetic approach. Potentially, employing the novel mechanochemical method could be simple, clean, and energy-saving in comparison to those using heat or light. The surface of DN hydrogel lacks the functional sites necessary for chemical grafting, making surface modification a formidable challenge. Here, we introduced a mechanochemical strategy that induces free radicals on the DN hydrogel surface, thereby enabling remodeling and modification by radical polymerization. This approach boasts broad applicability and can be widely used for polymeric materials possessing DN topological structures. in contrast to the

traditional synthetic substrate-guided differentiation techniques and conventional photo-triggered growth that is restricted to photo-active substrates, the force-triggered growth is not limited in principle to DN hydrogels, rather can be extended to various multi-network polymer materials. As a result, it presents a promising avenue for exploring force-triggered microstructures within degradable multi-network polymers in the realm of bioengineering. Moreover, we used a temperature-responsive polymer (poly(*N*-isopropylacrylamide) (PNIPAm)) (**Figure 11**), which experienced a significant transition from hydrophobic to hydrophilic at an LCST of 32°C[27]. Therefore, the NIPAm pattern on the surface of DN hydrogels can control cell adhesion and detachment by simple temperature changes[45]. On these surfaces, various cell types adhere, spread, and proliferate similarly to normal PS dishes at 37°C. When the incubation temperature was decreased to 20°C, the grafted PNIPAm changed from hydrophobic to hydrophilic. All cells will detach in the short-bundled cell groups, (**Figure 12**), while only some cells appear to detach spontaneously in the long-bundled cell groups (**Figure 11**). This phenomenon can be ascribed to the fact that PNIPAm becomes hydrophilic at 20°C. The hydrophilic property of PNIPAm impedes the interaction between proteins and the surface, thereby reducing protein adsorption and influencing cell attachment. Nevertheless, the topological structure on the PNIPAm surface plays a vital role. It enlarges the contact area of cells, which is favorable for the formation of integrin clusters, which stimulate the formation of adhesion foci, resulting in incomplete cell detachment. Using these temperature-responsive surfaces, cultured cells can be harvested as intact plates along with their deposited ECMs for tissue engineering applications. Unlike previous approaches, temperature-responsive surfaces allow cultured cells to be harvested without using proteases, such as trypsin or lysozyme, which may lead to cell damage and loss of differentiation phenotypes[46,47]. In addition, because the ECM still exists on the basal surface of the cell sheets[48], it can be grafted directly onto the tissue beds or layered to create three-dimensional (3D) tissue-like structures.

6. References

1. Bach, A. D.; Beier, J. P.; Stern-Staeter, J.; Horch, R. E. Skeletal muscle tissue engineering. *J Cell Mol Med* **2004**, 8, 413-422.

2. Ma, Z.; Kotaki, M.; Inai, R.; Ramakrishna, S. Potential of nanofiber matrix as tissue-engineering scaffolds. *Tissue Eng* **2005**, 11, 101-109.

3. Nisbet, D. R.; Forsythe, J. S.; Shen, W.; Finkelstein, D. I.; Horne, M. K. Review paper: a review of the cellular response on electrospun nanofibers for tissue engineering. *J Biomater Appl* **2009**, 24, 7-29.

4. Choi, J. S.; Lee, S. J.; Christ, G. J.; Atala, A.; Yoo, J. J. The influence of electrospun aligned poly(epsilon-caprolactone)/collagen nanofiber meshes on the formation of self-aligned skeletal muscle myotubes. *Biomaterials* **2008**, 29, 2899-2906.

5. Pan, S.; Zhu, C.; Wu, Y.; Tao, L. Chitosan-Based Self-Healing Hydrogel: From Fabrication to Biomedical Application. *Polymers (Basel)* **2023**, 15, 3768.

6. Liu, Y.; He, W.; Zhang, Z.; Lee, B. P. Recent Developments in Tough Hydrogels for Biomedical Applications. *Gels* **2018**, 4, 46.

7. Kong, X.; Guo, G.; Yiming, B.; Hu, J.; Zheng, Q.; Li, T.; Wu, Z.; Qian, J. Tissue-Compatible and Lubricated Hydrogel Catheter with Promising Activity Against Polymicrobial Infections for Ventilator-Associated Pneumonia Prevention. *Adv Healthc Mater* **2024**, 13, e2401750.

8. Gao, F.; Xu, Z.; Liang, Q.; Li, H.; Peng, L.; Wu, M.; Zhao, X.; Cui, X.; Ruan, C.; Liu, W. Osteochondral Regeneration with 3D-Printed Biodegradable High-Strength Supramolecular Polymer Reinforced-Gelatin Hydrogel Scaffolds. *Adv Sci (Weinh)* **2019**, 6, 1900867.

9. Gong, J. P.; Katsuyama, Y.; Kurokawa, T.; and Osada,Y. Double-Network Hydrogels with Extremely High Mechanical Strength. *Advanced Materials* **2003**, 15, 1155–1158.

10. Gong, J. P. Why are double network hydrogels so tough? *Soft Matter* **2010**, 6, 2583–2590.

11. Mu, Q.; Cui, K.; Wang, ZJ.; Matsuda, T.; Cui, W.; Kato, H.; Namiki, S.; Yamazaki, T.; Frauenlob, M.; Nonoyama, T.; Tsuda, M.; Tanaka, S.; Nakajima, T.; Gong, J. P. Force-triggered rapid microstructure growth on hydrogel surface for on-demand functions. *Nat Commun* **2022**, 13, 6213.

12. Matsuda, T.; Kawakami, R.; Namba, R.; Nakajima, T.; Gong, J. P. Mechanoresponsive self-growing hydrogels inspired by muscle training. *Science* **2019**, 363, 504-508.

13. Verstraeten, F.; Göstl, R.; Sijbesma, R. P. Stress-induced colouration and crosslinking of polymeric materials by mechanochemical formation of triphenylimidazolyl radicals. *Chem. Commun* **2016***,* 52, 8608–8611.

14. Matsuda, T.; Kawakami, R.; Namba, R.; Nakajima, T.; Gong, J. P. Mechanoresponsive self-growing hydrogels inspired by muscle training. *Science* **2019**, 363, 504-508.

15. Zhang, Q.; Dong, P.; Chen, L.; Wang, X.; Lu, S. Genipin-cross-linked thermosensitive silk sericin/poly(N-isopropylacrylamide) hydrogels for cell proliferation and rapid detachment. *J Biomed Mater Res A* **2014**, 102, 76-83.

16. Frauenlob, M.; King, D. R.; Guo, H.; Ishihara, S.; Tsuda, M.; Kurokawa, T.; Haga, H.; Tanaka, S.; Gong, J. P. Modulation and characterization of the double network hydrogel surface-bulk transition. *Macromolecules* **2019**, 52, 6704-6713.

17. Imaoka, C.; Nakajima, T.; Indei, T.; Iwata, M.; Hong, W.; Marcellan, A.; Gong, J. P. Inverse mechanical-swelling coupling of a highly deformed double-network gel. *Sci. Adv* **2023**, 9, eabp8351.

18. Nakajima, T.; Sato, H.; Zhao, Y.; Kawahara, S.; Kurokawa, T.; Sugahara, K.; Gong, J. P. A universal molecular stent method to toughen any hydrogels based on double network concept. *Adv. Funct. Mater* **2012***,* 22, 4426-4432.

19. Nakajima, T.; Ozaki, Y.; Namba, R.; Ota, K.; Maida, Y.; Matsuda, T.; Kurokawa, T.; Gong, J. P. Tough double-network gels and elastomers from the nonprestretched first network. *ACS Macro Lett* **2019**, 8, 1407-1412.

20. Matsuda, T.; Nakajima, T.; Fukuda, Y.; Hong, W.; Sakai, T.; Kurokawa, T.; Chung, U.; Gong, J. P. Yielding criteria of double network hydrogels. *Macromolecules* **2016**, 49, 1865-1872.

21. Matsuda, T.; Kawakami, R.; Nakajima, T.; Gong, J. P. Crack tip field of a double-network gel: visualization of covalent bond scission through mechanoradical polymerization. *Macromolecules* **2020**, 53, 8787-8795.

22. Mu, Q.; Zhang, Q.; Yu, W.; Su, M.; Cai, Z.; Cui, K.; Ye, Y.; Liu, X.; Deng, L.; Chen, B.; Yang, N.; Chen, L.; Tao, L.; Wei, Y. Robust multiscale-oriented thermoresponsive fibrous hydrogels

with rapid self-recovery and ultrafast response underwater. *ACS Appl. Mater. Interfaces* **2020**, 12, 33152-33162.

23. Sanz, B.; Bilderling, C.; Tuninetti, J. S.; Pietrasanta, L.; Mijangos, C.; Longo, G. S.; Azzaroni, O.; Giussi, J. M. Thermally-induced softening of PNIPAm-based nanopillar arrays. *Soft Matter* **2017**, 13, 2453-2464.

24. Wang, T.; Chen, H.; Liu, K.; Wang, S.; Xue, P.; Yu, Y.; Ge, P.; Zhang, J.; Yang, B. Janus Si micropillar arrays with thermal-responsive anisotropic wettability for manipulation of microfluid motions. *ACS Appl Mater Interfaces* **2015**, 7, 376-382.

25. Yamauchi, H.; Maeda, Y. LCST and UCST behavior of poly(N-isopropylacrylamide) in DMSO/water mixed solvents studied by IR and micro-Raman spectroscopy. *J Phys Chem B* **2007**, 111, 2964-2968.

26. Cai, K.; Lin, S.; Yao, K. Advances in Research on Surface Engineering of Biomaterials for Tissue Engineering. *Progress in Chemistry* **2001**, 13, 56-64.

27. Stetsyshyn, Y.; Raczkowska, J.; Harhay, K. et al. Temperature-responsive and multi-responsive grafted polymer brushes with transitions based on critical solution temperature: synthesis, properties, and applications. *Colloid Polym Sci* **2021**, 299, 363 – 383.

28. Ferri, P.; Barbieri, E.; Burattini, S.; Guescini, M.; D'Emilio, A.; Biagiotti, L.; Del Grande, P.; De Luca, A.; Stocchi, V, Falcieri, E. Expression and subcellular localization of myogenic regulatory factors during the differentiation of skeletal muscle C2C12 myoblasts. *J Cell Biochem* **2009**, 108, 1302-1317.

29. Chen, W.; Simmons, C. A. Lessons from (patho)physiological tissue stiffness and their implications for drug screening, drug delivery and regenerative medicine. *Adv Drug Deliv Rev* **2001**, 30, 269-276.

30. Discher, D. E.; Janmey, P.; Wang, Y. Tissue cells feel and respond to the stiffness of their substrate. *Science* **2005**, 310, 1139-1143.

31. Wang, P.; Yu, H.; Tsai, W. B. Modulation of alignment and differentiation of skeletal myoblasts by submicron ridges/grooves surface structure. *Biotechnol Bioeng* **2010**, 106, 285-294.

32. Kim, D. H.; Lipke, E. A.; Kim, P.; Cheong, R.; Thompson, S.; Delannoy, M.; Suh, K. Y.; Tung, L.; Levchenko, A. Nanoscale cues regulate the structure and function of macroscopic cardiac tissue constructs. *Proc Natl Acad Sci U S A* **2010**, 107, 565-570.

33. Anselme, K.; Bigerelle, M. Role of materials surface topography on mammalian cell response. *International Materials Reviews* **2011**, 56, 243-266.

34. McKee, C. T.; Last, J. A.; Russell, P.; Murphy, C. J. Indentation versus tensile measurements of Young's modulus for soft biological tissues. *Tissue Eng Part B Rev* **2011**, 17,155-164.

35. Keung, A. J.; de Juan-Pardo, E. M.; Schaffer, D. V.; Kumar, S. Rho GTPases mediate the mechanosensitive lineage commitment of neural stem cells. *Stem Cells* **2011**, 29, 1886-1897.

36. Ribeiro, A.; Balasubramanian, S.; Hughes, D.; Vargo, S.; Powell, E. M.; Leach, J. B. β1-Integrin cytoskeletal signaling regulates sensory neuron response to matrix dimensionality. *Neuroscience* **2013**, 248, 67-78.

37. Sun, Y.; Chen, C.; Fu, J. Forcing stem cells to behave: a biophysical perspective of the cellular microenvironment. *Annu Rev Biophys* **2012**, 41, 519-542.

38. Sun, Y.; Liu, J.; Xu, Z.; Lin, X.; Zhang, X.; Li, L.; Li, Y. Matrix stiffness regulates myocardial differentiation of human umbilical cord mesenchymal stem cells. *Aging (Albany NY)* **2020**, 13, 2231-2250.

39. Gribova, V.; Gauthier-Rouvière, C.; Albigès-Rizo, C.; Auzely-Velty, R.; Picart, C. Effect of RGD functionalization and stiffness modulation of polyelectrolyte multilayer films on muscle cell differentiation. *Acta Biomater* **2013**, 9, 6468-6480.

40. Koning, M.; Harmsen, M. C.; van Luyn, M. J.; Werker, P. M. Current opportunities and challenges in skeletal muscle tissue engineering. *J Tissue Eng Regen Med* **2009**, 3, 407-415.

41. Haykal, S.; Waddell, T. K.; Hofer, S. O. Moving towards in situ tracheal regeneration: the bionic tissue engineered transplantation approach. *J. Cell. Mol. Med* **2010**. 14, 1877-1889.

42. Meregalli, M.; Farini, A.; Parolini, D.; Maciotta, S.; Torrente, Y. Stem cell therapies to treat muscular dystrophy: progress to date. *BioDrugs* **2010**, 24, 237-247.

43. Scime, A.; Caron, A. Z.; Grenier, G. Advances in myogenic cell transplantation and skeletal muscle tissue engineering. *Front Biosci (Landmark Ed)* **2009**, 4, 3012-3023.

44. Mikos, A. G.; McIntire, L. V.; Anderson, J. M.; Babensee, J. E. Host response to tissue engineered devices. *Adv Drug Deliv Rev* **1998**, 33, 111-139.

45. Okano, T.; Yamada, N.; Okuhara, M.; Sakai, H.; Sakurai, Y. Mechanism of cell detachment from temperature-modulated, hydrophilic-hydrophobic polymer surfaces. *Biomaterials* **1995**, 16, 297-303.

46. Kushida, A.; Yamato, M.; Isoi, Y.; Kikuchi, A.; Okano, T. A noninvasive transfer system for polarized renal tubule epithelial cell sheets using temperature-responsive culture dishes. *Eur Cell Mater* **2005**, 10, 23-30.

47. Kushida, A.; Yamato, M.; Kikuchi, A.; Okano, T. Two-dimensional manipulation of differentiated Madin-Darby canine kidney (MDCK) cell sheets: the noninvasive harvest from temperature-responsive culture dishes and transfer to other surfaces. *J Biomed Mater Res* **2001**, 54, 37-46.

48. Kushida, A.; Yamato, M.; Konno, C.; Kikuchi, A.; Sakurai, Y.; Okano, T. Decrease in culture temperature releases monolayer endothelial cell sheets together with deposited fibronectin matrix from temperature-responsive culture surfaces. *J Biomed Mater Res* **1999**, 45, 355-362.

49. Fang, H.; Gao, Y.; Wang, H.; Yin, H.; Li, G.; An, T. Photo-induced oxidative damage to dissolved free amino acids by the photosensitizer polycyclic musk tonalide: Transformation kinetics and mechanisms, *Water Research* **2017**, 115, 339-346.

50. Kobayashi, J.; Okano, T. Fabrication of a thermoresponsive cell culture dish: a key technology for cell sheet tissue engineering. *Sci Technol Adv Mater* **2010**, 11, 14111.

7. Acknowledgments

We thank Y. Katsuyama for the preparation of the experimental devices and S. Kohsaka (National Cancer Center Research Institute, Tokyo, Japan) for providing the C2C12-GFP cells. Funding: This work was supported by JST SPRING, Grant Number JPMJSP2119; JSPS KAKENHI Grant Nos. 22H04968, 22K21342, 23K07825, 24K03245 and 24H00037; JST FOREST Grant No. JPMJFR221X; Japan Agency for Medical Research and Development Grant No. 24ama221532h0001.

.